C • H • A • P • T • E • R • 2

CENTRIFUGAL PUMPS

SECTION 2.1
CENTRIFUGAL PUMP THEORY

PAUL COOPER

INTRODUCTION

A centrifugal pump is a rotating machine in which flow and pressure are generated dynamically. The inlet is not walled off from the outlet as is the case with positive displacement pumps, whether they are reciprocating or rotary in configuration. Rather, a centrifugal pump delivers useful energy to the fluid or "pumpage" largely through velocity changes that occur as this fluid flows through the impeller and the associated fixed passageways of the pump; that is, it is a "rotodynamic" pump. All impeller pumps are rotodynamic, including those with radial-flow, mixed-flow, and axial-flow impellers: the term "centrifugal pump" tends to encompass all rotodynamic pumps.

Although the actual flow patterns within a centrifugal pump are three-dimensional and unsteady in varying degrees, it is fairly easy, on a one-dimensional, steady-flow basis, to make the connection between the basic energy transfer and performance relationships and the geometry or what is commonly termed the "hydraulic design" (more properly the "fluid dynamical design") of impellers and stators or stationary passageways of these machines.

In fact, disciplined one-dimensional thinking and analysis enables one to deduce pump operational characteristics (for example, power and head versus flow rate) at both the optimum or design conditions and off-design conditions. This enables the designer and the user to judge whether a pump and the fluid system in which it is installed will operate smoothly or with instabilities. The user should then be able to understand the offerings of a pump manufacturer, and the designer should be able to provide a machine that optimally fits the user's requirements.

The complexities of the flow in a centrifugal pump command attention when the energy level or power input for a given size becomes relatively large. Fluid phenomena such as recirculation, cavitation, and pressure pulsations become important; "hydraulic" and mechanical interactions—involving stress, vibration, rotor dynamics, and the associated design approaches, as well as the materials used—become critical; and operational limits must be understood and respected.

NOMENCLATURE

NOTE: The units for each quantity defined are as stated in this nomenclature, unless otherwise specifically stated in the text, equations, figures, or tables.

A = area, in^2 (mm).

a = constant of the diffuser or volute configuration in Pfleiderer's slip relation.

a = radius of impeller disk, ft (m), = $r_{t,2}$.

A_p = area of flow passage normal to the flow direction, ft^2 (m^2).

b = width of an impeller or other bladed passage in the meridional plane, ft (m).

NOTE: When dealing with radial thrust, b_2 includes also the thickness of the shrouds.

C_p = specific heat of liquid being pumped, Btu/(lbm-degF); [kcal/(kg-degC)].

c or V = absolute velocity, ft/sec (m/s).

D = diameter; unless otherwise subscripted = impeller exit diameter, ft (m).

d = diameter, ft (m).

D_h = hydraulic diameter of flow passage (= $4A_p/\wp$), ft (m).

F = thrust force, lbf (N).

g = acceleration due to gravity, = 32.174 ft/sec^2 (9.80665 m/s^2) at earth sea level.

g_o = constant in Newton's Second Law, = 32.174 (lbm-ft)/(lbf-sec^2). (There is no SI equivalent; use the dimensionless constant 1 in place of g_o in SI computations.)

$\{g_p\}$ = set of fluid properties associated with gas-handling phenomena

H = head of liquid column, ft (m) (Eq. 3); can also have the same meaning as the change in head ΔH (that is, the same meaning as "pump head").

ΔH = change in head across pump or pump stage, also called the "pump head" or "total dynamic head" ft (m).

ΔH = the small reduction in pump head (usually 3%) in testing for NPSHR, ft (m).

H_e = $H_{i,\infty}$ = the ideal head for an infinite number of blades that produce no blockage.

H_i = ideal head [= $H + \Sigma(H_L)$], ft (m) (Eq. 15b); sometimes called the "input head."

H_L = head loss, ft (m).

ΣH_L = all losses in the main flow passages from pump inlet to pump outlet, ft (m).

h = static enthalpy in Btu/lbm times $g_o J$, ft^2/sec^2; (or in kcal/kg times J, $m^2/s^2 = J$/kg).

h_{sv} or $NPSH$ = net positive suction head, ft (m).

ID = inner diameter.

J = the mechanical equivalent of heat, 778 ft-lbf/Btu (4184 N-m/kcal).

ℓ = blade, vane, or passage arc length, ft (m).

M or T = torque, lbf-ft (N-m).

m = distance in streamwise direction in meridional plane (Figure 14), in or ft (m).

$\dot{m}$ = mass flow rate, lbf-sec/ft (kg/s), = ρQ.

$MCSF$ or $Q_{\min}$ = minimum continuous stable flow, ft³/sec (m³/s).

N or n = rotative speed of the impeller, rpm.

$NPSH$ or h_{sv} = net positive suction head, ft (m).

$NPSHA$ or $NPSH_A$ = available $NPSH$.

$NPSHR$ or $NPSH_R$ = required $NPSH$ to prevent significant loss (> 3%) of pump Δp or to protect the pump against cavitation damage, whichever is greater.

$NPSH3\%$ or $NPSH_{3\%}$ = required $NPSH$ to prevent significant loss (> 3%) of pump Δp; this is the "performance $NPSH$" defined in Section 2.3.1.

n_b or Z_i = number of impeller blades.

n_q = specific speed in rpm, m³/s, m units (Eq. 38b) = N_s/51.64 (Eq. 39c).

n_v or Z_d = number of vanes in diffuser or stator.

N_s or $N_{s(\mathrm{US})}$ or n_s = specific speed in rpm, gpm, ft units (Eq. 38a).

N_{ss} or S = suction specific speed in rpm, gpm, ft units (Eq. 42).

OD = outer diameter.

P = total pressure, lbf/ft² (Pa).

p = pressure, lbf/ft² [Pa (=N/m²)] (= "static pressure").

Δp = pressure rise, lbf/ft² (Pa).

p_L = pressure loss, lbf/ft² (Pa).

$p_{L,\,i}$ = impeller pressure loss from its inlet to the point of interest, lbf/ft² (Pa).

$p_{L,\,i\,+\,\mathrm{I/L}}$ = pressure loss $p_{L,\,i}$ in impeller plus pressure loss in inlet passage, lbf/ft² (Pa).

Σp_L = all losses in the main flow passages from pump inlet to pump outlet, lbf/ft² (Pa).

p_v or p_{vp} = vapor pressure of liquid being pumped, lbf/ft² (Pa).

P_I = power delivered to all fluid flowing through the impeller, ft-lbf/sec (kW).

P_S = shaft power, ft-lbf/sec (kW).

$\wp$ = perimeter of flow passage cross section normal to the flow direction, ft (m).

Q = volume flow rate or, more conveniently, "flow rate" or "capacity," ft³/sec (m³/s).

Q_{DR} = flow rate below which discharge recirculation exists, ft³/sec (m³/s).

Q_L = leakage from impeller exit to inlet, ft³/sec (m³/s).

$Q_{\min}$ or $MCSF$ = minimum continuous stable flow rate, ft³/sec (m³/s).

Q_R = flow rate below which recirculation exists, ft³/sec (m³/s).

Q_{SR} = flow rate below which suction recirculation exists, ft³/sec (m³/s).

Q3D (quasi-3D) = quasi-three dimensional.

R = radius of curvature of meridional streamline, ft (m) (Figures 13, 14, and 25).

r = radial distance from axis of rotation, ft (m).

r_b = radial distance from axis of rotation to center of circle defining impeller passage width, ft (m) (Figures 13 and 25).

r_e = maximum value of r within the "eye plane." (Figures 13 and 25).

s = width of gap between impeller disk and adjacent casing wall, ft (m).

S = N_{ss}, suction specific speed in rpm, gpm, ft units (Eq. 42).

sp. gr. = specific gravity, namely, the ratio of liquid density to that of water at 60°F (15.6°C).

{S} = set of flow properties associated with solids in the pumpage

T = axial thrust, lbf (N).

T or **T** or M = torque, lbf-ft (N-m).

T = temperature, °F or °R (°C or °K).

ΔT_c = temperature rise due to compression, °F (°C).

t = time, sec (s).

t = blade or vane thickness, ft (m).

u = internal energy in Btu/lbm multiplied by $g_o J$, ft²/sec²; (or in kcal/kg times J, m²/s²).

U = tangential speed Ωr of the point on the impeller at radius r, ft/sec (m/s).

U_e = the value of U at the maximum radial location r_e within the "eye plane."

V = volume, ft³ (m³).

V or c = absolute velocity of fluid, ft/sec (m/s).

V_e = the average value of the meridional velocity component V_m in the eye (= Q/A_e), ft/sec (m/s).

V_s = slip velocity (Figure 15), ft/sec (m/s).

W or w = velocity of fluid relative to rotating impeller, ft/sec (m/s).

W_g = the one-dimensional value of W that would exist if there were no slip.

w_1 = throat width (Figure 21), ft (m).

y = transformed distance along blade from trailing edge (Figure 19), in or ft (m).

z = axial distance in polar coordinate system, ft (m).

Z or Z_e = elevation coordinate, ft (m).

Z_d or n_v = number of vanes in diffuser or stator.

Z_i or n_b = number of impeller blades.

α = angle of the absolute velocity vector from the circumferential direction.

β = angle of the relative velocity vector or impeller blade in the plane of the velocity diagram (as seen, for example, in Figure 3) from the circumferential (tangential) direction.

γ = fluid weight density, lbf/ft^3 (N/m^3) = ρg. (1N = 1 kg-m/s^2).

δ = clearance, ft (m)

δ^* = displacement thickness of the boundary layer, ft (m).

$\delta_0{}^*$ = displacement thickness of the zero-pressure-gradient boundary layer, ft (m), ($\approx 0.002 \times \ell$ for turbulent boundary layers at $\nu = 1$ cs in typical centrifugal pumps).

ε = absolute roughness height, ft (m)

ε_2 = fraction of impeller discharge meridional area (that is, the area normal to the velocity component $V_{m,2}$) that is *not* blocked by the thickness of the blades and the boundary layer displacement thickness on blades and on hub and shroud surfaces.

$\varepsilon_{2,b}$ = fraction of the circumference at the exit of the impeller that is *not* blocked by the thickness of the blades and boundary layer displacement thickness on blades. (See computation in Table 4.)

η = η_p = pump efficiency; or a component efficiency (different subscript, Eqs. 8–11).

θ = rotational polar coordinate or central angle about the impeller axis, radians.

NOTE: In a polar-coordinate description of impeller blades or stationary vanes, θ becomes the construction angle and is usually regarded as positive in the direction of the blade development from inlet to exit of the impeller or other blade row.

μ = slip factor = V_s/U_2 (=1 − h_0, where h_0 is the slip factor as defined by Busemann[18].)

μ = absolute viscosity, lbf-sec/ft^2 (Pa-s or N-s/m^2); often quoted in centipoises, abbreviated to "cp" (1 cp = 0.001 Pa-s). [(μ in cp) = sp. gr. × (ν in cs).]

ν = kinematic viscosity (= μ/ρ), ft^2/sec (m^2/s); often quoted in centistokes, abbreviated to "cs" (1 cs = 1 mm^2/s). [(ν in cs) = (μ in cp)/sp. gr.

ρ = fluid mass density, lbf-sec^2/ft^4 (kg/m^3),= γ/g.

σ = solidity (Eq. 53).

σ = Thoma's cavitation parameter = h_{sv}/H.

T or T or M = torque, lbf-ft (N-m).

ϕ = flow coefficient.

ϕ_e = V_e/U_e = impeller inlet or eye flow coefficient.

ϕ_i (or $\phi_{i,2}$) = impeller exit flow coefficient = $V_{m,2}/U_2$ (Figure 12).

ψ = head coefficient (Figure 12); stream function (Figure 14).

ψ_i = ideal head coefficient [= $\psi_{i,2} = V_{\theta,2}/U_2$ for zero inlet swirl ($V_{\theta,1} = 0$)].

$\psi_{i,2}$ = $V_{\theta,2}/U_2$ [= ψ_i for zero inlet swirl ($V_{\theta,1} = 0$)].

Ω = angular speed of the impeller in radians per second (1/s) = $N\pi/30$.

Ω_s = universal specific speed (unitless) (Eq. 37) = $N_s/2733$ (Eq. 38a) = $n_q/52.92$ (Eq. 38b).

Ω_{ss} = universal suction specific speed (unitless) (Eq. 41) = $N_{ss}/2733$ (Eq. 42).

{2-ph} = set of fluid properties associated with vaporization

Subscripts

b = impeller blade.

D = drag due to disk friction, bearings, and seals.

DF = disk friction.

d = discharge flange or exit (ex) of the pump.

e = at the "eye" of the impeller. The "eye" is the throat (minimum-diameter point) at the entrance into the impeller and is the area defined by the "eye plane," which is normal to the axis of rotation. "e" can refer more specifically to the shroud or maximum-diameter point within the eye, as with r_e (Figure 13) or U_e. The inlet tips of the impeller blades are generally at or near this location.

ex = exit of diffuser or the discharge flange or port of the pump (d).

f = the direction of the flow.

h = hub.

i = inner limit of region or gap (Tables 4 and 5)

i (or ideal) = ideal.

i (or imp) = impeller.

in (or s) = pump inlet flange or port.

I/L = inlet passage; that is, the passage from the pump inlet flange or port to the impeller.

I = input to fluid.

L = losses.

m = "mechanical" (pertaining to efficiency, Eq. 9).

m = component of velocity in the meridional plane (that is, the axial-radial plane containing the axis of rotation).

mean = the 50% or rms meridional streamline.

n = normal or BEP value.

o = outer limit of region or gap (Tables 4 and 5).

out = pump outlet flange or port.

p = pressure side of blade or passage.

R = value of r at the impeller ring clearance.

S = shaft.

s (or in) = suction flange or inlet of the pump.

SE = shockless entry (that is, inlet velocity vector aligned with blade camber line).

s/o = shut-off or zero flow rate Q.

r = in the radial direction.

rms = the 50% or mean meridional streamline.

s = shaft.

s = suction side of blade or passage.

s = same meaning as sh and t.

sh = shroud (also at the eye plane at inlet—and in general "t" at outlet).

stg = stage.

T = entry throat of volute or diffuser.

t = the tip or maximum radial position of the impeller blades at inlet or outlet (same meaning as s and sh).

t = tongue or cutwater.

u (see θ, below).

v = volumetric (pertaining to efficiency, Eq. 11).

v = volute.

z = in the axial direction.

θ or u = component of velocity in the circumferential direction (that is, the tangential direction in the polar view that is perpendicular to the axis of rotation).

1 = impeller inlet at the blade leading edge—at the mean unless further defined.

2 = impeller outlet at the blade trailing edge—at the mean unless further defined.

3 = volute base circle or entrance to diffuser.

∞ = for an infinite number of blades that also produce zero blockage of the flow.

Superscripts

$^-$ = average value

ENERGY TRANSFER

Hydraulics or fluid dynamics has the primary influence on the geometry of a rotodynamic pump stage—of all the engineering disciplines involved in the design of the machine. It is basic to the energy transfer or pumping process. Staging is also influenced by the other disciplines, especially in high-energy pumps. The basic energy transfer relationships need to be thoroughly understood to achieve a credible design and to understand the operation of these machines. Action of the mechanical input shaft power to effect an increase in the of energy of the pumpage is governed by the first law of thermodynamics. Realization of that energy in terms of pump pressure rise or head involves losses and the second law of thermodynamics.

The First Law of Thermodynamics Fluid flow, whether liquid or gas, through a centrifugal pump is essentially adiabatic, heat transfer being negligible in comparison to the other forms of energy involved in the energy transfer process. (Yet, even if the process were not adiabatic, the density of a liquid is only weakly dependent on temperature.) Further, while the delivery of energy to fluid by rotating blades is inherently unsteady (varying pressure from blade to blade as viewed in an absolute reference frame), the flow across the boundaries of a control volume surrounding the pump is essentially steady, and the first law of thermodynamics for the pump can be expressed in the form of the adiabatic steady-flow energy equation (Eq. 1) as follows:

$$P_S = \dot{m}\left[\left(h + \frac{V^2}{2} + gZ_e\right)_{\text{out}} - \left(h + \frac{V^2}{2} + gZ_e\right)_{\text{in}}\right]$$

where

$$h = u + \frac{p}{\rho} \tag{1}$$

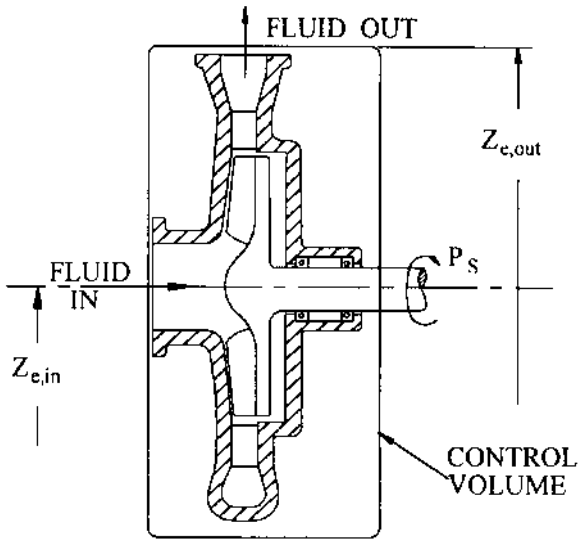

FIGURE 1 Energy transfer in a centrifugal pump

Here, shaft power P_s is transformed into fluid power, which is the mass flow rate $\dot{m}$ times the change in the total enthalpy (which includes static enthalpy, velocity energy per unit mass, and potential energy due to elevation in a gravitational field that produces acceleration at rate g) from inlet to outlet of the control volume (Figure 1).

When dealing with essentially incompressible liquids, the shaft power is commonly expressed in terms of "head" and mass flow rate, as in Eq. 2:

$$\frac{P_S}{\dot{m}} = g\Delta H + \Delta u \tag{2}$$

where

$$H = \frac{p}{\rho g} + \frac{V^2}{2g} + Z_e \tag{3}$$

The change in H is called the "head" ΔH of the pump; and, because H (Eq. 3) includes *the velocity head* $V^2/2g$ and the *elevation head* Z_e at the point of interest, ΔH is often called the "total dynamic head." ΔH is often abbreviated to simply "H" and is the increase in height of a column of liquid that the pump would create if the *static pressure head* $p/\rho g$ and the velocity head $V^2/2g$ were converted without loss into elevation head Z_e at their respective locations at the inlet to and outlet from the control volume; that is, both upstream and downstream of the pump.

The Second Law of Thermodynamics: Losses and Efficiency As can be seen from Eq. 2, not all of the mechanical input energy per unit mass (that is, the shaft power per unit of mass flow rate) ends up as useful pump output energy per unit mass $g\Delta H$. Rather, losses produce an internal energy increase Δu (accompanied by a temperature increase) in addition to that due to any heat transfer into the control volume. This fact is due to the second law of thermodynamics and is expressed for pumps in Eq 4:

$$g\Delta H < \frac{P_S}{\dot{m}} \quad \text{or} \quad \eta < 1 \tag{4}$$

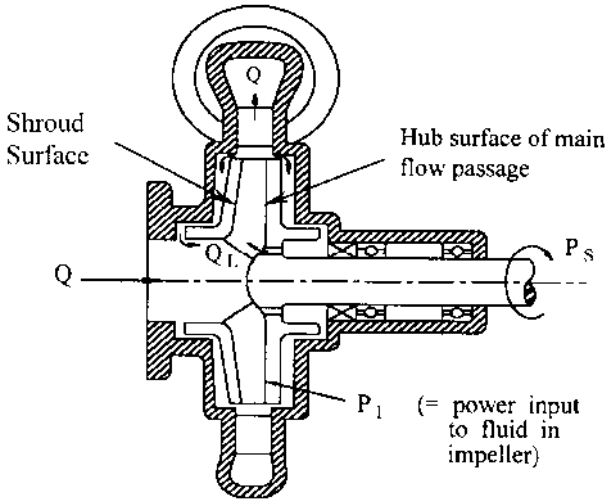

FIGURE 2 Determining component efficiencies. (This is a meridional view.)

where $\dot{m} = \rho Q$

The losses in the pump are quantified by the overall efficiency η, which must be less than unity and is expressed in Eq. 5:

$$\eta = \frac{g\Delta H\dot{m}}{P_S} = \text{Overall Pump Efficiency} \tag{5}$$

It should be pointed out here that real liquids undergo some compression—which is accompanied by a reversible increase in the temperature ΔT_c of the liquid—called the "heat of compression." This portion of the actual total temperature rise ΔT is in addition to that arising from losses and must therefore be taken into account when determining efficiency from measurements of the temperature rise of the pumpage.[1] See the discussion on this subject in Section 2.3.1.

To pinpoint the losses, it is convenient to deal with them in terms of "component efficiencies." For the typical shrouded- or closed-impeller pump shown in Figure 2, Eq. 5 can be rewritten as follows:

$$\eta = \frac{P_I}{P_S} \times \frac{g\Delta H(\dot{m} + \dot{m}_L)}{P_I} \times \frac{\dot{m}}{\dot{m} + \dot{m}_L} \tag{6}$$

Noting that

$$P_i = g\Delta H_i(\dot{m} + \dot{m}_L) \tag{7}$$

and $\dot{m} = \rho Q$

H_i = Ideal Head

one may rewrite Eq. 6 as follows:

$$\eta = \frac{P_I}{P_S} \times \frac{\Delta H}{\Delta H_i} \times \frac{Q}{Q + Q_L} = \eta_m \times \eta_{HY} \times \eta_v \tag{8}$$

where

$$\left.\begin{matrix}\text{“Mechanical”} \\ \text{Efficiency}\end{matrix}\right\} \eta_m = \frac{P_I}{P_S} = \frac{P_S - P_D}{P_S} \tag{9}$$

$$\left.\begin{matrix}\text{Hydraulic} \\ \text{Efficiency}\end{matrix}\right\} \eta_{HY} = \frac{\Delta H}{\Delta H_i} = \frac{\Delta H_i - \Sigma H_L}{\Delta H_i} \tag{10}$$

$$\left.\begin{matrix}\text{Volumetric} \\ \text{Efficiency}\end{matrix}\right\} \eta_v = \frac{Q}{Q + Q_L} \tag{11}$$

Approximate formulas for the three component efficiencies of Eq. 8 will be given further on. Their product yields the overall pump efficiency as defined in Eq. 5, and reflects the following division of the pump losses:

a. External drags on the rotating element due to i) bearings, ii) seals, and iii) fluid friction on the outside surfaces of the impeller shrouds—called “disk friction”; the total being $P_D = P_S - P_I$. Generally, the major component of P_D is the disk friction, and the “mechanical efficiency” is that portion of the shaft power that is delivered to the fluid flowing through the impeller passages.

b. Hydraulic losses in the main flow passages of the pump; namely, inlet branch, impeller, diffuser or volute, return passages in multistage pumps, and outlet branch. The energy loss per unit mass is $g\Sigma H_L = g(H_i - \Delta H)$, the ratio of output head ΔH to the input head H_i being the hydraulic efficiency. This is the major focus of the designer for typical centrifugal pump geometries (which are associated with normal “specific speeds”—to be defined later). The other two component efficiencies are then quite high and of relatively little consequence.

c. External leakages totaling Q_L leaking past the impeller and back into the inlet eye. This leakage has received its share of the full amount of power $P_I = \rho g\, \Delta H_i (Q + Q_L)$ delivered to all the fluid $(Q + Q_L)$ passing through the impeller. This leakage power is $P_L = \rho g\, \Delta H_i\, Q_L$, which is lost as this fluid leaks back to the impeller inlet. The remaining fluid input power is thus $(P_I - P_L) = \rho g\, \Delta H_i Q$, the ratio of this power to the total (P_I) being the volumetric efficiency.

There are exceptions to this convenient model for dividing up pump losses. The main exception is that if the pump has an open impeller, that is, one without either or both shrouds, that portion of the total leakage Q_L disappears. The leakage now occurs across the blade tips and affects the main flow passage hydraulic losses. The volumetric efficiency is now higher, but the hydraulic efficiency is lower. In that case disk friction is still present, as the impeller still has to drag fluid along the adjacent stationary wall(s). Another exception—for closed impellers—is that disk friction is fundamentally an inefficient pumping action, the fluid being flung radially outward[2]; and this can result in a slight increase in pump head if the fluid on the outside of an impeller shroud or disk is pumped into the main flow downstream of the impeller.

VELOCITY DIAGRAMS AND HEAD GENERATION

The mechanism of the transfer of shaft torque (or power) to the fluid flowing within the impeller is fundamentally dynamic; that is, it is connected with changes in fluid velocity. This requires the introduction of Newton’s second law, which when combined with the first

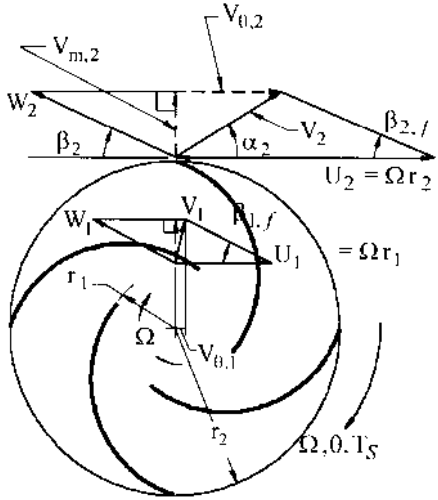

FIGURE 3 Impeller velocity diagrams (1 = inlet; 2 = outlet)

law of thermodynamics, yields Euler's Pump Equation. Fluid velocities at inlet and exit of the impeller are fundamental to this development. Fluid flowing along the blades of an impeller rotating at angular velocity Ω and viewed in the rotating reference frame of that impeller has relative velocity W. Vectorially adding W to impeller blade speed $U = \Omega r$ yields the absolute velocity V, as shown in the velocity diagrams of Figure 3.

Newton's Second Law for Moments of Forces and Euler's Pump Equation Relating impeller torque $\mathbf{T}$ to fluid angular momentum per unit mass rV_θ is the convenient way of applying Newton's second law to centrifugal pumps. This is stated as follows for the control volume $\mathbf{V}$ that contains the pump impeller (Eq. 12):

$$\Sigma\mathbf{T} = \int\int\int_{\mathbf{V}} (\partial(\rho r V_\theta)/\partial t)/d\mathbf{V} + \int\int \rho r V_\theta dQ \tag{12}$$

where $\Sigma\mathbf{T} = \mathbf{T}_S - \mathbf{T}_D$ is the summation of torques acting on the impeller; namely, the net torque $\mathbf{T}_I$ acting on the fluid flowing through it. The volume integral (first term on the right side) of Eq. 12 is the unsteady term, which is zero for steady operation. It comes into play during changing or transient conditions, such as start up and shutdown; that is, when the angular momentum per unit volume $\rho r V_\theta$ is changing with time within the impeller volume $\mathbf{V}$.

The surface integral (second term on the right hand side) of Eq. 12 is the one that pump designers and users are mainly concerned with. Its integration over the exterior surface of the control volume $\mathbf{V}$ is effectively accomplished for most impellers by combining one-dimensional results from inlet to outlet on each of several stream surfaces—imagined to be nested surfaces of revolution bounded by the hub and shroud stream surfaces (indicated in Figure 2). Insight into the power of this term can be gained by taking the mean value of the integrand in terms of the velocities on a representative stream surface; that is, essentially the surface of revolution lying at an appropriate mean location between hub and shroud. Each of the two velocity diagrams of Figure 3 lies in a plane tangent to this mean stream surface. For flow through an impeller, the torque delivered to the fluid is therefore given by the following relationship involving these average quantities:

$$\mathbf{T}_I = (\dot{m} + \dot{m}_L) \times (r_2 V_{\theta,2} - r_1 V_{\theta,1} \tag{13}$$

or $\times\ \Omega$:

$$P_I = (\dot{m} + \dot{m}_L) \times (U_2 V_{\theta,2} - U_1 V_{\theta,1}) \tag{14}$$

Eq. 13 says that the torque is equal to the mass flow rate times the change of angular momentum per unit mass $\Delta(rV_\theta)$. This becomes the "power" statement of Eq. 14 when both sides are multiplied by Ω. Following the statement of the second law of thermodynamics in Eq. 4, we now can similarly say that $g\Delta H$ must be less than the power input to the fluid per unit of mass flow rate, namely $\Delta(UV_\theta)$ from Eq. 14. So, we now arrive at Euler's Pump Equation—expressed three different ways as follows:

$$g\Delta H < \Delta(UV_\theta) \tag{15a}$$

$$g\Delta H_i = \Delta(UV_\theta) \tag{15b}$$

or

$$g\Delta H = \eta_{HY}\Delta(UV_\theta) \tag{15c}$$

The inequality (Eq. 15a) is quantified by Eq. 15b, which follows in view of Eq. 7. Eq. 15c then follows from the definition of hydraulic efficiency (Eq. 10). Euler's Pump Equation makes one of the most profound statements in the field of engineering, because it determines the major geometrical features of the design of a rotodynamic machine. By reversing the inequality in Eq. 15a, the same principle applies to turbines; hence, the more encompassing title, "Euler's Pump and Turbine Equation."

So, to design or analyze a pump, one needs to a) obtain the velocity diagrams that will produce the ideal head at the design flow rate and b) determine how the shape of these diagrams affects the hydraulic efficiency η_{HY}, so as to obtain the desired pump stage head. Step (a) for a given pump is a simple one-dimensional exercise that utilizes the principles of continuity and kinematics (Eqs. 16 and 17) to construct the velocity diagrams for a given total impeller volume flow rate Q and pump rotative speed (Ω or N):

Continuity:
$$Q = 2\pi r b V_m \tag{16}$$

where $W = V_m/\sin\beta_f$

Kinematics:
$$V_\theta = U - W\cos\beta_f \tag{17}$$

Step (b) is in essence the evaluation of the hydraulic losses ΣH_L in Eq. 10, which depend mainly on the relative and absolute velocities, the associated flow passage dimensions, and incidence angles. Eq. 15c then gives the head that the pump stage will generate. Performing steps (a) and (b) at several other flow rates at the same speed enables one to develop the pump performance characteristics.

STATIC PRESSURE GENERATION

The Extended Bernoulli Equation To estimate the losses, it is convenient first to investigate the static pressure and velocity head portions of the total head. Eq. 15c can be written in terms of the total pressure P, which equals ρgH. Similarly, we may speak of hydraulic losses as losses of static pressure Σp_L, which equals $\rho g \Sigma H_L$; so

$$P = P_{in} + \rho(UV_\theta - U_1 V_{\theta,1}) - \Sigma p_L \tag{18}$$

where, from Eq. 3, the static, dynamic and potential energy components of the total pressure are brought into evidence:

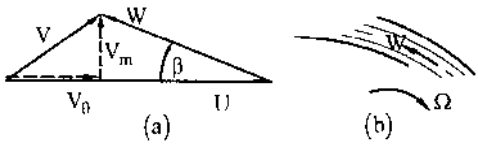

FIGURE 4 Velocity triangle and flow within impeller passageway

$$P = p + \frac{1}{2}\rho V^2 + \rho g Z_e = \rho g H \tag{19}$$

Eq. 18 is the turbomachine form of the "extended Bernoulli equation," which states that along a streamline the total pressure P—also known as the Bernoulli constant and defined in Eq. 19—is a) decreased by losses and b) increased by energy addition that occurs along the streamline.

Centrifugal and Diffusion Effects in Impellers Changes in potential energy across a pump stage are small; so the static pressure rise is found essentially from subtracting the dynamic (velocity) pressure change from the total pressure change. Within the impeller, the static pressure in turn arises from a) centrifugal and b) passage diffusion effects.

Fluid in the impeller passage of Figure 4b flows from low to high radius r or blade speed U, often also experiencing a decrease in passage relative velocity W. The geometry of the velocity diagram (Figure 4a) leads to the following combination of Eqs. 18 and 19 applied across the impeller:

$$\Delta\left(p + \frac{1}{2}\rho V_m^2 + \frac{1}{2}\rho V_\theta^2\right) = \Delta[\rho U \times (U - W\cos\beta)] - p_{L,i} - \Delta(\rho g Z_e) \tag{20}$$

and, because $V_m = W_m$, this simplifies to the following form of the extended Bernoulli equation, which applies along a streamline from the inlet of the impeller:

$$\underbrace{p - p_1}_{\text{Static Pressure Change}} = \frac{1}{2}\rho\underbrace{(U^2 - U_1^2}_{\text{Centrifugal Effect}} + \underbrace{W_1^2 - W^2)}_{\text{Passage Diffusion}} - \underbrace{p_{L,i}}_{\text{Losses: Incidence, Friction, Secondary Flow, Tip Leakage, Mixing}} - \rho g(Z_{e-Z_{e,1}}) \quad (\rho\Delta u) \tag{21}$$

Here, the U-increase corresponds to the centrifugal contribution to the static pressure rise, and the W-decrease to the diffusion contribution. There is no U-change along an axial streamline in an axial-flow impeller or propeller; so, static pressure rise is due only to diffusion. Radial-flow impellers, on the other hand, often have little or no net W-change, the centrifugal effect being paramount. [A study of the velocity diagrams of Figure 3 suggests that such impellers possess a high "degree of reaction." The degree of reaction is defined as that fraction of the total energy addition within the impeller (Eq. 15b) that does *not* include the change in absolute velocity energy, $\Delta(V^2/2)$. This fraction is, therefore, the sum

of the static pressure energy change, that due to elevation change, and the energy losses in the impeller, as can be seen from Eqs. 18 and 19.]

Collector Static Pressure Rise, Inlet Nozzle Drop A similar form of Eq. 21 applies in the stationary flow elements, where W is also the absolute velocity V and blade speed U is zero. (This would be a more recognizable form of the extended Bernoulli equation, wherein only losses modify the Bernoulli constant.[3]) A further static pressure increase occurs in the stationary collection system downstream of the impeller (with the attendant losses); namely, in the stationary volute or diffuser. This static rise is generally about a third of that in the impeller, and it is due only to diffusion, that is, the decrease in velocity in that passage. To complete the picture, there is often an increase in the comparatively small velocity in the approach passageway or nozzle or suction branch from the pump inlet port or flange to the impeller eye or blade leading edge. This is accompanied by an attendant small pressure drop.

Internal Static Pressure Distribution If the fluid enters the pump from a stagnant pool, the total pressure at the impeller eye P_1 will be very nearly the static pressure of the upstream pool (plus the pressure equivalent of the elevation of the pool above the eye). This is one reason why the local static pressure p within the pump is often referenced to P_1, as indicated in the following form of Eq. 21:

$$p - P_1 = \frac{1}{2}\rho(U^2 - W^2) - p_{L,i} - \rho g Z_e - \rho U_1 V_{\theta,1} \tag{22}$$

where

$$P_1 = p_1 + \rho\frac{V_1^2}{2} + \rho g Z_{e,1} \tag{23}$$

Figure 5 is an illustration of the internal static pressure development. The difference between P_1 and p_1 is due to the impeller inlet absolute velocity head or dynamic pressure $\rho V_1^2/2$, a much larger difference existing at the impeller exit, namely $\rho V_2^2/2$. Losses in the collector result in the pump or stage outlet total pressure P_{out} being less than P_2, the rise in total pressure ΔP_{pump} from port to port being $P_{out} - P_{in}$. In the figure, P_{in} is very nearly the same as P_1, the inlet passage loss being comparatively small for most pumps.

NET POSITIVE SUCTION HEAD

Local reduction of the static pressure p to the vapor pressure p_v of the liquid causes vaporization of the liquid and cavitation. Internal pressure drops are due to a) impeller inlet velocity head and inlet passage loss and b) blade loading and loss within the impeller. In order to prevent a substantial decrease of impeller pressure rise, the sum of these pressure drops should not exceed the difference between P_{in} and p_v, the head equivalent of which is called "net positive suction head" or *NPSH*:

$$\frac{P_{in} - p_v}{\rho g} \equiv NPSH \Rightarrow P_{in} = \rho g NPSH + p_v \tag{24}$$

Insufficient *NPSH* leads to cavitation and loss of pump pressure rise. That is because the impeller can become filled with vapor, in which case the density ρ of the fluid within the impeller is then reduced by orders of magnitude. This in turn, as can be seen in Eqs. 18–22, results in essentially zero pump pressure rise; that is, total loss of pump performance.

Eq. 24 substituted into Eq. 22 yields the local static pressure above vapor pressure in terms of the *NPSH*:

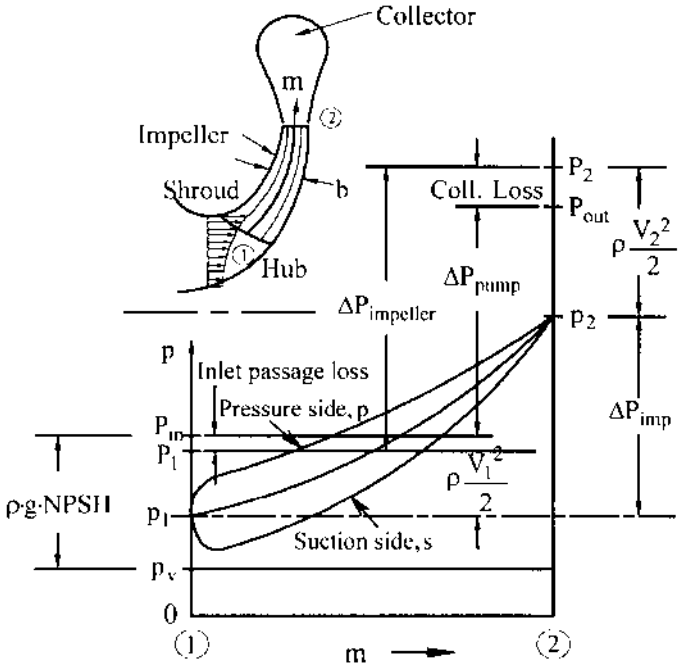

FIGURE 5 Pump stage internal pressure development. Total pressure rise $\Delta P = \rho g \Delta H$.

$$p - p_v = \rho g NPSH + \frac{1}{2}\rho(U^2 - W^2) - p_{L,\,i+I/L} - \rho g Z_e - \rho U_1 V_{\theta,\,1} \tag{25}$$

This, together with the foregoing pressure drops, which occur in the inlet region of the pump, is illustrated in Figure 5. The figure contains three plots of p along the representative streamline from 1 to 2, m being distance along this line in the meridional plane. These plots are for the suction side or trailing face of an impeller blade, the pressure side or driving face, and the average or mid-passage position. The middle or average pressure plot is readily described by Eq. 25 in terms of the local average W-distribution. The local blade-to-blade static pressure difference $p_p - p_s$ arises from the torque exerted on a strip of fluid between the blades and approximated here via blade-to-blade average velocity components in Newton's Second Law for Moments of Forces:

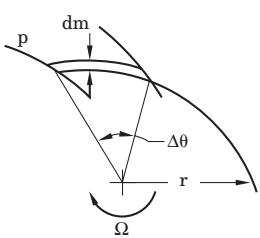

$$r(p_p - p_s)b\,dm = \rho V_m b r \cdot \Delta\theta \cdot d(rV_\theta) \tag{26}$$

$$p_p - p_s = \frac{2\pi}{n_b}\frac{\rho V_m}{\Omega}\frac{d(UV_\theta)}{dm}$$

where, for ease of illustration, the blade-to-blade polar angle difference $\Delta\theta$ is taken equal to $2\pi/n_b$, the actual value of $\Delta\theta$ being slightly less than this due to the thickness of the blades. Thus, for example, too small a number of blades n_b results in a larger value of $p_p - p_s$ and a lower minimum static pressure in the inlet region of the impeller.

The density reduction in a cavitating impeller is difficult to predict analytically; therefore, empirical relationships for acceptable levels of *NPSH* have been developed and will be presented further on, as guidelines for design and performance prediction are developed.

PERFORMANCE CHARACTERISTIC CURVES

Velocity diagrams and ideal head-rise vary with flow rate Q as illustrated in Figure 6 for the typical case of constant rotative speed N or angular speed Ω. Flow patterns in Figure 6b correspond to points on the characteristic curves of Figure 6a. The inlet velocity diagrams (just upstream of the impeller) are shown there for high and low flow rate—with zero swirl being delivered by the inlet passageway to the impeller; that is, $V_{\theta,1} = 0$. The outlet velocity diagrams on Figure 6a are found one-dimensionally, the magnitude of the exit relative velocity vector W_2 varying directly with Q and its direction being nearly tangent to the impeller blade. From these diagrams are found the absolute velocity vector V_2 and its circumferential component $V_{\theta,2}$. Because blade speed U_2 is constant, the resulting plot of the ideal head $\Delta H_i = U_2 V_{\theta,2}/g$ (from Eq. 15b) is a straight line, rising to the point U_2^2/g at zero-Q or "shut-off head." This is twice the impeller OD tip speed head $U_2^2/2g$. The right-most velocity diagram in Figure 6a has zero $V_{\theta,2}$; however, the maximum or "runout" flow rate happens at lower Q than this. That is because the actual head H is less than ΔH_i due to losses (as seen in Eq. 10), and $\Delta H = 0$ at runout—where overall pump efficiency (Eq. 8) is also zero.

This one-dimensional analysis works well in the vicinity of the best efficiency point (b.e.p. or BEP) and at higher Q because the fluid flows smoothly through the impeller pas-

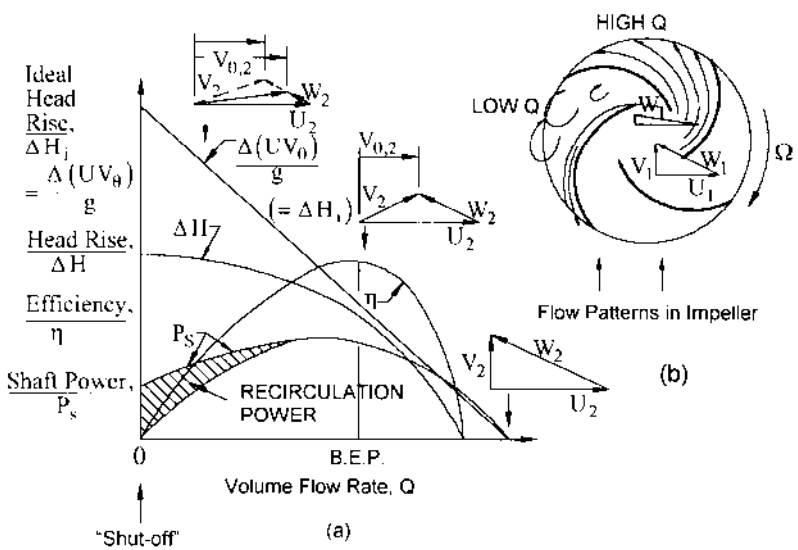

FIGURE 6A and B Characteristic performance curves of a pump stage, related to velocity diagrams

sages as illustrated in Figure 6b for "high Q." However, it fails at "low Q," where recirculating flow develops—indicated by a substantial one-dimensional deceleration or reduction in the fluid velocity relative to those passages—that is, $W_2 \ll W_1$. This is analogous to a diffuser with side walls that diverge too much: the main fluid stream separates from one or both walls and flows along in a narrow portion of the passage in a jet—the rest of the passage being occupied with eddying fluid that can recirculate out of the impeller inlet and exit. Consequently, the real outlet velocity diagram at low Q is the one with the dashed lines and the smaller value of $V_{\theta,2}$, rather than the solid-lined, one-dimensional diagram superimposed on it. This in turn reduces the ideal head at the low-Q point of the curves.

To complicate matters further at low Q, one-dimensional application of this "corrected" outlet velocity diagram via Eq. 14 would produce a pump power consumption curve that passes through the origin of Figure 6a. Such a result (assuming negligible external drag power P_D), is known not to occur in a real pump. Rather, superimposed on the jet flow pattern just described is recirculating fluid that leaves the impeller, gives up its angular momentum to its surroundings, and re-enters the impeller to be re-energized.

In other words, the one-dimensional simplifications mentioned after Eq. 12 do not hold at low Q; rather, there is an added "recirculation power," which is the UV_θ-change experienced by the recirculating fluid integrated over each element of re-entering mass flow rate[4]. The complexity of this recirculation destroys one's ability to interpret pump performance under such conditions by means of velocity diagrams. Instead, a transition is made from empirical correlations for head and power at "shutoff" or zero net flow rate to the high-Q, one-dimensional analysis, enabling one to arrive at the complete set of characteristic curves for efficiency, power, and head illustrated in Figure 6a. In fact, impeller pressure-rise at shutoff is very nearly what would be expected due to the centrifugal effect of the fluid rotating as a solid body, namely $\rho U_2^2/2$. The recirculating flow patterns seem to be merely superimposed with little effect on impeller pressure-rise. This recirculation, on the other hand, does produce some additional shutoff pressure rise in the collecting and diffusing passages downstream of the impeller.

SCALING AND SIMILITUDE

When a set of characteristic curves for a given pump stage is known, that machine can be used as a model to satisfy similar conditions of service at higher speed and a different size. Scaling a given geometry to a new size means multiplying every linear dimension of the model by the scale factor, including all clearances and surface roughness elements. The performance of the model is then scaled to correspond to the scaled-up model by requiring similar velocity diagrams (often called "velocity triangles") and assuming that the influences of fluid viscosity and vaporization are negligible. The proportions associated with Eqs. 27, 29, and 32 illustrate this. The blade velocity U (Eq. 30) varies directly with rotative speed N or angular speed Ω—and directly with size, as expressed by the radius r. For the velocity V (or W) to be in proportion to U, the flow rate Q must therefore vary as Ωr^3; hence, the "specific flow" Q_s must be constant (Eq. 28). Further, as the head is the product of two velocities, it must vary as $\Omega^2 r^2$; hence, the head coefficient ψ must be constant (Eq. 31). Finally, as power is the product of pressure-rise and flow rate, shaft power P_s must vary as $\rho\Omega^3 r^5$; hence, the power coefficient must be constant.

$$Q = AV \quad \begin{cases} A \propto r_2^2 & \propto D^2 \\ V \propto \Omega r_2 & \propto ND \end{cases}$$

$$\Rightarrow Q \propto ND^3 \quad \text{or} \quad \Omega r_2^3 \tag{27}$$

and

$$\frac{Q}{\Omega r_2^3} = \text{Constant} = Q_s \tag{28}$$

At above Q,

$$\eta = \text{Constant, and}$$

$$g\Delta H = \eta_{HY}\Delta(UV_\theta)$$

$$\Rightarrow \Delta H \propto N^2D^2 \tag{29}$$

$$U = \Omega r \tag{30}$$

and

$$\psi = \frac{g\Delta H}{U_2^2} = \text{constant} \tag{31}$$

$$P_S = \frac{\rho Q g \Delta H}{\eta}$$

$$\Rightarrow P_S \propto \rho N^3 D^5 \tag{32}$$

and

$$\hat{P}_S = \frac{P_S}{\rho\Omega^3 r_2^5} = \text{constant} \tag{33}$$

Figure 7a is the result of following these similarity rules for a given pump that undergoes a change in speed from full speed to half speed without a change in size. The similar Q at half speed for a given Q at full speed is half that at full speed. At each such half-speed Q-value, the head ΔH is accordingly one-fourth of its full-speed value and the efficiency η is unchanged. One can avoid replotting the characteristic curves in this manner for every change in speed (and size) by expressing them nondimensionally in terms of Q_s, ψ, η, and $\hat{P}_s$. They then all collapse on one another as illustrated in Figure 7b. Note that a change in pump geometry or shape of the hydraulic passageways destroys this similitude and necessarily produces a new set of curves—shaped differently but similar to each other.

Similitude enables the engineer to work from a single dimensionless set of performance curves for a given pump model. This is a practical but special case of the more general statement that pump performance as represented by efficiency, head, and power, is more generally expressed in terms of the complete physical equation as follows:

$$\eta, \Delta H, P_S = \text{fct's. } (Q, r_2, \Omega, \rho, \upsilon, NPSH, \{2\text{-}ph\}, \{g_p\}, \{S\}, \{\ell_i\}) \tag{34}$$

where $\{\ell_i\}$ is the infinite set of lengths that defines the pump stage geometry. A common group of these lengths is illustrated in Figure 8. Dimensionlessly, Eq. 34 becomes

$$\eta, \psi, \hat{P}_S = \text{fct's. } (Q_s, R_e, \tau_2, \{2\text{-}\Phi\}, \{\Gamma_p\}, \{\Sigma\}, \{G_i\}) \tag{35}$$

where the dimensionless quantities containing flow rate, viscosity and *NPSH* are respectively defined as follows:

where

$$Q_s = \frac{Q}{\Omega r_2^3} \qquad R_e = \frac{\Omega r_2^2}{\upsilon} \qquad \tau_2 = \frac{2gNPSH}{\Omega^2 r_2^2}$$

Specific Flow	Machine Reynolds Number	Cavitation Coefficient

(36)

and

- $\{G_i\} = \{\ell_i/r\}$ defines the dimensionless geometry or shape.
- $\{2\text{-}\Phi\}$ = the dimensionless quantities arising from the set of fluid, thermal, vaporization, and heat transfer properties $\{2\text{-}ph\}$ that influence the flow of two-phase vapor and liquid. These quantities come into play when the *NPSH* is low enough for such flow to be extensive enough to influence pump performance.

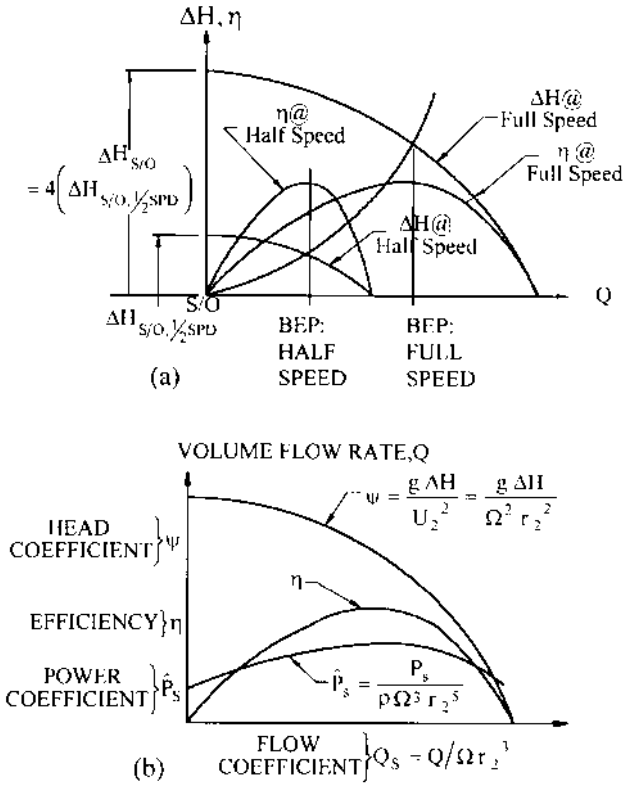

FIGURE 7 Similar performance curves: a) dimensional; b) dimensionless

- {Σ} = the dimensionless quantities arising from the set of properties associated with entrained solids and emulsifying fluids that affect the performance of slurry pumps and emulsion pumps.

SPECIFIC SPEED AND OPTIMUM GEOMETRY

The hydraulic geometry or shape of a pump stage can in principle be chosen for given values of the other independent variables in Eqs. 34 or 35 to optimize the resulting performance; for example, to maximize the best efficiency η_{BEP} under certain conditions on the head and power. Two such conditions that are common are a) no positive slope is allowed anywhere along the ΔH-vs.-Q curve of Figure 7 (called the "no drooping nor dip" condition) and b) the maximum power consumption must occur at the BEP (often called the "non-overloading" condition). A fundamental and generally typical pumping situation involves a) negligible influence of viscosity, (that is, high Reynolds number) b) the absence of two-phase fluid effects, (that is, the existence of sufficient *NPSH* or τ) and c) the absence of solid particles and emulsion-related substances in the fluid. In this situation, Eq. 35 has one remaining significant independent variable; namely, the specific flow Q_s, which in the definitions of Eq. 36 contains the volume flow rate Q, the pump speed Ω, and the characteristic radius r_2. Most users don't know the

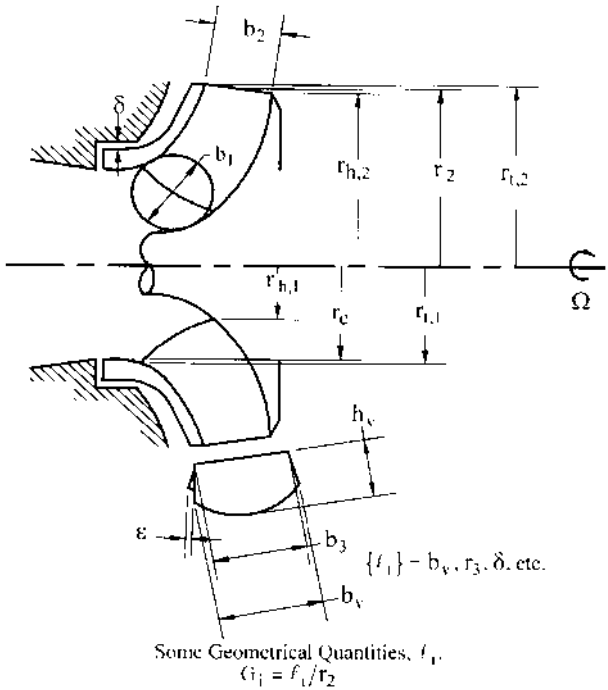

FIGURE 8 Defining the geometry of a pump stage

size of the pump stage a priori; so, r_2 is eliminated by replacing Q_s in Eq. 35 with a new quantity that is the result of dividing the square root of Q_s by the $\frac{3}{4}$-power of the head coefficient ψ. Thus, from the definitions just given of Q_s and ψ, one arrives at the *specific speed* Ω_s as the independent variable in terms of which the geometry is optimized[3]:

$$\Omega_s = \frac{\Omega\sqrt{Q}}{(g\Delta H)^{3/4}} = \frac{\sqrt{Q_s}}{\psi^{3/4}} \tag{37}$$

For convenience, specific speed is usually expressed in terms of the conventional quantities N, Q, and ΔH that correspond to the factors in Eq. 37, which quantities are expressed in the units commonly used commercially. For example, forms found in the United States and in Europe and the relationship of these to the truly unitless "universal specific speed" Ω_s defined in Eq. 37 are as follows:

$$\Omega_s = \frac{N(\text{rpm})\sqrt{Q(\text{USgpm})}/[\Delta H(\text{ft})]^{3/4}}{2733.016} = \frac{N_{s,\,(\text{U.S.})}}{2733.016} \tag{38a}$$

$$\Omega_s = \frac{N(\text{rpm})\sqrt{Q(\text{m}^3/\text{s})}/[\Delta H(\text{m})]^{3/4}}{52.919} = \frac{n_q}{52.919} \tag{38b}$$

Thus,

$$n_q(\text{m}^3/\text{s, m}) = N_s(\text{USgpm, ft})/51.64 \tag{38c}$$

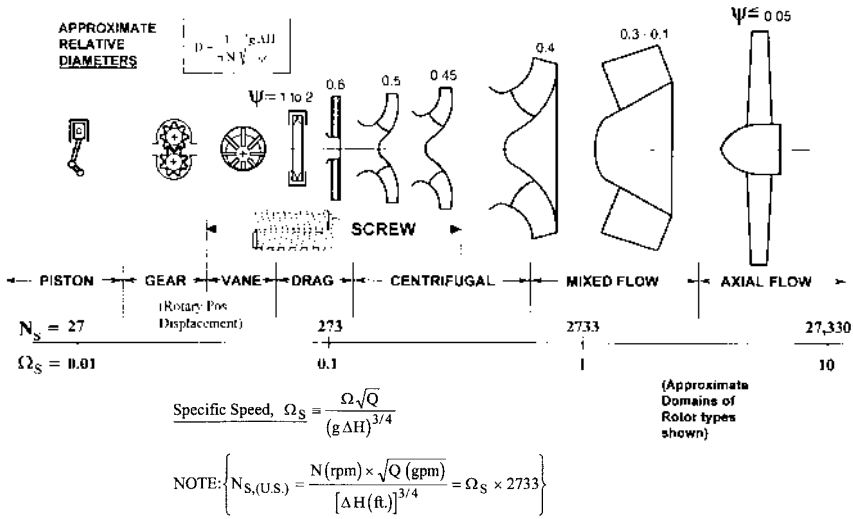

FIGURE 9 Optimum geometry as a function of BEP specific speed (for single-stage rotors)

Rotor Shape as a Function of Specific Speed Optimization of pump hydraulic geometry in terms of the BEP specific speed has taken place empirically and analytically throughout the history of pump development. An approximate illustration of the results of this process for pump rotors or impellers is shown in Figure 9. Not only does the geometry emerge from the optimization process but also the head, flow, and power coefficients for each shape as well. Approximate values for the optimum BEP head coefficient ψ are shown on the figure. The actual rotor diameter can then be deduced as noted—from the ψ-definition of Eq. 31. The relationship among the various rotors is illustrated in the figure—assuming that they all have the same speed and head; that is, as one moves along the abscissa or specific speed axis of Figure 9, only the flow rate is changing as far as the illustrations of the rotors are concerned. As would be expected, therefore, high-specific-speed impellers need to have large passages relative to their overall diameter. This is powerfully illustrated if one contrasts the propeller (high-Ω_s) with the low-Ω_s centrifugal impeller.

At the lower end of the specific speed range shown in Figure 9, rotodynamic pumps (that is, centrifugal pumps, in which category mixed- and axial-flow geometries are generally included) would be too low in efficiency to be practical. Rather, rotary positive displacement pumps take over because there is a transition through the drag pump domain. Sometimes called a regenerative or periphery pump, the drag pump is actually a rotodynamic machine, developing head peripherally around the impeller through successive passes radially through the blades on both sides until a barrier is reached at some point on the periphery, where the fluid is then discharged.[5]

The screw pump, on the other hand, is a truly positive displacement (rotary) machine. It can have two, three, or more meshing screws and can move large quantities of fluid—both single- and multiphase—against a large pressure difference Δp, giving it a specific speed range that extends well into centrifugal pump territory. Not shown is the progressive cavity pump, which has a single screw surrounded by an elastomer sealing member.

Lower flow rates are readily accommodated by the vane pump, whereas gear pumps handle a higher range of pressure differences at such flow rates. Finally, extremely high pressures are produced by reciprocating pumps, the specific speed range of which extends off the figure on the left.

Positive displacement pumps appear in Figure 9 in order to provide perspective. The concept of specific speed is not generally applied to these machines, because a given positive displacement pump can have such a wide range of pressure-rise capability at a chosen flow rate and speed as to make it difficult to associate a given rotor geometry with a particular value of specific speed. On the other hand, a unique rotodynamic pump geometry is readily associated with the specific speed of the BEP of such a machine.

Performance of Optimum Geometries Figure 9 enables one to easily identify the pump stage types associated with required pumping tasks in terms of head, flow rate, and rotative speed. Beyond this general picture is the related performance of a real pump geometry in a real fluid. Although, for centrifugal pumps, the specific speed has the major effect on performance, the available *NPSH* and the viscosity of the pumpage also have an influence. These are evident in the following formal statement of the efficiency of an optimized pump (cf Eq. 35)

$$(\eta_{\max})_{\{G_i\}_{\text{opt}}} = f\,(\Omega_s,\, \Omega_{ss},\, \{2\text{-}\Phi\},\, \{\Gamma_p\},\, \{\,\Sigma\},\, R_{e,\,H,\,Q}) \tag{39}$$

where the radius r_2, representing the size, has been eliminated from the other variables in Eq. 35 by introducing the *suction specific speed* Ω_{ss} and the *head-flow Reynolds number* $R_{e,H,Q}$, which are defined in Eqs. 40 and 41:

$$R_{e,\,H,\,Q} = \frac{\sqrt{Q}\,(g\Delta H)^{1/4}}{\nu} = R_e\sqrt{Q_s}\,\psi^{1/4} \tag{40}$$

$$\Omega_{ss} = \frac{\Omega\sqrt{Q}}{(g\,NPSH)^{3/4}} = \frac{\sqrt{Q_s}}{(\tau_2/2)^{3/4}} \tag{41}$$

where, the common form of the suction specific speed, called N_{ss}, is given in commercial U.S. units by (Eq. 42)

$$N_{ss,\,(\text{U.S.})} = \frac{N(\text{rpm})\sqrt{Q(\text{gpm})}}{[NPSH\ (\text{ft})]^{3/4}} = \Omega_{\text{ss}} \times 2733.016 \tag{42}$$

Size Effect For sufficiently high *NPSH* (or sufficiently low suction specific speed) and low viscosity (or high Reynolds number), real pumps also possess a strong size effect on efficiency. This is because, in normal manufacturing processes, the clearances δ preventing internal leakage Q_L (for example, past the impeller sealing rings in Figure 2) do not scale up as rapidly as the size (represented by r_2), nor do the surface roughness heights ε. Thus, a larger pump tends to be more efficient. Strictly speaking, however, the geometry of the larger pump is not the same as that of the smaller pump, and this forces one to modify Eq. 39 by reintroducing two of the length ratios G_i that were part of the set $\{G_i\}$ in Eq. 35 which characterize the hydraulic shape of the machine. Thus, Eq. 39, revised to reflect these realities, becomes

$$(\eta_{\max})_{\{G_i\}_{\text{opt.}}} = f_1\!\left(\Omega_s,\, \Omega_{ss},\, R_{e,\,H,\,Q},\, \{2\text{-}\Phi\},\, \{\Gamma_p\},\, \{\,\Sigma\},\, \frac{\varepsilon}{r_2},\, \frac{\delta}{r_2}\right) \tag{43}$$

A study of a large number of commercial centrifugal pumps by H. H. Anderson[6] has quantified Eq. 43 for such machines. These pumps were all operating in water and had sufficient *NPSH* for performance not to be influenced by Ω_{ss}. The results are given by Eq. 44, which is plotted in Figure 10:

$$\eta = 0.94 - 0.08955 \times \left[\frac{Q(\text{gpm})}{N(\text{rpm})} \times X\right]^{-0.21333} - 0.29 \times \left[\log_{10}\!\left(\frac{2286}{N_s}\right)\right]^2 \tag{44}$$

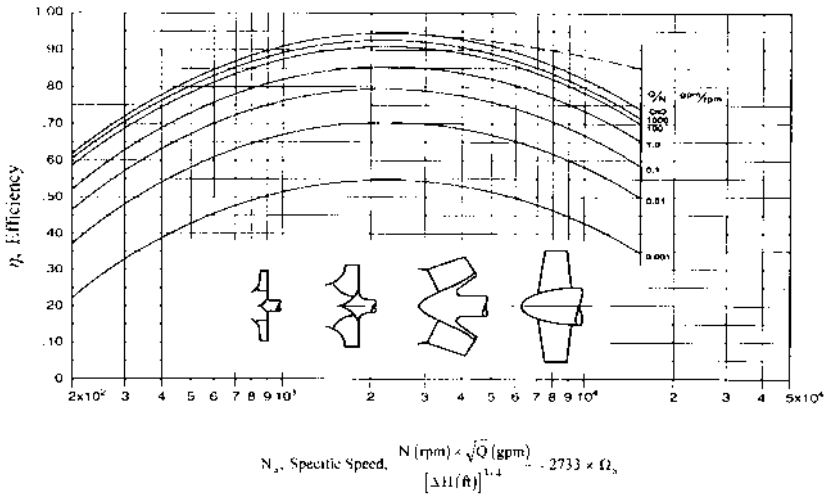

FIGURE 10 Efficiency of centrifugal pumps versus specific speed, size, and shape–adapted from Anderson[6]. Note: Actual experience for $Ns > 2286$ shows higher efficiency, as indicated by the dashed line.

where $X = \left[\dfrac{140}{\varepsilon(\mu - \text{in.})}\right]^2$

Eq. 44 is a combination of separate relationships described by Anderson for efficiency and speed as functions of flow rate[6]. Included is a correction for specific speed that is too conservative for $N_{s\,(U.S.)} > 2286$ or Ω_s greater than about unity. With this qualification, Figure 10 is a useful representation for centrifugal pumps and is often as far as many users go in determining the performance of these machines.

Viscosity Effects Centrifugal pump geometries have not generally been optimized versus Reynolds number—often because the effect on hydraulic shape is not very great except for the highest viscosities of the pumpage, and a given application can sometimes experience a substantial range of viscosity. Studies of conventional centrifugal pumps over a range of Reynolds number have been combined in nomographic charts in the Hydraulic Institute Standards, which yield correction factors to the head, efficiency, and flow rate of the BEP of a low-viscosity pump in order to obtain the BEP of that pump when operating at higher viscosity[7]. Figure 11 is a presentation of these correction factors in terms of the head-flow Reynolds number. Strictly speaking, in view of Eq. 43, each pump geometry has a unique set of such correction factors, yet the data presented in Figure 11 have been widely utilized as reasonably representative of conventional centrifugal pumps.

NPSH Effects In many cases, the available *NPSH* is low enough, or the suction-specific speed Ω_{ss} at which the pump stage must operate is high enough for significant two-phase activity to exist within the impeller. This is to be expected in centrifugal impellers of water pumps if the available Ω_{ss} is greater than about 3 to 4 (or $N_{ss,(U.S.)} = 8{,}000$ to $11{,}000$). In such a case, Ω_{ss} and the vaporization quantities {2-Φ} in Eq. 35 dictate a profound change in the impeller geometry into that of an inducer. The inducer has an entering or "eye" diameter that is significantly enlarged—together with tightly wrapped helical blading. Often the inducer is a separate stage that pressurizes the two-phase fluid as needed to provide a sufficiently low value of Ω_{ss} at the entrance of the more typical impeller blading that is immediately downstream of the inducer. If the two-phase fluid is near its thermodynamic critical point, the {2-Φ} operate to greatly reduce the amount of two-phase

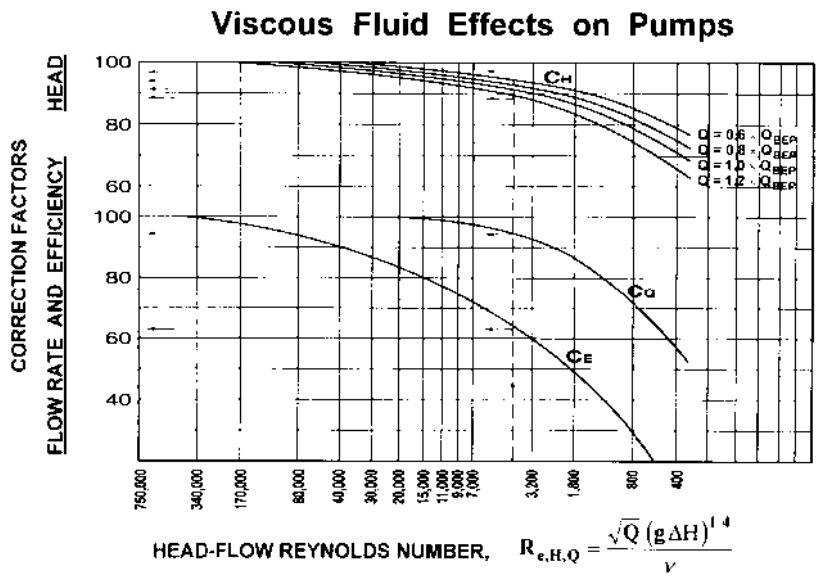

FIGURE 11 Viscous fluid effects on centrifugal pumps—adapted from Hydraulic Institute ANSI/HI 2000 Edition Pump Standards, Reference 7.

activity within the pump. (At the critical point, the liquid and gas phases are identical, and therefore both have the same specific volume.) An example is the pumping of liquid hydrogen, for which an inducer is unnecessary until much higher values of Ω_{ss} are reached. Moreover, inducers—typically limited to Ω_{ss}-values of about 10 ($N_{ss,(U.S.)} = 27{,}000$) in water—can, at sufficiently low tip speed, operate at zero *NPSH*, which corresponds to an infinite value of Ω_{ss}[8].

Pumping Entrained Gas In addition to the liquid's own vapor (which is the gas involved in the *NPSH*-effects discussion), many pumping applications deal with a different gas; that is, a different substance from the liquid being pumped. The effects of this gas on performance arise from a) the volume flow rate of the gas at the inlet, b) the pressure ratio of the pump, which determines how far into the impeller this gas volume persists; that is, how much it gets compressed, and c) how much of the gas dissolves in the liquid as the pressure increases within the pump, which depends on both the solubility and the degree of agitation of the fluid produced by the pump. The set of fluid properties associated with these gas-handling phenomena are represented by $\{g_p\}$ in Eq. 34, the dimensionless form (Eqs. 35 and 43) of this set being $\{\Gamma_p\}$. Generally, for typical commercial centrifugal pumps, the performance under such conditions usually manifests itself as a loss of pressure rise, which is reasonably stable up to an inlet volume flow rate fraction of gas to liquid of 0.04 to 0.07[9]. Inducers can handle larger inlet volume fractions of gas, and, under Dalton's law for partial pressures, the liquid's own vapor also occupies the volume of the gas bubbles. Single and multistage centrifugal pumps have been built that handle far greater gas volume than these single-stage values[10,11]; moreover, multiphase rotary positive displacement screw pumps can handle gas volume fractions up to 1 (100 percent gas)[11].

Effects of Slurries and Emulsions Finally there is the influence of the dimensionless quantities $\{\Sigma\}$ in Eq. 43. Impeller and casing design are altered so as to reduce wear-producing velocities if the pumpage is a slurry of solids contained in a carrier liquid. (Slurry pumps are usually single-stage machines with a collector or volute casing sur-

rounding the impeller.) This usually means a smaller impeller eye diameter (which, as can be seen in Figure 6, reduces the inlet relative velocity W_1,) and a larger radial distance from the impeller to the surrounding volute because the circumferential velocity component V_θ of the fluid emerging from the impeller (also seen in Figure 6) slows down with increasing radial position and is then lower in the volute passageway[12]. Performance also is altered, depending on the composition and concentration of the slurry. These are complicated non-Newtonian flows and are covered in detail elsewhere in this book in conjunction with a thorough treatment on solids-handling pumps. Emulsions are another example of such flows, many of which are destroyed by excessive local shear in the fluid. For this reason, screw pumps are sometimes utilized for emulsions rather than oversized, slow-running centrifugal pumps. Except for thin layers of the fluid at the clearances, most of the flow in a screw pump experiences very little shear in comparison to the flow through a centrifugal pump.

Electromagnetic Effects Not appearing in Eq. 43 are quantities associated with electromagnetic phenomena. For example, electric current flowing radially outward through fluid contained in an axially directed magnetic field is capable of producing a rotating flow. Called a hydromagnetic pump, this device is therefore "centrifugal," yet it has no moving parts. Such pumps have been used for liquid metals and could be made reasonably efficient for any pumpage with high conductivity.

DESIGN PROCEDURES

Establishing the Pump Configuration The first step in designing a pump is to determine the type and number of stages that are needed to meet the given set of operating conditions, usually Q, p_1, p_2, available $NPSH$ (= $NPSHA$) and specific gravity of the fluid. If the pump must meet several such sets of operating conditions, one set has to be chosen for the BEP or design point so all the others are satisfied, if possible. Making the proper choice of this BEP may require some iteration: first making a trial choice, doing a preliminary design, and determining the corresponding pump performance characteristic curves, and then repeating these steps if necessary.

Pump rotative speed N (rpm) must be chosen in order to proceed. Selection of the highest practical rpm is desirable because it yields the smallest size and therefore usually the lowest cost and easiest containment of system pressure. If, for the chosen number of stages, the stage specific speed is too low, Figure 10 indicates that efficiency is generally improved with greater speed. The maximum possible rpm is that which yields a value for the suction specific speed Ω_{ss} (Eq. 41) or N_{ss} (Eq. 42) that the first stage of the pump can accommodate, where $NPSH$ is found from Eq. 41 as follows:

$$NPSH = \frac{1}{g}\left(\frac{\Omega}{\Omega_{ss}}\right)^{4/3} Q^{2/3} \tag{45}$$

Typically, the Ω_{ss}-capability of an impeller does not exceed a value that is somewhere in the range 3 to 4.5 (N_{ss} = 8,200 to 12,300), depending on minimum (off-design) flow rate requirements, and it is typically 10 (27,000) or less for inducers. Generally, the supplier furnishes a pump that has a value of $NPSH$-capability (or "$NPSHR$") smaller than the stated $NPSHA$. This difference or "$NPSH$-margin" is desirable if there is any uncertainty as to the true value of $NPSHA$. It is essential for high values of Δp_{stg}; (see discussion of "high-energy pumps" further on in this section.) Often a higher speed can be employed if a double-suction impeller (entry of fluid from both sides) can be used, as then only half of the given Q enters each side of this impeller, and only that half can be used in the Ω_{ss}-equation applying to that fluid and impeller type.

The double-suction configuration is popular for large, single-stage pumps because the axial thrust is nominally zero. It is also found as the first stage in some multistage pumps, in which case the arrangement of the remaining impellers can be "back-to-back" (half of them facing in one direction and half opposite) to achieve axial thrust balance. On the

other hand, the interstage flow passages are simpler if these impellers are all facing in the same direction—in which case the thrust is opposed by a balancing drum or disk as described in Section 2.2.1. Forming the specific speed from N, Q, and ΔH (from Eq. 3) and referring to Figure 9 for the kind of impeller (which then gives one an idea of the other hydraulic components (inlet passage, diffuser and collector, and so on) and Figure 10 for the expected efficiency, one can decide whether the pump would perform better and still meet any installation and size restrictions with more than the one stage implied by this first N_s-calculation.

If the user requires the performance characteristics of a positive displacement pump—such as a wide range of pressure-rise at a nearly constant flow rate Q—selecting such a pump may be possible if the specific speed is not too high. (See Figure 9.) The choice of speed for positive displacement pumps is sometimes determined by mechanical considerations rather than suction capability.

Sizing the Pump The next step is to determine the approximate size of a pump or pump installation. Beginning with the impeller, the agent of the energy transfer to the fluid in a pump, one utilizes the results of the pump hydraulic geometry optimization process. This also yields the proportions of the velocity diagrams that correspond to the geometry associated with the desired value of specific speed. These in turn lead to two major sizing factors for an impeller, which are plotted for typical commercial pumps in Figure 12; namely the head coefficient ψ (originally defined in Eq. 31) and the outlet flow coefficient ϕ_i defined on this figure[4]. Equations in the figure show how these factors are used to determine the exit radius r_2 (or diameter D_2) and the width b_2 (Figure 8) respectively. The flow coefficient ϕ_i is obviously a velocity component ratio. For the head coefficient of a pump with zero inlet prewhirl to the impeller (that is, $V_{\theta,1} = 0$), the relevant

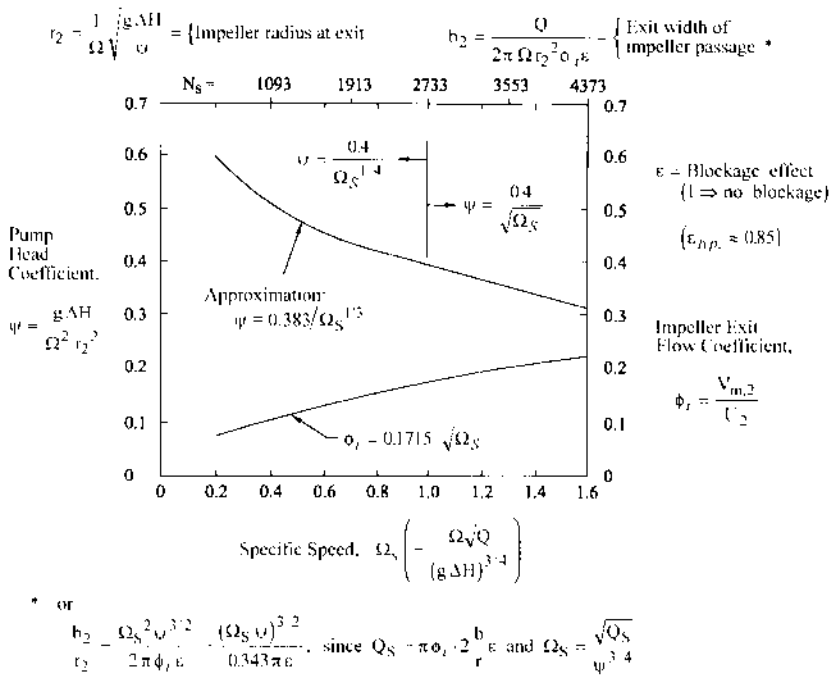

FIGURE 12 Sizing factors for the diameter and width of typical impellers—adapted from Stepanoff [4].

velocity ratio (see Figure 3) is $V_{\theta,2}/U_2$, which in view of Eqs. 15b and 31 is equal to the ideal head coefficient ψ_i, as this corresponds to the ideal head H_i. Referring to Eq. 15c, it is obvious that the actual head coefficient $\psi = \eta_{HY} \times \psi_i$, or, in the (common) case of zero prewhirl, $\psi_i = V_{\theta,2}/U_2$.

Overall pump dimensions are conveniently viewed in terms of factors times the impeller diameter. The overall diameter exceeds that of the impeller due to the surrounding casing. For single stage pumps, this casing will include a volute and perhaps a set of diffuser vanes immediately surrounding the impeller; so, the casing diameter can be 50% greater than D_2 or more. On multistage pumps (many with radial-outflow diffusers and return vanes), this excess is often less than 50%.

Single-stage pump axial length includes provision for inlet passageways and bearing housings and is therefore approximately the same as the overall pump diameter. On the other hand, the axial length of a stage in a multistage pump is often less than half of the impeller diameter. Minimizing this "stage length" (and diameter) is a goal of competitive pump designers in the quest to create a machine of light weight and low cost. But too small a stage length is accompanied by inferior hydraulic performance because not enough room is provided for the passages around and within the impeller to turn the fluid with minimum loss. Further, the bearing housings and the suction and discharge "heads" or end pieces must be considered in arriving at the overall length of a multistage pump.

This sizing discussion so far has focused on pumps with a radial-outflow geometry. For the axial-flow geometries of higher specific speeds, the situation is simpler. The diameters of the propeller (Figure 9) and any stationary vanes downstream (or upstream) are essentially the same. The approach and discharge piping is of about the same size. A simple guideline for the maximum radius of the propeller is found from the following approximate extrapolation of the ψ-curve of Figure 12:

$$\psi_t = \frac{0.53}{\Omega_s} \tag{46}$$

where the outer radius of the propeller $r_{t,2}$ should be substituted for the mean exit radius r_2 in the ψ-definition. Thus the ψ-curve is in reality a ψ_t-curve for non-radial-flow pumps. For small departures from radial flow, as illustrated in Figure 8, the ψ-curve of Figure 12 can be used either way.

These guidelines are often all that pump users or fluid system designers need to plan their installations. To get beyond this overview, one must pursue the hydraulic design in detail—as afforded by the following development and examples.

Designing the Impeller Determination of the geometrical features of the impeller is generally accomplished in the following order: a) the "eye" radius r_e, b) the exit radius r_2 or $r_{t,2}$, and c) the exit width b_2 or, in the case of mixed- and axial-flow impellers, the hub exit radius $r_{h,2}$—all of which form the starting point for d) shaping the hub and shroud profiles (Figure 13); and, finally, e) construction of the blades.

a) The eye. The inlet radius of the impeller eye r_e (Figure 13) is nearly the same as $r_{t,1}$, which is the diameter of the tips of the impeller blades at the inlet. This emerges after the eye flow coefficient $\phi_e = V_e/U_e$ [the ratio of the one-dimensional axial velocity entering the eye (Figure 8) to the tangential speed of the impeller eye $U_e = \Omega r_e$] is known:

$$\phi_e = \frac{Q/A_e}{\Omega r_e} = \frac{\overline{V_e}}{U_e} \tag{47}$$

$$A_e = \pi(r_e^{\,2} - r_s^{\,2}) \tag{48}$$

Thus, r_e can be found from the following combination of Eqs. 47 and 48:

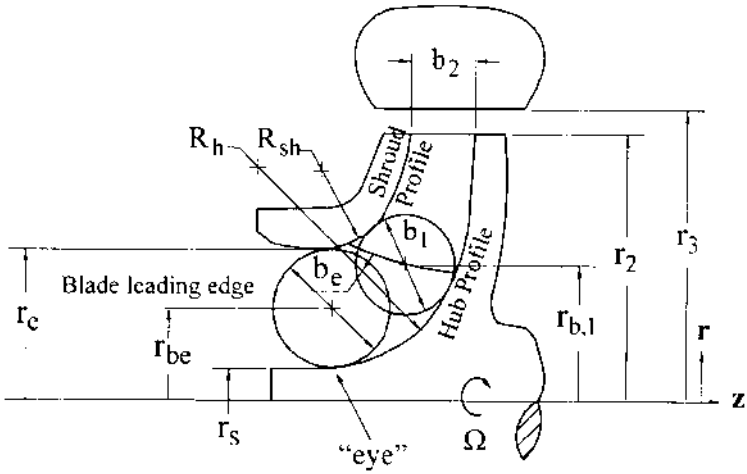

FIGURE 13 Hub and shroud profiles of centrifugal pump impeller

$$r_e = \left[\frac{Q}{\pi \Omega \phi_e \left(1 - \dfrac{r_s^2}{r_e^2} \right)} \right]^{1/3} \tag{49}$$

where the shaft-to-eye ratio r_s/r_e can be estimated at first. Typical values for ϕ_e vary from 0.2 to 0.3 for impellers and down to 0.1 or less for inducers, depending on suction conditions, as can be seen from its relationship to suction-specific speed:

$$\Omega_{ss} = \frac{\Omega \sqrt{Q}}{(g\,NPSH)^{3/4}} = \sqrt{\pi \phi_e \left(1 - \frac{r_s^2}{r_e^2} \right)} \Big/ (\tau/2)^{3/4} \tag{50}$$

where the cavitation coefficient τ (cf. τ_2 in Eq. 36) is defined in terms of the eye speed $U_e = \Omega r_e$ (Table 1). τ is related to ϕ_e through empirical correlations, such as those given in Table 1. (Gongwer's[13] values for the correlation factors k_1 and k_2 apply to large pumps. The larger "typical" values shown for 3% breakdown apply to the more common smaller sizes. The inducer correlation is a curve fit to the data of Stripling and Acosta[14] for the breakdown value of τ.) Thus one can solve for ϕ_e from a given suction-specific speed and, through Eq. 49, obtain the eye size. However, the value of ϕ_e at the BEP or design point rarely exceeds 0.3, regardless of how much *NPSH* is available. This ϕ_e-limit therefore applies to impellers that follow and are in series with the first stage in a multistage pump. These are variously referred to as "series" or "intermediate" stages. (Slurry pump impellers are an exception to this guideline, for then the relative velocity is minimized to avoid excessive wear. In this case ϕ_e can be as high as 0.4 and *NPSHA* is generally more than adequate for these slow-running machines.)

b) The exit radius r_2 (or diameter D_2). This is found from head-coefficient ψ by means of the equation for r_2 in Figure 12. The upper curve for ψ can be used unless detailed performance analysis or a desired non-typical performance characteristic curve indicates otherwise. Eq. 46 can be used for specific speeds Ω_s greater than 1.6 ($N_s > 4373$), where the maximum radius $r_{t,2}$ is computed per the previous discussion accompanying that equation.

c) The exit width b_2. The equation for exit passage width b_2 in Figure 12 can be used for radial-outflow and mixed-flow impellers, r_2 being located halfway across the passage. This

TABLE 1 *NPSH* correlations

$$\tau \equiv \frac{NPSH}{U_e^2/2g} \qquad \Omega_{ss} = \frac{\sqrt{\pi\phi_e\left(1-\frac{r_h^2}{r_e^2}\right)}}{(\tau/2)^{3/4}}$$

For breakdown in pressure rise due to two-phase activity in pump

a) Impellers (Gongwer[13]) $\tau = k_1 \frac{V_e^2}{2g} + k_2 \frac{W_{1,sh}^2}{2g}$

$$NPSH_{3\%} = \overbrace{\left(\frac{V_{1,sh}}{V_e}\right)^n \frac{V_e^2}{2g}}^{k_1} + k_2 \frac{W_{1,sh}^2}{2g}$$

$(V_{0,1} = 0)$: $\boxed{\tau_{3\%} \equiv \frac{NPSH_{3\%}}{U_e^2/2g} = (k_1 + k_2)\phi_e^2 + k_2}$

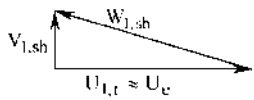

$$\phi_e = \frac{V_e}{U_e} - \frac{Q/A_e}{\Omega r_e}$$

	Gongwer[13] (Large pumps)	Typical (3% breakdown)
k_1	1.4	1.69
k_2	0.085	0.102

b) Inducers (curve fit to the data of Stripling & Acosta[14])

$$\tau = 0.02 + 0.02\left[\log_{10}\left(\frac{\phi_e \sin\beta_{1,b,sh}}{1+\cos\beta_{1,b,sh}}\right) + 3\right]^{3.5}$$

involves the exit flow coefficient or meridional velocity ratio $\phi_i = V_{m,2}/U_2$, the lower curve of Figure 12 being for typical values of this quantity. The "openness" factor ε allows for blockage due to blade thickness and to the buildup of boundary layers on the surfaces of the passageways (blades and hub and shroud). The value of ε is generally between 0.8 and 0.9, the higher figure applying to larger machines. For axial-flow impellers or propellers and inducers, a choice of the hub-to-tip radius ratio at the exit defines the passage width instead. This ratio decreases with specific speed from about $\frac{2}{3}$ at the right end of Figure 12 to $\frac{1}{3}$ or less at the highest specific speeds.

d) Hub and shroud profiles. With the eye and the outlet sizing established, the two are connected by specifying the hub and shroud profiles. Some texts illustrate the variation of hub and shroud profiles with specific speed[15]. Although these are excellent guidelines coming from experience, what follows is the approach one would take to synthesize these

shapes on the basis of fundamental fluid dynamical considerations, at the same time taking experience into account. Referring to Figure 13, an acceptable geometry can be achieved by following these guidelines:

i. Maintaining the meridional flow area $2\pi r_{b,1}b_1$ at the blade leading edge at about the same as it is at the eye, namely $\pi(r_e^2 - r_s^2)$, but then gradually increasing it versus meridional distance to the generally larger value already established at the exit, namely $2\pi r_2 b_2$.

ii. Choosing the minimum radius of curvature R_{sh} of the shroud to be about half the radial opening at the eye. This avoids excessive local velocity $V_{1,sh}$ at the blade leading edge. This has two consequences. Shaping the impeller blades to match a widely varying meridional approach velocity can complicate the construction of these blades. Also, on first-stage impellers, if $V_{1,sh}$ is too great, the local pressure at that location will be closer to the vapor pressure, increasing the required *NPSH* (or $NPSH_{3\%}$). This is due to a larger resulting value of the empirical factor k_1, presented in Table 1 as the n^{th} power of the velocity ratio $V_{1,sh}/V_e$. Single-phase theory would require that the exponent $n = 2$, but two-phase activity in the pump reduces the local pressure reduction that a single-phase application of Bernoulli's equation would indicate.

Figure 14 is a plot of the meridional streamlines in the space between the hub and shroud surfaces of the first-stage impeller of a high-energy boiler feed pump in the absence of blades. This was obtained from a computer solution via Katsanis' program[16] of the inviscid axisymmetric flow field, which is governed by the following equation:

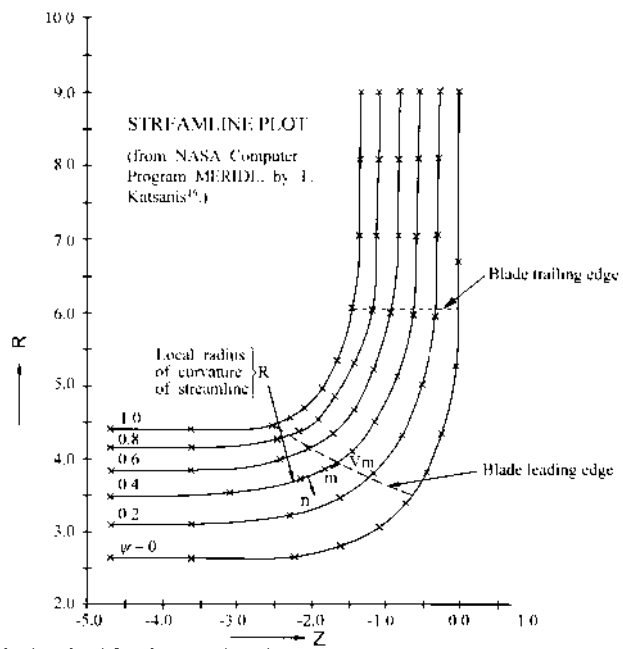

ψ = Stream function or fraction of total flow that passes inward of the correspondingly numbered meridional streamline.

FIGURE 14 Axisymmetric flow analysis for the distribution of meridional velocity V_m along the blade leading edge (Eq. 51a)

$$\frac{dV_m}{dn} = \frac{V_m}{R} \tag{51a}$$

As the average value of V_m at the blade leading edge is about the same as its average V_e in the eye, $V_{1,sh}$ can be estimated from the finite-difference form of this equation, which expresses the change in V_m from shroud to hub in terms of an average radius of curvature R of the meridional streamlines across the passage of width Δn from shroud to hub in the n-direction (normal to the streamlines in Figure 14):

$$\frac{\Delta V_m}{\overline{V_m}} = \frac{\Delta n}{\overline{R}} \tag{51b}$$

The estimated average R in Figure 14 is about twice the passage width Δn; so, by the estimate of Eq. 51b, $\Delta V_m / V_e = \frac{1}{2}$. If half this difference is between V_e and $V_{1,sh}$, then $V_{1,sh}/V_e \approx 1.25$. The computer solution of the inviscid axisymmetric-flow Eq. 51a in this bladeless passage yields $\Delta V_m / V_e = 0.73$ and $V_{1,sh}/V_e = 1.45$ at this location[16]. Now, referring to Table 1, raising $V_{1,sh}/V_e$ to the power 1.4 would produce the typical value of 1.69 given for k_1, which implies that the exponent $n \approx 1.4$. However, two real effects operate to bias $V_{1,sh}/V_e$ toward lesser values; namely, a) greater loss of total pressure of flow entering the impeller along the shroud—due to wall friction and higher velocity, and b) shifting of the flow away from the shroud due to the presence of the impeller blades, which in conventional designs present the incoming flow with the greatest incidence at the hub. This serendipitous state of affairs tends to bring the value of n back toward 2. Moreover, the above estimate of $V_{1,sh}/V_e \approx 1.25$ from Eq. 51b is more typical of the flow for which designers tend to set the impeller blades at the inlet.

These results are strongly influenced by the radius of curvature at the shroud R_{sh}, which in Figure 14 is about half of the passage width Δn. This accords with the guideline for R_{sh}.

iii. Shaping the hub profile compatibly with the guidelines as stated earlier. This is best done after making an initial estimate of the shroud profile as outlined previously. The distribution of meridional flow area from the eye to the exit should then be specified. From this, a hub profile will emerge. As seen in Figures 13 and 14, the hub of a radial-outflow impeller becomes essentially radial over the outer portion of its extent. If this does not result from this procedure, appropriate adjustments can be made to the shroud profile and the process repeated.

iv. For a high-specific-speed, axial-flow impeller, or inducer, the hub profile is often a cone or a reverse curve between a smaller radial location at inlet to a larger one at outlet, the latter radius decreasing with increasing specific speed as mentioned earlier. A cone or cylinder for the shroud profile is often found in such machines.

e) Construction of the blades. The blades are designed by i) selecting the locus of the leading and trailing edges in the meridional plane, ii) establishing the surfaces of revolution (streamwise lines in the meridional plane) from inlet to outlet along which the construction proceeds, iii) selecting the inlet angles, iv) selecting the outlet angles, v) establishing the number of blades, and vi) obtaining the blade coordinates from inlet to outlet:

i. *Leading and trailing edge loci.* If every point along the leading and trailing edges is revolved about the axis of rotation so as to lie in one meridional plane, the loci of these edges appear as shown in Figure 13 or 14. The outer or shroud end of the blade leading edge is positioned at or near the minimum radial location; that is, at or near the eye plane, whereas the inner or hub end is typically well back and largely around the corner along the hub profile. These locations are desirable; first, at the shroud, because the absolute velocity V (typically $= V_m$) approaching the blade begins to decelerate beyond the eye plane, so starting the blade ahead of this decelerating region tends to

prevent separation of the fluid from the shroud surface due to the pumping action in the blade channels[17]; and secondly, being far enough along the hub in the streamwise direction to avoid impractical blade shapes (excessive twist, rake, and so on) that would make both the construction and the flow inefficient. The locus of the blade trailing edges is normally straight in the meridional plane and is axial in orientation for most centrifugal pumps. At the higher specific speeds, this locus becomes more and more slanted until it takes on the nearly radial orientation it has for a propeller (Figure 9).

ii. *Surfaces of revolution for blade construction.* Developing the coordinates of the blades along three streamwise surfaces of revolution—the hub, mean, and shroud, whose intersections with the meridional plane appear as streamwise lines in that plane—usually provides a sufficient framework for shaping the blades of an impeller. However, for high specific-speed impellers, where the passage width in the meridional plane Δn (Figure 14) is large (about equal to or greater that the meridional distance from leading to trailing edge), definition along two intermediate surfaces of revolution is also needed to achieve a satisfactory design.

The "mean" line is one that is representative of the flow from a one-dimensional standpoint as well as for the construction of the blades. Precisely, this is the mass-averaged or "50%" streamline (that is, the streamline for $\psi = 0.5$ in Figure 14)—which evenly divides the mass flow[17]. This line is reasonably and conveniently approximated by the "rms streamline;" that is, the line that would result in a uniform meridional velocity distribution from hub to shroud and therefore equal areas $2\pi r\Delta n$ normal to the meridional velocity component V_m. In this case, Δn $(= \Delta b)$ is the spacing between the rms streamline and the hub or shroud line. This would put each point on the mean line at the root mean square radial position along a true normal to the meridional streamlines; hence, the "rms" terminology.

iii. *Inlet blade angles.* The blade angles are set to match the inlet flow field. This is done where each of the previously chosen surfaces of revolution (that intersect the meridional plane in the streamwise lines just described) crosses the chosen locus of the blade leading edges in the meridional plane. At each such crossing point, an inlet velocity diagram of the type shown in Figure 3 is plotted in a plane tangent to the surface of revolution at that point. (Figure 3, representing a purely radial-flow configuration, is a view of such a plane, as the surfaces of revolution are then simply disks.) Each such velocity diagram or triangle contains a specific value of the angle $\beta_{f,1}$ between the relative velocity vector W_1 and the local blade speed vector $U_1 = \Omega r_1$.

The corresponding blade angle $\beta_{b,1}$ between the mean camber line of the blade and the circumferential direction is set equal to $\beta_{f,1}$ or slightly higher than this to allow for the higher $V_{m,1}$ caused by non-zero blade thickness at the leading edge and to allow for higher flow rates that may be called for at off-design conditions. To construct the triangle, one first plots U_1 and then $V_{m,1}$, which is taken from an analysis such as that of Figure 14 (altered as noted previously for the effect of the blades) or is chosen as the mean value $Q/2\pi r_{b,1}b_1$ (Figure 13) at the rms streamline. It is adjusted from experience at the shroud and hub. Likewise, if any prewhirl $V_{\theta,1}$ is delivered to the impeller, it must be taken into account as illustrated in Figure 3.

iv. *Outlet blade angles.* Whereas the inlet velocity diagrams enable the designer to correctly set the blades to receive the incoming fluid with minimum loss, the outlet velocity diagram displays the evidence—through the magnitude of the circumferential velocity component $V_{\theta,2}$ that the intended head will be delivered by the pump in accordance with Eq. 15c. As shown in Figure 3, $V_{\theta,2}$ is determined—for the given impeller tip speed U_2—by the exit relative flow angle $\beta_{f,2}$ in conjunction with the exit meridional velocity component $V_{m,2}$. This value of V_m is somewhat larger than that given by Eq. 16 because of a) blockage due to blade thickness and boundary layer displacement thickness and b) the presence of any leakage flow Q_L (Figure 2 and Eq. 11) that may also be flowing through the impeller exit plane or Station 2.

Well inward of the exit plane, the direction of the one-dimensional relative velocity vector W can be assumed to be parallel to the blade surface; however, in the last third

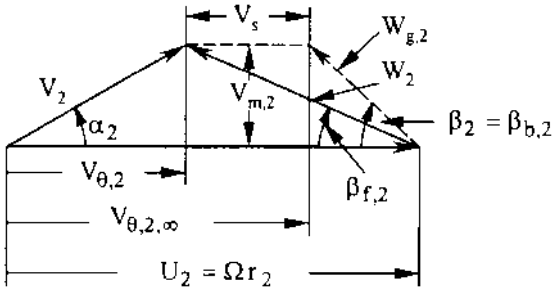

FIGURE 15 Impeller outlet velocity diagram

of the passage, the blade-to-blade distribution of the local relative velocity changes due to the unloading of the blades at the exit. This produces a deviation of the direction of W_2 from that of the blade. This deviation, called "slip" in pumps, results in less energy being delivered to the fluid by the impeller than would be the case if there were "perfect guidance" such as would occur with an infinite number of blades. Accordingly, in the outlet velocity diagram of Figure 15, the relative flow angle β_f is less than the blade angle β_b. This deviation is quantified by the "slip velocity" V_s. The magnitude of V_s depends on the distribution of loading along the blades from inlet to exit and therefore on the geometry of the flow passages and the number of blades. (Without slip, W_2 is the same as the "geometric" relative velocity $W_{g,2}$ shown in the figure.) The slip factor $\mu = V_s / U_2$—typically between 0.1 and 0.2—was determined theoretically by Busemann for frictionless flow through impellers with logarithmic-spiral blades (constant-β from inlet to exit) and a two-dimensional, radial-flow geometry with parallel hub and shroud[18]. Applicability of this theory to typical impellers, despite the differences in geometry and the real fluid effects, was found to be good by Wiesner, who represented Busemann's results by the following convenient approximation[19]:

$$\mu \equiv \frac{V_S}{U_2} = \frac{\sqrt{\sin \beta_2}}{n_b^{0.7}} \tag{52}$$

A broader, empirical slip correlation for pumps was developed by Pfleiderer, taking into account impeller geometry and blade loading, as well as the influence of the downstream collecting system (volute or diffuser)[20]. Pfleiderer computes the slip velocity as the product of a slip factor p and the impeller exit tangential velocity $V_{\theta,2}$, where p is computed as shown in Table 2. This table also contains a simple example; namely, a radial flow impeller of a volute pump, for which the resulting value of μ is 0.1826—versus 0.1498 via Eq. 52; however, in this case the latter result is low by about 15 percent. A study of the Busemann plots in Wiesner's paper yields $\mu = 0.18$. Yet, if this had been a vaned-diffuser pump, Pfleiderer would have predicted $\mu = 0.1468$ for the same impeller, as it would have delivered more $V_{\theta,2}$ for the same $\beta_{b,2}$, $W_{g,2}$, and, therefore, $V_{\theta,2}$, (Figure 15). This stems from the factor "a" in Table 2 having the value 0.6 (for a vaned diffuser) instead of 0.8 (for a volute). So by this combination of circumstances—and in this example—Eq. 52 describes the slip of a diffuser pump impeller. But, despite the simplicity of Eq. 52, Pfleiderer's method (Table 2) would appear to be a more rational, comprehensive, and satisfying method for estimating slip in real pumps.

So, to find the outlet blade angle, the designer begins by deciding upon the required value of $V_{\theta,2}$; finds the exit flow angle and other elements of the diagram assuming the existence of slip. Next, the designer computes the slip and then obtains the value of the outlet blade angle $\beta_{b,2}$. The process is iterative because the forementioned blockage depends on the blade angle as well as the thickness.

TABLE 2 Pfleiderer's slip formula

Slip Velocity V_s:

$$V_S = p\,V_{\theta,2}$$

$$\left[\Rightarrow \frac{V_{\theta,\infty,2}}{V_{\theta,2}} = 1 + p\right]$$

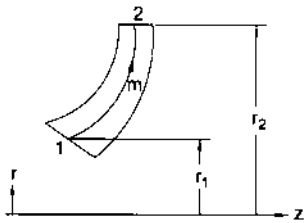

where $$p = \frac{\psi' r_2^2}{z\int_1^2 r\,dm}$$

and where $\psi' = a \times (1 + \sin\beta_2)$ (or $\beta_{b,2}$)

$$\left\{\Rightarrow \int_1^2 r\,dm = \frac{1}{2}\left(r_2^2 - r_1^2\right)\right.$$

$$\left.= \left(\frac{r_2 + r_1}{2}\right) \times (r_2 - r_1)\right.$$

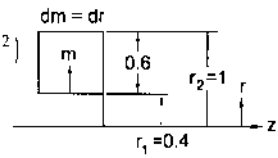

and a $-$ { 0.6 Diffuser (vaned); 0.65 – 0.85 Volute; 0.85 – 1.0 Vaneless diffuser }

Example: $r_2 = 1$; $r_1 = 0.4$; $V_{0,2} = \frac{U_2}{2}$;
$z = 7$; $\beta_2 = 20°$.
$a = 0.8$ (volute)
$\psi' = 0.8 \times (1 + 0.342)$

$$\left\{p \equiv \frac{V_S}{V_{\theta,2}} = \frac{0.8 \times (1 + 0.342) \times 1^2}{7 \times \frac{1 + 0.4}{2} \times 0.6} = 0.3652\right.$$

$$\left.\mu \equiv \frac{V_S}{U_2} = p \times \frac{V_{\theta,2}}{U_2} = 0.3652 \times \frac{1}{2} = 0.1826\right.$$

v. *Number of blades.* The choice of the number of impeller blades is influenced by a) interaction of the flow and pressure fields of the impeller and adjacent vaned structures such as the volute tongues or diffuser vanes and b) the need to maintain smooth, attached—and therefore efficient—fluid flow within the impeller passages. The effect of the number of blades on the interaction phenomenon is addressed in the latter part of this section under the topic of high-energy pumps, where this issue becomes critical. Smooth, attached flow is assured if the product of the number of blades and their total arc length ℓ along a given meridional streamline, as illustrated in Figure 16, is of sufficient magnitude. Divided by a representative circumference on that streamline, usually that of the impeller outer diameter (OD), this product is called the solidity σ:

$$\sigma = \frac{n_b \times \ell}{2\pi r_2} \tag{53}$$

In practice, solidity varies from about 1.8 at low specific speed ($\Omega_s < 0.4$ or $N_s < 1093$) to slightly less than unity at $\Omega_s = 3$ ($N_s = 8199$). For example, Dicmas' curve[21] is

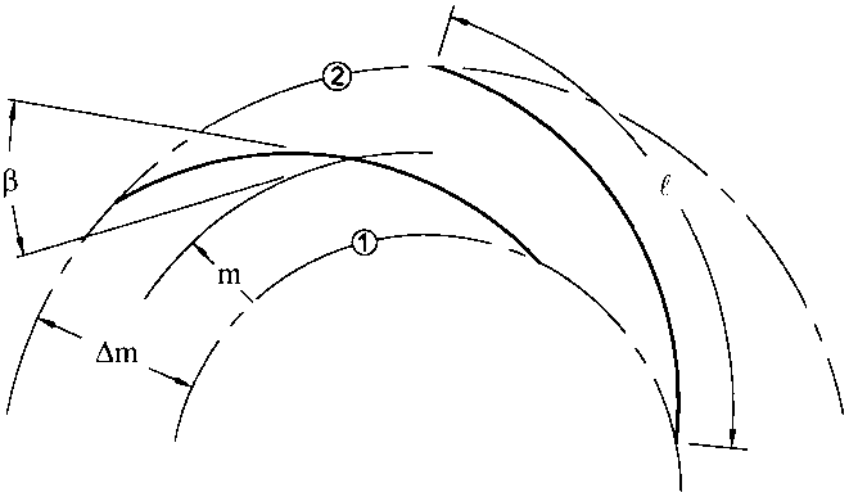

FIGURE 16 Intersection of impeller blades with mean surface of revolution

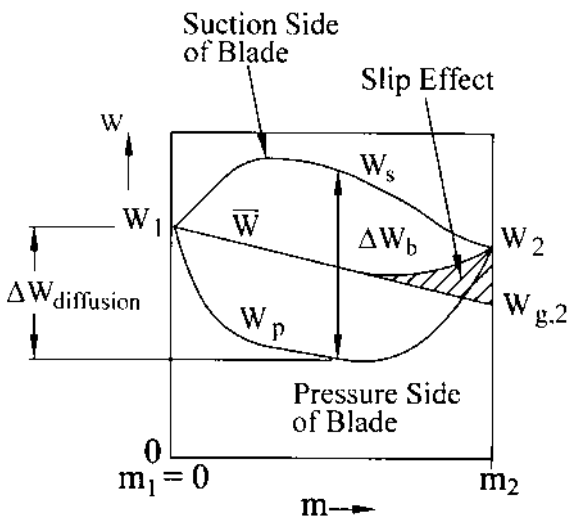

FIGURE 17 Relative velocity distributions.

useful for $\Omega_s > 1$ ($N_s > 2733$). This limits the relative velocity reduction that occurs on the blade surfaces. Illustrated in Figure 17, this reduction or diffusion arises from the loading on the blades expressed in terms of the blade-to-blade relative velocity difference ΔW_b:

$$W_s - W_p(=\Delta W_b) = \frac{2\pi}{\Omega n_b} \times \frac{V_{m,o}}{\overline{W}} \frac{d(UV_\theta)}{dm} \tag{54}$$

$V_{m,o}$ is the local meridional velocity component neglecting blockage. (One-dimensionally, $V_{m,o}$ is the value of V_m found from Eq. 16, where the radius r is that from the axis of rotation to the center of the circle of diameter b in Figure 8, which in turn lies on an imaginary line in Figure 8 that is normal to the hub, shroud, and intermediate stream surfaces.) Here, ΔW_b emerges by applying Bernoulli's equation [Eq. 21 with no change in radius (that is, no change in U) or loss as one traverses from pressure side to suction side of the passage] to the static pressure difference $p_p - p_s$ arising from the delivery of angular momentum to the fluid (Eq. 26). This in turn results from the application of the shaft torque to the blades. It is also assumed in the derivation of Eq. 54 that the *blade-to-blade average relative velocity W lies halfway between the surface velocities* W_s *and* W_p, (which would exist just outside the boundary layers on the blades,) as illustrated in Figure 17. This is a good assumption for efficient flow well within a bladed channel[22]. ΔW_b is inversely proportional to the solidity because, on the average, from inlet to outlet, Eq. 54 becomes

$$\overline{W_s - W_p} = \overline{\Delta W_b} \approx \left(\frac{2\pi r_2 \sin\beta}{n_b \Delta m}\right)\Delta\left(\frac{r}{r_2}\ V_\theta\right) \tag{55}$$

where it can be seen from Figure 16 and Eq. 53 that the fraction involving the number of blades n_b is the reciprocal of the solidity σ because

$$\ell = \Delta m/\overline{\sin\beta} \tag{56}$$

For unconventional impeller geometries, the foregoing solidity guidelines may be inadequate to assure efficient flow. For any geometry, though, the concept of a diffusion factor D, utilized by NACA researchers[23] to assess stationary cascades of airfoils can be employed. In view of Eqs. 53–56, their equation for D takes the following form for both axial- and non-axial-flow geometries, rotating or not:

$$D = 1 - \frac{W_2}{W_1} + \frac{\Delta\left(\frac{r}{r_2}\ V_\theta\right)}{2\sigma W_1} \tag{57}$$

This can be deduced from Figure 17 as follows:

$$D = \frac{W_1 - W_2}{W_1} + \frac{\overline{\Delta W_b}}{2W_1}\left(\approx\frac{\Delta W_{\text{diffusion}}}{W_1}\right) \tag{58}$$

Then, Eq. 57 is obtained through the definitions of the average value of ΔW_b (Eq. 55 with Eq. 56) and σ (Eq. 53). NACA researchers found that losses increase rapidly if $D > 0.6$. However, many centrifugal pump impellers have virtually the same value of relative velocity W at in and at outlet—along the rms streamline (Figure 17), so D from Eq. 57 is less than 0.6 on the rms streamline and even negative along the hub streamline. This situation was encountered in accelerating (turbine) cascades and led to the use of local diffusion factors, one for each side of the blade, namely D_p and D_s. Here, inspection of Figure 17 and Eq. 58 leads to

$$D_p = 1 - \frac{W_{p,\,\min}}{W_1} \quad ; \quad D_s = 1 - \frac{W_2}{W_{s,\,\max}} \tag{59a and b}$$

where the 0.6 limit applies individually to D_p and D_s—or to the sum of the two, in which case the limit is 1.2. Eqs. 59a and 59b, therefore, constitute a more useful form

of the diffusion factor concept for assessing the blade loading and the choice of the number of blades in centrifugal pump impellers[24].

Finally, the total blade length or number of blades, should not exceed that necessary to limit the diffusion as just described, as this adds unnecessary skin friction drag, which causes a reduction in efficiency. Thus the solidity values given in conjunction with Eq. 53 should not be appreciably exceeded, unless blade load needs to be reduced to lower levels, as with inducers to limit cavitation[8] or impellers for pumps that must produce lower levels of pressure pulsations.

vi. *Development of the blade shape.* Blades are developed by defining the intersection of the mean blade surface (really an imaginary surface) or camber line on one or more nested surfaces of revolution. Two such surfaces are formed by the hub and shroud profiles. If the blade shape is two-dimensional (that is, the same shape at all axial positions z), the mean blade surface is completely defined by constructing it on only one such surface of revolution. Generally, however, the shape is three-dimensional and is a fit to the shapes constructed on two or more of these surfaces of revolution; namely, the hub and shroud and usually at least one surface between them. After this final shape is known, half of the blade thickness is added to each side. (Sometimes the full blade thickness is added to one side only, meaning that the constructed surface just mentioned ends up—usually—as the pressure side of the finished blade rather than the mean or "camber" surface. The effective blade angles are then slightly different from those of the pressure side used in the construction process.) The construction along a mean surface of revolution is illustrated in Figure 18. The distribution of the local blade angle β (or more precisely, β_b) is found first by either the *"point-by-point"* method or the *conformal transformation* method—both of which yield the polar coordinates of the blade, r, θ, and z. These coordinates also depend on the chosen shapes of the intersections of the surfaces of revolution with the meridional plane; that is, the hub, shroud, and mean meridional "streamline" or rms line, as in Figure 18c, and the fact that, on the surface of revolution Figure 18a, $\tan \beta = \text{arc } bc/\text{arc } ac = dm/dy$. The elemental tangential length dy (= arc ac) is the same on both the surface of revolution (Figure 18a) and in the polar view (Figure 18b). From Figure 18b, it is seen that $dy = rd\theta$, so the "wrap" angle θ is found from

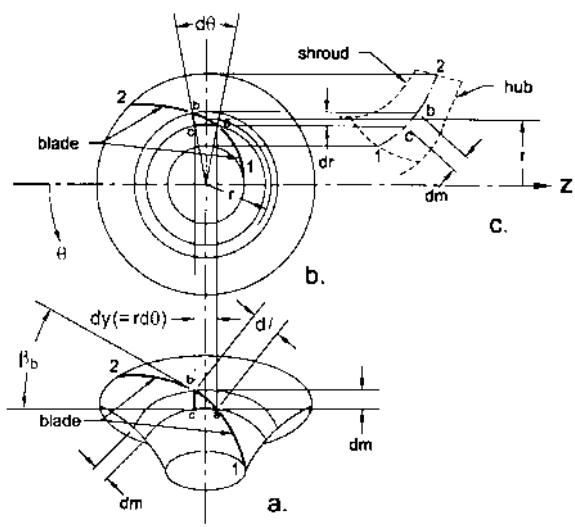

FIGURE 18 Blade construction: a) view of construction surface of revolution; b) polar view; c) meridional view

$$\tan \beta_b = \frac{dm}{rd\theta} \tag{60}$$

and r and z are found from the fact that the coordinate m along each of the construction surfaces is a function of r and z (Figure 18c).

If the blade is two-dimensional, its mean surface consists of a series of straight-line axial elements, each having a unique r and θ at all z. Such a blade is typical of low-specific-speed, radial-flow impellers, and can be easily constructed by the *"point-by-point"* method. Here, one specifies the distribution of W_g—often linear as in Figure 17—after determining the hub and shroud profiles and the corresponding distribution of V_m[15]. In effect, one obtains the distribution of the blade angle β_b by constructing a velocity diagram like the one in Figure 15 at every m-location from inlet (1) to outlet (2) in Figure 18c, dealing only with the "geometric" or non-deviated velocities, in order to get a smooth variation of the blade angle β_b vs m. Allowance is made for blockage due to the thickness of the blades and the displacement thickness of the boundary layers in the passage. The resulting wrap angle θ for each m-point—as well as the corresponding r and z—is then found from Eq. 60. (For convenience in designing the blades, the construction angle θ is often taken as positive as one advances from impeller inlet to exit. For most impellers, this turns out to be opposite to the direction of rotation; and θ is taken in the direction of rotation for most other purposes of pump design and analysis.) As discussed previously in Paragraph iv and illustrated in Figure 17, the actual flow will deviate from the resulting blade via the "slip" phenomenon.

The point-by-point method allows the designer to exercise control over the relative velocity distributions on the blade surfaces (Eq. 54 and Figure 17) via specification of the distribution of W_g or other velocity component in Figure 15; for example, V_{θ_2}. This becomes more important if an unconventional impeller geometry is being developed[17].

The point-by-point method can also be used for three-dimensional blades. A simple approach in this respect would be to use this method to determine the blade shape along the rms- or 50%-streamline (that is, on the mean surface of revolution depicted in Figure 18). The shapes on the other streamlines, generally the hub and the shroud, can also be found by this method. The resulting overall blade shape, however, is subject to the condition that the resulting wrap $\theta_2 - \theta_1$ cannot greatly differ on all streamlines without the blade taking on a shape that is difficult to manufacture and which may turn out to be structurally unsound or create additional flow losses. This is because the final blade shape is the result of stacking the shapes that have been established on the nested stream surfaces defined by these meridional streamlines. Blade forces due to twists arising from this stacking could modify the expected flow and cause unexpected diffusion losses.

One way to generate blade shapes along the hub and shroud that have the same (or nearly the same) wrap as that obtained from point-by-point construction of the blade on the mean surface of revolution is to establish the desired inlet and outlet blade angles β_b on each such surface and then mathematically fit a smooth shape $y(m)$ to these end and wrap conditions, where y is the tangential coordinate seen in Figure 18 and defined in Figure 19. A conformal representation of the shapes of the blades resulting from such a procedure on each of the three surfaces is seen in Figure 19. These shapes are sometimes called "grid-lines" or simply "grids"—from the description of the graphical procedure that relates these shapes in the conformal representation to those on the actual, physical surfaces[4]. In such a representation, the blade angles are the same as they are on the physical surface of revolution because $\tan \beta = dm/dy$ and $dy = rd\theta$, also yielding Eq. 60.

If the associated distributions of W_g and V_m are smooth, one can expect to have a satisfactory result if these conformal representations are also smooth. Thus, many skilled designers bypass the computations just described for the point-by-point method and use the *conformal transformation* method of blade design. Here, one simply establishes the grid-line shapes by eye in the conformal plane of Figure 19, specifying the blade angles β at inlet and outlet by the previous procedures as the starting point for

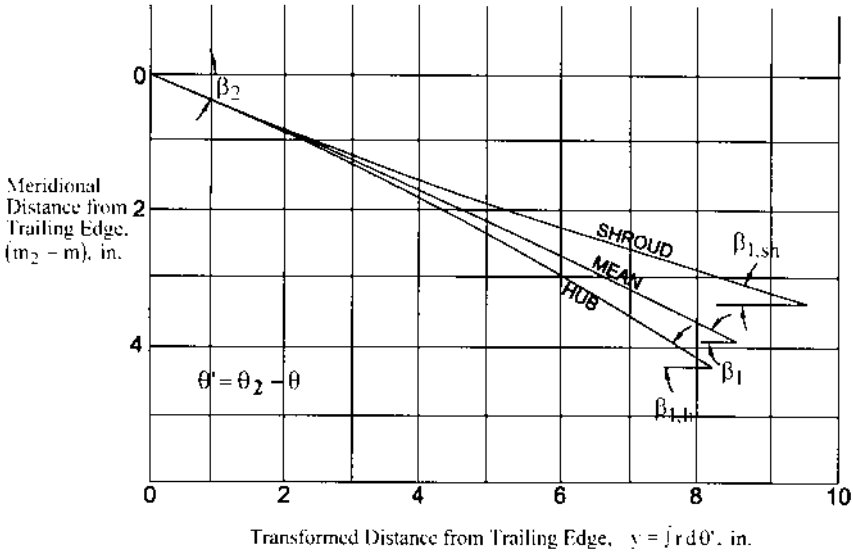

FIGURE 19 Conformal transformation of blade shape: "grid-lines"

drawing each grid-line. This conformal blade shape is then transformed onto the physical surface, the differential tangential distance dy becoming $rd\theta$ on the physical surface (Figure 18) and the differential meridional distance dm being identical in both the conformal and physical representations. If the resulting blade shape appears to be unsatisfactory, the designer repeats this process, possibly first altering the hub and shroud profiles or the blade leading and trailing edge locations on these profiles and recomputing the β's.

Designing the Collector The fluid emerging from the impeller is conducted to the pump discharge port or entry to another stage by the collecting configuration, which can employ one or more of the following elements in combination: a) *volutes*, which can be used for designs of all specific speeds, b) *diffuser or stator vanes*, which are often more economical of space in high-specific-speed single-stage pumps and in multistage pumps, and for the latter, c) *return or crossover passages*, which bring the fluid from the volute or diffuser to the eye of the next-stage impeller. Generally, the most efficient impeller has a steady internal relative flow field as it rotates in proximity to these configurations. This is assured by all of these elements because they are designed to maintain uniform static pressure around the impeller periphery—at least at the design point or BEP. An exception to this rule is the concentric, "doughnut"-type, "circular-volute" collector, which is used on small pumps or in special instances where the uniform pressure condition is desired at zero flow rate.

The proximity of stationary vanes in these collecting configurations to the impeller must be considered in their design. Called "Gap B," the meridional clearance between the exit of the impeller blades and adjacent vanes ranges from 4 to 15 percent of the impeller radius, volutes having higher values in this range than diffusers, and pumps of higher energy level requiring the larger values. If these gaps are too small, the interactions of the pressure fields of the adjacent blade and vane rows passing each other can cause vibration and structural failure of impeller blades, diffuser vanes, and volute tongues.

a) Volutes. A volute is built by distributing its cross-sectional area on a "base circle" that touches the tongue or "cutwater" and is meridionally removed from the impeller exit by

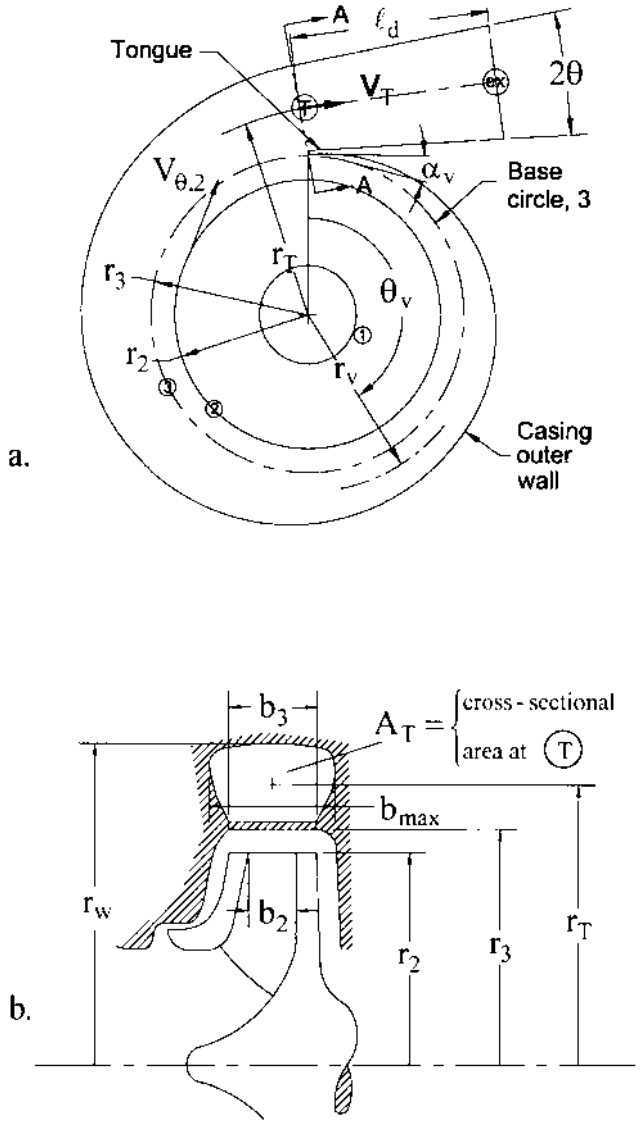

FIGURE 20 Volute casing: a) polar view; b) meridional view including Section A-A of throat T

Gap B. (For radial-discharge impellers, as in Figure 20, this is a radial gap, and the base circle has radius r_3.) Beginning at the tongue, the cross-sectional area A_v of the volute passage is zero, but it increases with angle θ in the direction of rotation, ending up at area A_T in the "throat" T, as depicted in Figure 20. Worster demonstrated that the desired peripheral uniformity of static pressure can be achieved if the product rV_θ is constant

everywhere in the volute[25]. One-dimensionally, this means that $r_T V_{\theta,T} = r_2 V_{\theta,2}$; and, if the velocity V_T is essentially tangential (in the θ-direction), $r_T V_T \cong r_2 V_{\theta,2}$. The diffusion or reduction of the velocity V from the impeller periphery at r_2 to the larger r_T of the throat produces a static pressure increase above that at the impeller exit; however, friction losses in the volute would cause a reduction in static pressure around the impeller at r_2 from tongue to throat unless the throat area $A_T = Q/V_T$ is slightly enlarged, creating a little more diffusion to compensate for this loss. Thus, in practice, at the BEP,

$$r_T V_T \cong (0.9 \text{ to } 0.95) \times r_2 V_{\theta,2} \tag{61}$$

At off-BEP conditions, the volute will be either too large or too small and Eq. 61 will not be satisfied. When the flow coefficient (or Q/N) drops below the BEP value, there will be excessive diffusion and an increase of static pressure around the volute from the zero area point around to the maximum area point at the throat. Proceeding around further, past the throat, a sudden drop in pressure occurs across the tongue to bring the pressure back to what it was at the starting point[25]. The opposite situation occurs above BEP.

Each of these off-BEP circumferential static pressure distributions is properly viewed as the consequence of a mismatch between the head-versus-flow characteristics of the impeller and volute[26]. For the impeller, there is the falling, straight, H_i-versus-Q line or "impeller line" of Figure 6, whereas the volute characteristic or "casing line" would be a straight line starting at the origin of Figure 6 and crossing the impeller line at the match point, which is generally at or close to the BEP flow rate. This casing line is straight because the throat velocity V_T varies directly with flow rate Q and, through Eq. 61, directly with the ideal head H_i—because $\Omega \times r_2 V_{\theta,2} = H_i$ (Eq. 15b for $V_{\theta,1} = 0$). In other words, the same volute could be optimum at a different value of Q if it were paired with another impeller whose H_i-versus-Q line crossed this same casing line at that different Q.

To essentially eliminate the consequent radial thrust on the impellers of large pumps at off-BEP conditions, a double volute is used; that is, there are two throats, 180 degrees apart, there being either two discharge ports or a connecting "back channel" to carry the fluid from one of the throats around to join the flow emerging from the other—to form a single discharge port.

The value of the volute cross-sectional area A_v at a given polar position θ_v can be found for the portion of the total pump flow rate Q being carried in the volute at that θ_v-position together with the condition rV_θ = constant versus radius. This will produce a distribution $A_v(\theta)$ that is slightly below a straight-line variation versus θ_v from zero to A_T. Often, the practice is to use the latter straight-line design because this produces larger values of A_v where the hydraulic radius of the volute is small, thus compensating for the greater friction loss in that region through lower velocity—particularly for the smaller pump sizes. The cross-sectional shape of the volute is dictated by the need to make a minimum-loss transition from a small area at the beginning of the volute where the height (as can be deduced from Figure 20b) is much smaller than the width b_3 to the throat, for which the height (to the outer casing wall at r_w) and the width $b_{\max}$ are more nearly equal. Too small an aspect ratio (height/width) decreases the hydraulic diameter too much and increases the loss. There is another transition from the throat through an essentially conical diffuser (which may negotiate a turn) to a larger, circular exit port. This diffuser can be designed with the help of charts of flow elements and will normally have a 7-deg. angle of divergence and a discharge area up to twice that of the throat A_T[27]. Thus, there is a substantial diffusion from the impeller periphery to the pump or stage exit port. This generally produces a static pressure rise in the collection system that is 20 to 25 percent of that of the whole stage.

b) Vaned diffusers. A vaned diffuser is rotationally symmetric and, if properly applied, produces minimal radial thrust over the whole flow rate range of a pump. Although diffusion can be accomplished in a radial outflow configuration without vanes due to the essential constancy of the angular momentum per unit mass rV_θ, one rarely finds a pump with a vaneless diffuser, partly because so much radial distance is needed to effect the reduction of tangential velocity required, as well as the still larger volute needed on single-stage

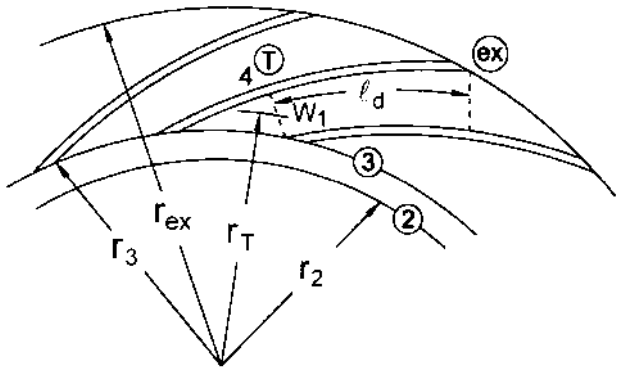

FIGURE 21 Vaned diffuser

pumps to collect the fluid at the exit of such a diffuser. Also, the absolute flow angle α_2 (Figure 15) of the fluid leaving the impeller is usually too small to satisfy the conditions for stall-free flow in a vaneless diffuser[28]. A vaned diffuser, on the other hand, can accomplish the reduction of velocity in a shorter radial distance. Also it can diffuse axially and, to a degree, even with radially inward flow.

Vaned diffusers are similar to multiple volutes in concept, except they are subject to off-design flow instabilities if not shaped correctly. Width b_3 is usually slightly greater than b_2 in order to accommodate discrepancies in the axial positions of impellers that feed them. With reference to Figure 21, "Gap B" ($= r_3 - r_2$) is in effect a short vaneless diffuser, and by the time the fluid has reached the throat (the dashed line at Station 4), it has gained a substantial portion of the static pressure recovery that takes place via diffusion from Station 2 to Station "ex." This "pre-diffusion" is enhanced by the fact that the throat area at Station 4 ($= b_3 w_1$ per passage for parallel-walled radial-flow diffusers) is larger than it is for volutes, the following relation applying to diffusers[29]:

$$r_T V_T \cong 0.8 r_2 V_{\theta,2} \tag{62}$$

Therefore, more diffusion than would result from applying Eq. 61 occurs in a vaned diffuser, the skin friction loss due to an otherwise higher velocity at the throat being offset by an efficient reduction of the velocity up to that point and a lower velocity onward.

The fully vaned portion from throat to exit (Figure 21), which performs most of the rest of the diffusion and associated static pressure recovery of the stage, is designed to perform efficiently and maintain stable flow. For typical radial-flow geometries with parallel walls, the vanes can be of constant thickness and comparatively thin or can thicken up to form "islands." The latter approach usually produces a channel that is two-dimensional with straight sides diverging at an included angle, length-to-entrance width ℓ / w_1, and area ratio A_{ex}/A_T in a combination that avoids appreciable stall[30]. A typical combination is an included angle of $11\frac{1}{2}$ deg., $\ell / w_1 = 4$, and $A_{ex}/A_T = 1.8$, which also applies for vanes of constant thickness, as illustrated in Figure 21. Constant thickness vanes have curvature. This modifies the performance somewhat[31,32], but it allows a smaller overall radius ratio of the diffuser, r_{ex}/r_3.

Also, this ratio r_{ex}/r_3 will be smaller as the *number of vanes* n_v increases. The best experience seems to be with diffusers that have only a few more vanes than the number of impeller blades n_b (n_b rarely exceeds 7 in traditional commercial pumps). For pumps of higher energy levels (or high head per stage, as discussed further on in connection with high-energy pumps), it is important that n_v be chosen so as to avoid a difference of 0 or 1 between n_b and n_v or their multiples—up to at least the third multiple or "order" of each. A difference of 2 should also be avoided for at least the lower orders[33].

At off-design flow-coefficients (or off-design flow rate at a constant speed), the angle α of the absolute velocity vector V (Figure 15) approaching the diffuser will vary; yet, for typ-

ical stages, a wide range of flow coefficient is possible without damaging instabilities, even at high energy levels. This is likely the case because α is rather small at the design point or BEP (except for designs having high specific speed), so variations of the angle that occur with flow changes are within the unstalled performance range of the diffuser vane system.

c) Return passages. Conducting the relatively low-velocity fluid from the diffuser to the eye of the next impeller in a multistage pump is accomplished with return vanes or passages that also deswirl the fluid wholly or partially. Except for development of stall in the diffuser, these passages will not see a changing angle of the approaching velocity vector because the diffuser feeding them is a stationary element. In radial-flow pumps, there is a sharp turn in the meridional plane in order to redirect the fluid inward. The fluid, still possessing a circumferential component of velocity that is greater than the meridional component, actually sees a much gentler turn. However, downstream of this point, a sharp turn of the blades is invariably a feature of a return passage; and this, together with the need to ensure undistorted flow into the following impeller, often dictates that the vane system accelerate the fluid as it approaches the eye. Although losses in the return passages—being related to the low velocity within them—have a minor effect on the overall stage efficiency, the design of such passages must ensure unstalled flow into the impeller in order to avoid the negative impact of a distorted inlet flow on the efficiency and to promote pulsation-free operation of the impeller.

A variety of return-passage geometries exist, some of which are presented in the literature [29,34]. The continuous-vane type is integral with the upstream diffuser, thereby eliminating the entry losses into yet another vane system after the diffuser[4,34]. Improvements in manufacturing technology have made this potentially more efficient approach more viable for radial machinery. The continuous-vane concept is standard practice in the design of mixed-flow "bowl"-type pumps[21]. The diffusing stator vane row that receives the fluid from the impeller of an axial-flow pump—being an axial-flow element itself—possesses the return feature already. Diffusion in axial-flow stators is typically accomplished by a reduction in velocity of about 30 to 40 percent. The actual value is governed by an acceptable level of the diffusion factor, Eq. 57. (A similar reduction in relative velocity is needed for an axial-flow impeller to generate static pressure, as can be seen from Eq. 21. By comparison, centrifugal impellers, on the rms streamline, usually have W_2 about equal to W_1—as seen in Figure 17.)

Axial-Flow Pumps The preceding development, though general, is applicable mainly to centrifugal and mixed-flow pumps. In that procedure, the impellers have appreciable solidity, and original blade shapes are constructed from the viewpoint of one- or two-dimensional channel flow. The collectors are often volutes or non-axial-flow vane systems. Performance is not known a priori and so must be estimated, as outlined further on. On the other hand, the extensive two-dimensional, experimental, axial-flow cascade data amassed by NACA researchers[23] and others enables the designer to adopt existing airfoil blade shapes and so predict the performance with greater confidence. The procedure for utilizing these shapes and the corresponding experimental results has long been the basis for designing axial-flow compressors for gas-turbine engines and is clearly described by Hill and Peterson[35]. This approach is widely used, especially for high-specific-speed, low-solidity axial-flow propeller pumps—in designing both rotating and stationary blade rows. Insights for propeller pump design and performance characteristics can be found in Stepanoff[4].

An exception to this axial-flow pump design approach is the case of inducers. Although they are axial flow pumps, they have high solidity and are usually designed as channel-flow machines. The design philosophy outlined in the preceding paragraphs is applicable, except that the blades usually approximate constant- or variable-pitch helices. Performance prediction is generally accomplished via one-dimensional calculations and the correlations described in the following paragraphs.

PREDICTING THE PERFORMANCE CURVES

The choices made in the foregoing design procedures can and should be verified analytically, the objectives being first to generate the performance characteristic curves for head

and power at constant speed and second to ensure stable behavior of the various systems in which the pump is to be applied. For the first objective, the solution involves analytical or empirical approaches: a) at non-recirculating flow conditions; that is, from flow rates Q somewhat below Q_{BEP} out to the maximum "runout" flow rate, b) at shut-off ($Q = 0$) and low flow, or c) the complete set of curves for a given pump predicted by means of computational fluid dynamics (CFD).

Generating Performance Curves The fluid dynamical limitation on the deceleration of the relative velocity W determines the shape of the head-versus-flow curves. This is inherent in the choice made for the head coefficient ψ in Figure 12, which sizes the impeller and is illustrated in Figure 22. The typical situation of zero (or nearly so) inlet whirl $V_{\theta,1} = 0$ means that the ideal head coefficient ψ_i equals the most significant ratio of the outlet velocity diagram because from Eqs. 15 and 31 (with for $V_{\theta,1} = 0$):

$$\psi_{\text{ideal}} = \frac{U_2^2 \, (V_{\theta,2}/U_2)}{U_2^2} \tag{63}$$

$$\psi = \eta_{HY} \, \psi_{\text{ideal}} = \eta_{HY} \, \frac{V_{\theta,2}}{U_2} \tag{64}$$

Figure 22 illustrates how specific speed Ω_s affects the BEP value of ψ_i and therefore ψ. Overall, only a small reduction of W occurs in most impellers. So, at low Ω_s, the low value of W_1 associated with the small eye relative to the maximum diameter (Figure 9) enables the outlet velocity diagram (Figure 22a) to have a high value of $V_{\theta,2}/U_2$. On the other hand, this ratio drops as Ω_s increases and the eye grows to be as large as the maximum diameter of the wheel. Figure 22b is the result because the value of ψ at shut-off (about $\frac{1}{2}$) is not based on the one-dimensional concept of velocity diagrams but primarily on the pressure generated by solid body rotation of stalled (though recirculating) fluid contained within the impeller. The BEP values of ψ in Figure 22b are consistent with Figure 12 and illustrate why a high-specific-speed impeller has such a substantial "rise to shut-off" of the head curve. This is dramatically illustrated in Figures 8–10 of Section 2.3.1 in which the head curves are normalized to that of the BEP[36].

a) Non-recirculating flows. The BEP efficiency and head can be determined from correlations for typical pumps or from computation of the losses. Fluid dynamic procedures described in this section can be used to determine the shapes of the head and power curves at all flow rates to runout, using the BEP as an anchor point for such computations. For pumps designed conventionally, beginning with Figure 12, Anderson's overall (BEP) efficiency correlation (Eq. 44) as modified in Figure 10 is useful. Other similar charts, especially Figure 6 in Section 2.3.1, are in widespread use. The breakdown of the losses involved, as expressed by Eqs. 8–11, is quantified through the development of the three component efficiencies η_{HY}, η_m, and η_v in Table 3. All three decrease with decreasing specific speed—as might be expected from the charts just mentioned.

This can be seen in the η_{HY}-expression (a) of Table 3 because ψ_i is greater at low Ω_s as discussed relative to Figure 22. Jekat's η_{HY}-expression (b) of the table works surprisingly well, largely because of the flow effect in Figure 9 (explained there as the "size effect" of larger relative roughness and clearances in smaller pumps) and because low Ω_s tends to go hand-in-hand with low flow rate Q.

To compute η_{HY} at $Q \neq Q_{BEP}$ (and, if required, at $Q = Q_{BEP}$ as well), it is necessary to go deeper into the prediction of η_{HY} by developing *expressions for the losses* noted in Eq. 21, which are basically expansions of the expression for the collector loss coefficient ζ_c[26] and for the impeller loss expression (c) of Table 3[37]. In this expression, the incidence loss coefficient k can be obtained from cascade data or developed as a combination of a turning and a sudden expansion loss[4,8,27]. The "pipe-type friction factor" f can be increased to include secondary flow and diffusion losses due to blade loading (or turning[38] of the absolute velocity vector V). The resulting f-value can thus be twice the usual pipe value associated with the skin friction losses in the passage. (The pipe value of f is found from the well-known

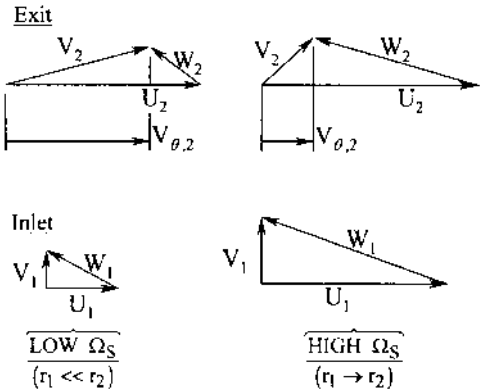

a) velocity diagrams at BEP

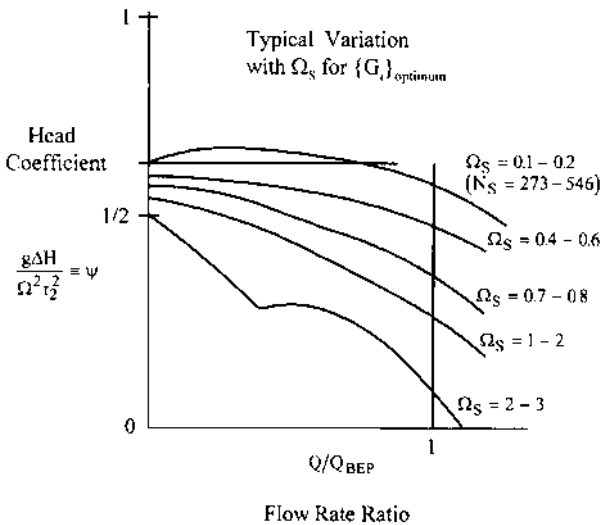

b) head-vs-flow curves

FIGURE 22 Performance versus specific speed: a) velocity diagrams at BEP; b) head-versus flow curves.

pipe friction chart—Figure 31 in Section 8.1—by substituting a representative average passage hydraulic diameter $D_h = 4A_p/\wp$ for the pipe diameter d.) A further increase in this f-value occurs if the impeller is missing one or both rotating shrouds; that is, it is a semi- or fully-open impeller with blade tip leakage losses appearing in the main flow stream[39]. Multiphase flows in pumps often are accompanied by greater than normal hydraulic losses; for example, increasing the concentration of solids in the carrier liquid flowing through a slurry pump increases the f-value still further[40] (see Section 9.16.2).

Quasi three-dimensional (Q3D) analysis[41] affords an assessment of the secondary flow and diffusion losses and gives results similar to inviscid three-dimensional (3D) flow analysis. Q3D analysis starts by solving the 2D meridional (hub-to-shroud) flow field—as in Figure 14, but with blades present. This is followed by a series of 2D blade-to-blade

TABLE 3 Component efficiency expressions developed

A) Hydraulic Efficiency

Breaking up the main flow losses into impeller (including inlet)

and collector losses $\sum_i L_i = L_{imp} + L_c$ and defining $L_c = \zeta_c \frac{V_2^2}{2}$, where ζ_c

is the collector loss coefficient or fraction of $V_2^2/2$ not converted into static pressure rise in the collector, we have (Eq. 10)

$$\eta_{HY} = 1 - \frac{\sum L_i}{\Delta(UV_\theta)} = \underbrace{1 - \frac{L_{imp}}{\Delta(UV_\theta)}}_{\eta_I} - \underbrace{\frac{\zeta_c V_2^2/2}{\Delta(UV_\theta)}}_{\zeta_c\left(\frac{\psi_{i,2}}{2} + \frac{\phi_{i,2}^2}{2\psi_{i,2}}\right)}$$

or, for no inlet whirl ($V_{\theta,1}=0$) $\psi_i = \psi_{i,2}$:1231

$$\eta_{HY} = \eta_I - \zeta_c\left(\frac{\psi_i}{2} + \frac{\phi_i^2}{2\psi_i}\right) \quad \text{(a)}$$

Impeller hydraulic efficiency: $(\eta_I \approx 0.90 - 095)$

Collector loss: $(\psi_i/2$ predominates) $(\zeta_c \approx 0.2 - 0.3)$

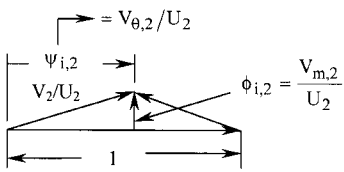

Practical experience (roughness ε constant for all sizes) yields the formula by W.K. Jekat:

$$\eta_{HY} \approx 1 - 0.8/\left[Q\,(\text{gpm})\right]^{0.25} \quad \text{(b)}$$

or $$\eta_{HY} \approx 1 - 0.071/\left[Q\,(\text{m}^3/\text{s})\right]^{0.25}$$

at all specific speeds.

However a deeper analysis treats losses L_{imp} as follows:

$$L_{imp} = k\frac{W_1^2}{2} + f\frac{\overline{W^2}}{2}\frac{\ell}{D_h} \quad \text{(c)}$$

where D_h = passage hydraulic diameter,
ℓ = passage length
f = pipe-type friction factor
k = incidence loss coefficient
$\overline{W^2}$ = the average square of the relative velocity within the passage along the rms or mean meridional streamline
W_1 = relative velocity just upstream of the impeller blades on the rms streamline

TABLE 3 Continued.

B) Mechanical Efficiency
From Eq. 9,

$$\eta_m = \frac{P_S - (P_{DF} + P_{B\&S})}{P_S} = 1 - \frac{P_{DF} + P_{B\&S}}{P_S} \qquad \text{(d)}$$

(Bearing & Seals)

$$P_{DF} = \frac{C_m}{2} \rho \Omega^3 r_2^5 \qquad \text{(e)}$$

Disk Friction

Where (for two sides of disk) $C_m \approx 0.085 \Big/ \left(\frac{\Omega r_{t,2}^2}{\nu} \right)^{0.2}$ (R_e) Typically $C_m = 0.004$ (at $R_e = 4.3 \times 10^6$) (f)

Shaft Power

$$P_S = \frac{\rho g \Delta H}{\eta_p} = \frac{\psi Q_S \rho \Omega^3 r_{t,2}^5}{\eta_p}$$

$$Q_S = \frac{Q}{\Omega r_{t,2}^5} = \Omega_s^2 \psi^{3/2} \Rightarrow P_S = \frac{\Omega_s^2 \psi^{5/2}}{\eta_p} \rho \Omega^3 r_{t,2}^5 \qquad \text{(g)}$$

Combining the usually smaller $P_{B\&S}$ with P_{DF}, Eq. (d) (with e, f and g) becomes

$$\eta_m = 1 - \frac{(C_m/2) \times \eta_p}{\Omega_s^2 \psi^{5/2}} \qquad \text{(h)}$$

C) Volumetric Efficiency
From Eq. 11,

$$\eta_v = \frac{Q}{Q + Q_L} \approx \frac{1}{1 + 5 \left[\frac{\frac{\delta}{r_R} \left(\frac{r_e}{r_2} \right)^2}{\Omega_s^2 \psi} \right]} \qquad \text{(j)}$$

The clearance ratio δ / r_R is typically 0.001 to 0.002

[Leakage back to impeller inlet across two rings (front and back) essentially doubles the leakage loss, changing the value 5 in Equation (j) to 10.]

inviscid solutions[42], each on a surface of revolution generated by one of the meridional streamlines of the hub-to-shroud 2D solution and producing results like that of Figure 17. From this, one computes the diffusion factors (Eqs. 57–59) and decides whether the diffusion losses are significant—in which case a redesign is in order, followed by a further Q3D evaluation. This type of iterative design approach for impeller blading has led some designers to combine Q3D analysis with an "inverse" design approach and a performance prediction scheme as discussed in this subsection. Here, in distinction to the more common "direct" choice of the conformal blade shape (Figure 19) between inlet and outlet as

described in paragraph (e) (vi) under "Designing the Impeller," one specifies the distribution of fluid dynamical quantities from inlet to outlet—such as UV_θ or W—and finally produces the corresponding blading[17,43]. In this sense, specifying W_g as described in the same paragraph (e) (vi) is an inverse design procedure.

Mechanical efficiency η_m, as stated earlier, is largely the result of impeller disk friction. If the drag of bearings and seals is added, as in Eq. (d) of Table 3, the moment coefficient C_m in the disk friction formula (e) can be increased over known disk friction values[44,45] to include these effects. (On the other hand, the drag power loss of shaft seals, though usually quite small, is generally directly proportional to speed. Such losses can therefore be significant in small pumps running at lower-than-normal speeds.) The C_m-expression given in Formula (f) reflects this adjustment and includes the drag on both sides of a smooth impeller for a typical clearance ratio $s/a = 0.05$, where a is the disc radius. This works well for most impellers: The drag at the ring fits roughly compensates for the fact that the impeller eye has been cut out of the disk, and so on. (There is very little influence on C_m of the gap width s between impeller shroud and casing wall, C_m being proportional to $(s/a)^{0.1}$ in general[44]. For very small s/a, C_m instead grows as s/a decreases; see Refs. 44 and 45 for formulas.)

The value of C_m can be even larger for semi- or fully-open impellers, if the neighboring fluid is rotating faster relative to the wall—as is the case with radial-bladed open impellers. The fluid between a shrouded impeller and adjacent wall, on the other hand, rotates at half speed[44]. (In cases where the impeller surface and adjacent wall are both rough, C_m is larger than just discussed[45].) Finally, notice in Eq. (h) that very low specific speed Ω_s produces a dramatically low value of η_m. This drives ψ to the larger values of Figure 12 at low Ω_s—also dictated by the W-deceleration considerations per Figure 22. Overall there is a benefit, despite possibly lower η_{HY} [Eq. (a)] due to the consequently greater ψ_i and collector loss.

Volumetric efficiency η_v applies to leakage across impeller shroud rings or "neck rings" and balancing drums. Eq. (j) in Table 3 is an approximation for the leakage across a typical ring of a closed-impeller pump, assuming orifice-type flow at a discharge coefficient of $\frac{1}{2}$, as reported by Stepanoff[4]. Referring to Figure 2, leakage Q_L occurs at $r = r_R$, (r_R being approximately 1.2 times r_e) under a pressure difference across the ring of about $\frac{2}{3}$ that of the pump stage. If the shroud is removed and the open blades are fitted closely to the adjacent wall, as with open impellers, the consequent leakage from one impeller passage to the next across the blade tips does not affect η_v, and Eq. (j) should be modified accordingly. Rather, the tip leakage causes a hydraulic efficiency loss as previously discussed. Finally, as with η_m, Eq. (j) indicates that low-Ω_s pumps have low η_v.

At flow rates Q other than Q_{BEP}, the analytical methods described previously for computing the hydraulic efficiency are utilized, together with computation of the inlet and outlet velocity diagrams, which yield the ideal head and power curves as illustrated in Figure 6. In this procedure, the slip velocity V_s (Figure 15) applies to the BEP and, at other flow rates, the exit relative flow angle $\beta_{f,2}$ can be assumed constant. This accords with the fact that V_s for the narrower active jet at low flow rates must be smaller. A blockage model for the thickening wakes and narrower active jets that develop as Q is decreased can be introduced to compute the one-dimensional velocity diagrams, but ignoring this at nonrecirculating flow rates appears not to be serious in determining the shapes of the head and power curves.

b) Shut-off and low flow. The foregoing analyses apply over that portion of the flow rate range that does not involve recirculation, as illustrated in Figure 6. The complexity of recirculation has not been readily handled analytically, and this has forced pump designers to estimate the low-flow end of the H-Q curve with the help of empirical correlations. Nevertheless, insightful fluid dynamical reasoning about the physics of the flow have led to useful expressions for the head developed and the power consumed at shut-off. Shut-off, then, in addition to the BEP, becomes the other anchor point of the head and power curves; and this—together with the shapes established for these curves at the higher flow rates—gives the analyst an idea of the intervening shapes.

Shut-off head $H_{s/o}$ can be viewed as the sum of two effects occurring at $Q = 0$, each being represented by a term in this equation:

$$H_{s/o} = \frac{k_{imp} \times (U_{t,2}^2 - U_{h,1}^2)}{2g} + \frac{k_{ex} \times U_2^2}{2g} \tag{65}$$

or

$$\psi_{s/o} = \frac{k_{imp} \times \left(\frac{r_{t,2}^2}{r_2^2} - \frac{r_{h,1}^2}{r_2^2} \right)}{2} - \frac{k_{ex}}{2} \tag{66}$$

where the first term is the centrifugal effect of essentially solid body rotation of the fluid confined within the impeller; and the second term is the pitot effect of the recirculating fluid from the impeller that impinges against the volute or diffuser throats which in turn are connected through stagnant fluid to the exit port of the pump. While the factors k_{imp} and k_{ex} associated with these effects vary with the hydraulic configuration, the values involved can be estimated as follows: $k_{\text{imp}} \approx 1$, as the radial equation of motion[3] would indicate for fluid rotating at Ωr everywhere within the blades, i.e., for $r_{h,1} < r < r_{t,2}$ (Fig. 8). Thus, as indicated by Eqs. 65 and 66, increasing the minimum radius of the blades at inlet $r_{h,1}$ tends to reduce the shut-off head. However, the presence or absence of fluid swirl in the region upstream of the impeller blades at shut-off has been found experimentally to affect the value of k_{imp} in surprising ways—sometimes increasing it above unity in such a way as to minimize the effect on shut-off head of any non-zero value of $r_{h,1}$. The value of k_{ex} depends on $(r_3 - r_2)/r_2$, or "Gap B" and other features of the impeller exit and collector geometry. It is usually in the range 0.2 ± 0.1, any change in the geometry that increases the shut-off power coefficient (see below) raising k_{ex} by driving more recirculating flow from the impeller against the volute or diffuser throats. Thus the shut-off head coefficient $\psi_{s/o}$ (Eq. 66) for typical radial-flow pumps generally exceeds $\frac{1}{2}$, the value of 0.585 being advanced by Stepanoff[4]. Estimates for $\psi_{s/o}$ are also indicated in Fig. 22b.

Shut-off power consumption $P_{s/o}$ includes disk, bearing, and seal drag power P_D and that which drives the recirculation P_{recirc}. The latter is generally dominant by far. From similarity arguments (Eq. 33), the shut-off power coefficient

$$\hat{P}_{s/o} = \frac{P_{s/o}}{\rho \Omega^3 r_2^5} \tag{67}$$

is a constant for a given pump geometry. Mockridge, in a discussion attached to an ASME paper by Stepanoff, reasoned that a wider impeller (larger b_2 at the same diameter D_2) would recirculate more fluid at shut-off and therefore have a higher value of this coefficient. His correlation is shown in Figure 23 and is probably the most significant quantitative result available for predicting the performance of centrifugal pumps at shut-off conditions[36].

c) Complete prediction via CFD. The uncertainties that have characterized the prediction of pump performance are now being overcome through advances in computational fluid dynamics. CFD entails three-dimensional solution of the flow fields within pumps via the Reynolds-averaged Navier-Stokes equations. Graf demonstrated the ability of a CFD computer code to calculate recirculation, the consequent prediction of the head curve for the impeller comparing favorably with experimental data[46]. The resulting distorted flows entering and leaving adjacent systems of impeller blades and stator vanes produce time-varying boundary conditions on each, the associated computational grids also moving relative to each other. This involves extensive, time-dependent computation. To provide solutions quickly on conventional, storage- and speed-limited workstations, some steady-flow codes treat these interfaces by circumferentially averaging the conditions at each point of the blade and vane leading and trailing edges as they appear in the meridional plane. Even with this simplification, pump analysts can now predict the entire performance curve of head within about two percent and the power curve with slightly less accuracy[47].

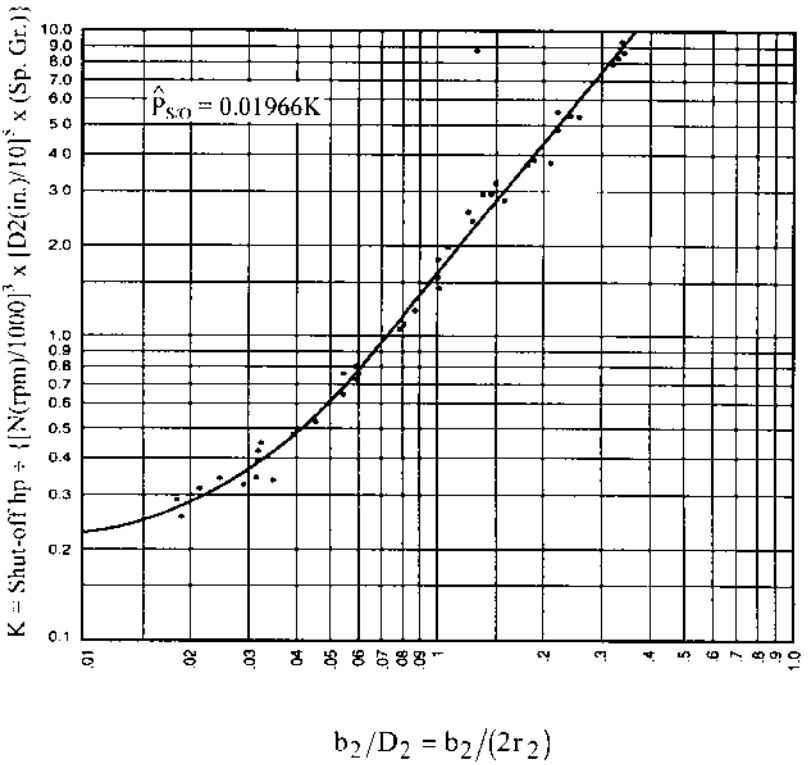

FIGURE 23 Shut-off power coefficient

The design task therefore resolves itself into an iteration between an efficient geometry-generating scheme and a rapid CFD flow and performance analysis of the geometry resulting from each iteration[48]. This is especially useful if a non-traditional geometry is involved, or if an efficient design is sought that will produce a desired performance curve shape. Nevertheless, many turbomachinery designers can make more rapid and valid judgments about their respective classes of machines through the time-honored iteration between a proprietary direct or inverse design and performance-prediction scheme and inviscid quasi-3D analysis [41,43]. They have developed reliable diffusion criteria (computed, for example, from Eqs. 59a and 59b) for interpreting the acceptability of the free-stream relative velocity distributions W_s and W_p on the blade surfaces (Figure 17) produced by the Q3D blade-to-blade solutions[43]. Because CFD codes solve the actual viscous flow field, the boundary condition on the blade surface is zero relative velocity. This can be at least partly overcome by displaying the CFD-distributions of pressures on the blade surfaces, the interpretation of which would require knowledge of the corresponding criteria for these pressures[46]. Also, the velocities at the edge of the boundary layer could be extracted from the CFD solution and displayed in familiar terms. A useful design approach for the present may therefore be to a) produce the final design by the more traditional methods and b) predict the performance curves via CFD[49].

Predicting Axial Thrust The prediction of pump performance is not truly complete without the corresponding prediction of the hydrodynamic axial and radial thrust that the impeller(s) can be expected to encounter. A comprehensive treatment of radial thrust appears in Section 2.3.1, and a review of axial thrust and thrust balancing devices is cov-

ered in Section 2.2.1. However, obscure flow phenomena can profoundly affect the radial distributions of pressure on the outside surfaces of a shrouded impeller that give rise to the net axial thrust. These phenomena become even more complex when discharge recirculation occurs and can cause adverse mechanical response in high-energy pumps, as will be explained further on. As a basis for tackling such problems, the fundamentals of axial thrust are presented in Table 4 for shrouded centrifugal impellers that have leaking fluid flowing in the gaps between the impeller shrouds and the adjacent casing walls. The positive direction of the thrust T is taken toward the suction or eye of the single-suction impeller shown. The incoming axial momentum $\rho Q V_{z,1}$ is generally quite small for radial impellers and has been omitted from the Table. It serves, however, to reduce T.

The centrifugal effect of the fluid spinning in the sidewall gaps causes a reduction in static pressure from the outer periphery (OD) of the impeller to the sealing ring, and this

TABLE 4 Leakage effects on axial thrusts

$$\text{Thrust} = (T_B - T_F)\, n_{stgs.} - T_{slv}$$

where $T = \int_{r_{min}}^{r_{max}} 2\pi r p\, dr$

where $p = p_2 - \int^2 \frac{\rho}{g} \frac{V_{\theta,gap}^2}{r} dr$

and p and $V_{\theta,gap}$ are determined as follows in the absence of vanes in the gap:

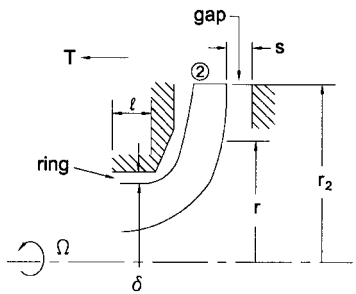

A) For zero leakage flow, fluid outside impeller rotates at half speed; i.e., at $\frac{\Omega r}{2}$; namely, $V_{\theta,gap} = \frac{\Omega r}{2}$; so that

$$p_o - p_i = \int_i^o \rho \frac{V_{\theta,gap}^2}{r} dr = \frac{\rho\Omega^2}{4} \int_i^o r\, dr = \rho \frac{\Omega^2 \left(r_o^2 - r_i^2\right)}{8}$$

or

$$p_o - p_i = \frac{\rho}{8} \Omega^2 r_o^2 \left[1 - \left(\frac{r_i}{r_o}\right)^2\right]$$

Note: This is 1/4 of what $(p_o - p_i)$ would be if $V_{\theta,gap} = \Omega r$ (full wheel speed - as on the front side of a semi-open impeller)

then, one gets $(p_o - p_i) = \frac{\rho}{2} \Omega^2 r_o^2 \left[1 - \left(\frac{r_i}{r_o}\right)^2\right]$

B) For non-zero leakage

1) Inflow: $V_{\theta,gap}$ averages to be > half speed

⇒ greater $(p_o - p_i)$ than at half speed (or zero leakage)

2) Outflow: $V_{\theta,gap}$ averages to be < half speed

⇒ nearly constant pressure from $(p_o - p_i)$

TABLE 4 Continued.

Specifically,

$$\text{where} \quad V_{\theta,\text{gap}} = \begin{cases} \Omega r_2 \times f_{\text{inflow}}\left(\dfrac{r}{r_2}, \Phi_{\text{lkg}}\right) \times f_{\text{width}} \\ \text{or} \\ \Omega r \times f_{\text{outflow}}\left(\Phi_{\text{lkg}}\right) \times f_{\text{width}} \end{cases}$$

$$\text{where} \quad \Phi_{\text{lkg}} = \frac{Q_{\text{leakage}}}{\Omega r_2^{\,3}} \Rightarrow \begin{cases} \text{Interaction of} \\ \text{leakage and} \\ \text{pressure at ring} \end{cases}$$

$$\text{where} \quad Q_{\text{leakage}} = f_L\left(\ell,\ \delta,\ \Omega,\ \nu,\ \Delta p_{\text{ring}}\right)$$

$$f_{\text{inflow}} = \left(0.5 - \frac{450}{\pi}\left|\Phi_{\text{lkg}}\right|\right)\frac{r}{r_2} + \frac{450}{\pi}\left|\Phi_{\text{lkg}}\right|$$

$$f_{\text{outflow}} = 0.5 - 100\left|\Phi_{\text{lkg}}\right|$$

$$f_{\text{width}} = \frac{\sqrt{A^2 + A} - A}{0.5}$$

$$\text{where} \quad A = 1/\left[5\, s/r_2\right]$$

is quantified in the expressions given for the swirl velocity component V_θ. These expressions are curve fits to experimental data for the leakage flowing radially inward on either or both sides of the impeller[50] and for outflowing leakage as occurs on the back side (away from the "front" or suction side) of multistage pump impellers due to the higher pressure arising from the diffusing system downstream of each impeller[51]. In the absence of leakage, the fluid in the sidewall gap rotates at about half the local impeller wheel speed; that is, $V_\theta = \Omega r/2$, and this half speed is typical of the gap flow near the impeller OD, even in the presence of leakage. The greater the inflow leakage, the lower the pressure becomes at the entrance to the ring clearance. The major effect is that of swirl or the tangential component of velocity V_θ, which varies inversely with radius unless casing wall drag interferes. More leakage flow is less influenced by this drag and so experiences a greater centrifugal effect. This in turn means more pressure drop from OD to ring. (The leakage rate, of course, is affected, the solutions for both leakage and pressure distribution being linked and usually requiring iteration.) The opposite effect happens for outflow on the back side of multistage pump impellers. Here the fluid enters the sidewall gap at a small radius (see Section 2.2.1) and so with negligible swirl. It flows outward without picking up much swirl, especially if there is substantial radial outflow leakage, which means the centrifugal effect is small, yielding a nearly constant pressure versus radius. The overall result is more net thrust than might be expected from a cursory look at the pressure-loaded surfaces.

If wear ring clearances increase during the life of the pump, the net thrust of multistage pump impellers increases. Likewise, unequal ring wear leads to uncertain changes in the thrust of a "balanced" single- or double-suction impeller with inflow to wear rings on both sides. Similarly, these theories can be applied to balancing drums and other such devices described in Section 2.2.1.

Integration of the pressure equation in Table 4 becomes a chore unless the whole theory is computerized. A quick estimate of the thrust is possible, however, if the distributions of pressure in the separable domains of the surfaces are assumed to be linear; in that case,

TABLE 5 Approximate axial thrust calculation

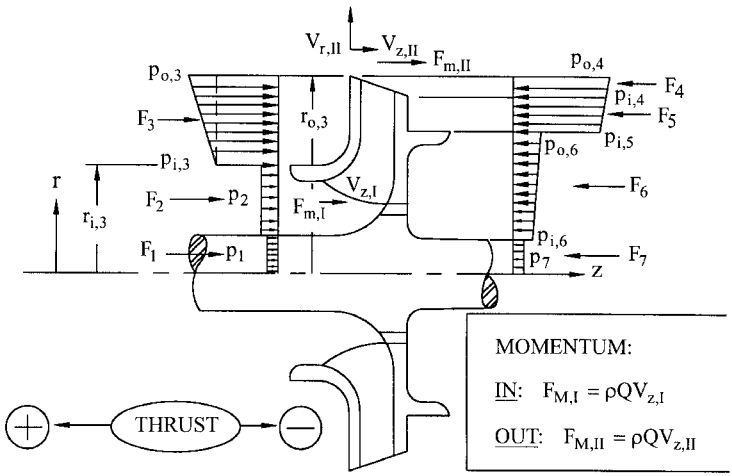

$$\underline{\text{THRUST}} = F_7 + F_6 + F_5 + F_4 - F_3 - F_2 - F_1 - F_{m,I} + F_{m,II}$$

$$\underline{\text{For Const. - p Forces}}: \quad F_j = p_j \times 2\pi \left(r_{j,o}^2 - r_{j,i}^2\right) \qquad j = 1,\ldots,7$$

i = inner; o = outer

$$\underline{\text{For Linear p(r) Forces}}: \quad F_j = F_{j,\text{const.}} + F_{j,\text{var}}$$

$$\text{where} \quad F_{j,\text{var}} = \tfrac{1}{3}\pi r_{j,o}^2 \left[2 - \frac{r_{j,i}}{r_{j,o}} - \left(\frac{r_{j,i}}{r_{j,o}}\right)^2\right] \times \left(p_{j,o} - p_{j,i}\right)$$

Example:

$$F_3 = p_{i,3} \times 2\pi\left(r_{o,3}^2 - r_{i,3}^2\right) + \tfrac{1}{3}\pi r_{3,o}^2 \left[2 - \frac{r_{3,i}}{r_{3,o}} - \left(\frac{r_{3,i}}{r_{3,o}}\right)^2\right] \times \left(p_{o,3} - p_{i,3}\right)$$

the integration is simple and yields the closed-form results of Table 5. This table also indicates how to account for each element of the thrust, including the axial momentum terms, which become significant for higher-specific-speed mixed-flow impellers. In all cases, in order to proceed with the calculation, the static pressure at the impeller OD must be known, as it is from the boundary condition imposed at the OD that the rest of the pressure distribution emerges. Even for substantial leakage, the pressure drop of the fluid entering the sidewall gaps from the impeller exit is small or negligible; therefore, the impeller pressure essentially applies in the gap (at the OD) as well. The foregoing methods of predicting pump head also yield the impeller OD pressure, which is usually between 75 and 80% of the stage pressure rise above inlet.

Thrust computations can therefore be coupled with the head-curve prediction scheme being employed for the pump, thereby yielding predicted thrust curves together with the predictions of hydraulic performance.

Ensuring Stable Performance The ability for a pump to run smoothly with minimal pressure-rise and flow-rate excursions is dependent on the shape of the pump head-flow performance curve and the characteristics of the system in which it operates. There are two types of pump-system instability; namely, a) static instability, which can be ascertained by studying the pump and system head curves, and b) dynamic instability, which requires more detailed knowledge of the system[52]. (In addition to these system-related instabilities, there is the unsteady behavior of the separated and recirculating flows that occur when a pump operates a flow rate substantially below the BEP. Called hydraulic instability, this becomes important in higher-energy applications and is therefore discussed later.)

a) Static stability and instability. Figure 24 illustrates two pumping systems; namely, a) a piping system in which the flow is turbulent and largely independent of Reynolds number; so, the head drop ΔH through it is proportional to Q^2, and b) two reservoirs with a constant difference ΔH between the two liquid surfaces and comparatively negligible head loss in the pipes connecting them. In each case, the pump is designed to produce head ΔH, as required to deliver the desired flow rate Q. The influence of the pump head curve shape is immediately appreciated in Case (b): the curve "droops" as Q is reduced to shut-off, thereby producing two vastly different flow rates at the same head. In fact, however, the pump will not operate at the lower-Q intersection point of the two curves. The pump shut-off head is less than ΔH, so it will produce no positive flow rate. Instead, as discussed in Section 2.3.1, fluid will flow backwards through the pump. Further, if circumstances could allow operation at this lower-Q point, even a vanishingly small increase of Q would cause a further, divergent increase because the head of the pump exceeds the ΔH of the system. Likewise, a small decrease leads to even lesser Q because the system ΔH exceeds that of the pump. This is called "static instability." Conversely, the higher-Q point of Figure 24b is "statically stable," small departures in Q being suppressed by algebraically opposite signs of the difference between the system and pump heads. Both intersection points of Figure 24a are seen by this type of analysis to be statically stable. If the operator increases the frictional resistance by closing up a valve in the piping system, the operating point simply moves to the left on the curve and remains stable. Thus, it is concluded that if the slope of the pump H-versus-Q curve is *less* than that of the system, operation will be *statically stable*—and vice versa.

Most pumping systems are combinations of the "pure friction" type of Figure 24a and the "purely elevation" type of Figure 24b. In this case of static stability, the drooping pump head curve presents no problem. Theoretically, it is possible to have a pump head curve with a kink that could have a more positive slope than that of a system curve, which might intersect it at such a kink. The high-Ω_s curve of Figure 22b depicts a kink or dip, which is due to stalled flow within a mixed- or axial-flow impeller that is not sufficiently confined by the impeller to be maintained in solid body rotation. (It is the centrifugal effect of such rotation that maintains the pressure rise in radial-flow impellers despite the stalling.) That particular pump, if applied to a system that never intersects the pump head curve at the kink, would never experience static instability. On the other hand, the designer may want to take on the challenge of designing a machine without such a kink. The previously mentioned design procedure utilizing CFD in both the impeller and the diffuser to check whether the kink is gone would be a way of tackling this problem[53].

In-depth discussion of the variety of systems that can be encountered, including multiple systems and parallel operation of multiple pumps, can be found in Sections 2.3.1, 8.1, and 8.2. Purely from a static stability standpoint, most of these situations demand a substantially negative slope of the head curve throughout the range of flow rate Q—or what is commonly specified as a pump with head "continuously rising to shut-off." (This "rise in head" versus a drop in Q should not be confused with the pump developed head H, which is also properly termed the "head rise" ΔH, produced by the pump at a given value of Q.)

b) Dynamic instability. If the system has appreciable capacitance, operation may not be stable if the slope of the pump head curve is positive or even zero[54]. This is true even though the slope of the pump head curve is less than that of the system head curve as required above for static stability—as with the lower-Q intersection point of Figure 24a. Dynamic instability can be manifested as pump surge, a phenomenon wherein the flow

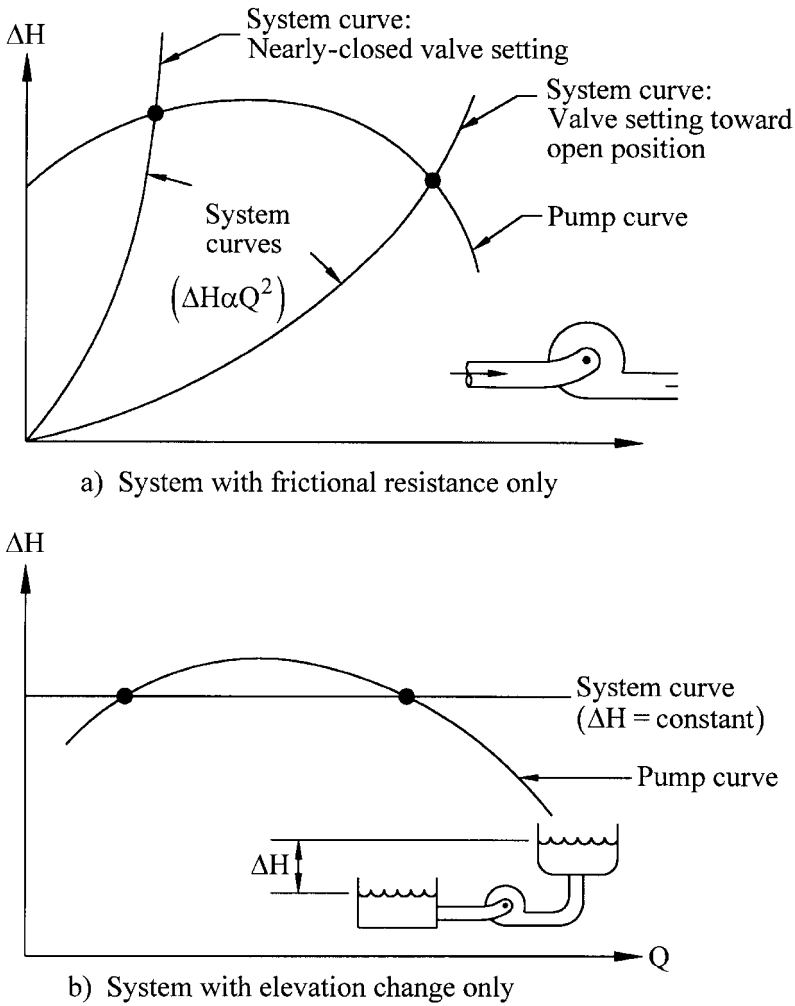

FIGURE 24A and B Pump-system stability

rate oscillates and can even be alternately positive and negative through the pump[54]. This is characteristic of "soft" systems that contain vessels with free surfaces and, therefore, appreciable capacitance. Two-phase flow increases the capacitance of a system and can cause dynamic instability. For example, fluctuating vapor volume within the propellant pump inducers can contribute to the dynamic instability of a rocket propulsion system[55].

On the other hand, a "hard" piping system with no capacitance is theoretically capable of accommodating a pump that has a flat or drooping head curve and that operates on that flat or drooping section of the curve. Low-specific-speed pumps can have drooping curves (Figure 22b), especially if designed with a high head coefficient ψ at the BEP. Figures 5 and 7 of Section 2.3.1 depict flat and drooping curves of low-Ω_s radial-bladed pumps, a type that is widely used in low-cost, small sizes. If properly applied, such machines will operate with stability. On the other hand, a conservative approach that guarantees both static

and dynamic stability for the widest range of applications is to design all pumps without flat spots or droops in the head curves.

DESIGN EXAMPLE

To illustrate the application of the preceding design information, the basic hydraulic design requirements are presented in Table 6 for a single-stage centrifugal water pump with a volute collector. The chosen conditions compute to a universal specific speed Ω_s of 1 (N_s = 2733, and n_q = 52.9 from Eqs. 38a and 38b). The pump is to be designed for a suction specific speed Ω_{ss} of 4.5 ($N_{ss} \equiv S$ = 12,300 by Eqs. 41 and 42), therefore, a "performance-*NPSH*" (see *NPSH* discussion in Section 2.3.1) or $NPSH_{3\%}$ of 14 ft (4.27 m). As such, this pump is readily applicable to taking water from an atmospheric reservoir with some suction lift. Although acceptable for 1780 rpm specified for this pump, this suction-specific speed Ω_{ss} of 4.5 is regarded as high for pumps with more head (energy level) than this one (see the energy-level discussion later).

Impeller Design

SUCTION NOZZLE Beginning upstream, an ideal, axial-flow approach passage is assumed —this is known as an "end-suction" configuration. The suction-approach passage or suction branch (not shown) is simply a conical nozzle that increases the velocity of the fluid from the suction port to the impeller eye by about 50 percent in an axial distance of about half the diameter of the eye. This helps to ensure the existence of uniform flow at the eye. Too short a nozzle would mean excessive local meridional (axial in this geometry) velocity at the impeller shroud and possible separation.

IMPELLER INLET Beginning with Ω_{ss} of 4.5, computations for this example are carried out in Table 7 for the impeller eye geometry. The choice of the $NPSH_{3\%}$ correlation of Table 1 is used, with k_1 = 1.69 and k_2 = 0.102. The local maximum velocity at the eye $V_{1,sh}$ ($=V_{m,1,sh}$) is assumed to be 25% greater than the one-dimensional average $V_e = Q/A_e$. This is smaller than the bladeless result of Figure 14, but is typical of this end-suction configuration,

TABLE 6 Given conditions for design example (single stage, end-suction volume pump)

Speed = 1780 RPM

Flow Rate = 2500 gpm (0.1577 m^3/s)

Head = 104 ft. (31.7 m) Fluid: Water $\begin{cases} \text{sp. gr.} = 1 \\ \nu = 1 \text{ cs.} \end{cases}$

Specific Speed $\Omega_s = 1\,; N_s = \dfrac{1780\sqrt{2500}}{(104)^{3/4}} = 2733;\ n_q = \dfrac{1780\sqrt{0.1577}}{(31.7)^{3/4}} = 52.9$

Suction Specific Speed $\Omega_{ss} = 4.5$ (S = 12,300)

$$\text{NPSH} = \left\{\frac{1780}{12{,}300}\right\}^{4/3} (2500)^{2/3} = 14 \text{ ft. } (4.27 \text{ m})$$

TABLE 7 Impeller inlet (design example)

$$\Omega_{ss} = 4.5 = \frac{\sqrt{\pi \phi_e \left(1 - \frac{r_s^2}{r_e^2}\right)}}{(\tau/2)^{3/4}} \qquad \text{(from Eq. 50)}$$

For $\tau = (1.69 + 0.102)\,\phi_e^{\,2} + 0.102$

$\phi_e = 0.29$ = eye flow coefficient

Eye dia/2 = eye radius:

$$r_e = \sqrt[3]{\frac{Q}{\Omega \pi \phi_e \left(1 - \frac{r_s^2}{r_e^2}\right)}} = \sqrt[3]{\frac{2500\text{gpm}/449\ \frac{\text{gpm}}{\text{ft}^3/\text{sec}}}{\frac{\pi}{30} \times 1780 \times \frac{\pi}{\text{sec}} \times 0.29}} \qquad \text{(from Eq. 49)}$$

[$r_s = 0$ (no shaft in eye)]

$r_e = 0.3201$ ft. (0.0976 m)

$r_e = 3.84$ in. (97.6 mm)

$V_e = 17.3$ (5.3) $= \phi_e U_e$

$W = 62.1$ (18.9)

$16.2° = \beta_{f,1}$

$U_e = 59.6$ ft/sec. (18.2 m/s) $= \Omega r_e$

(See Fig. 25): $R_{sh} = \frac{r_e - r_s}{2} = 1.92$ in. (48.8 mm)

Other dimensional data shown on Fig. 25.

including the effect of the blading. Moreover, the value of k_1 should be more than adequate for this value of $V_{1,sh}$.

The Ω_{ss} and τ-ϕ_e relationships yield the eye flow coefficient ϕ_e, which in turn sizes the eye. $\phi_e = 0.29$ implies a τ-value of 0.253, which is typical. However, lower ϕ_e- and τ-values are common, especially for the case of a shaft through the eye, because this tends to maintain the level of Ω_{ss} in the face of the r_s-effect in Eq. 50. The nominal velocity diagram at the eye—substantially the shroud-end or tip of the blade leading edge—shows V_e rather than $V_{1,sh}$ for the meridional component of velocity and so is not the actual velocity diagram at that location. Rather, this triangle serves to identify the geometry through the basic ratio $\phi_e = V_e/U_e$—without having to deal with the uncertain choice of $V_{1,sh}/V_e$. Moreover, ϕ_e is the tangent of the tip relative flow angle β_{f1} as it would be for a uniform axial velocity profile in the eye.

With the eye radius r_e established, the local shroud radius of curvature R_{sh} follows from the guidelines associated with Figure 13. The geometry established so far is illustrated in Figure 25. Before the full picture shown there can be established, the outlet must be sized.

IMPELLER OUTLET The computations in Table 8 for the impeller exit begin with the choice of the typical value of $22\frac{1}{2}$ degrees for the outlet blade angle $\beta_{b,2}$. This enables the head coefficient ψ to be chosen under the guidance of the upper curve in Figure 12. The value 0.385 is selected, and this yields the impeller diameter of 12 in. (304.8 mm). The other curve in Figure 12 is for outlet flow coefficient $\phi_{i,2}$, which conveniently equals 0.1715 for

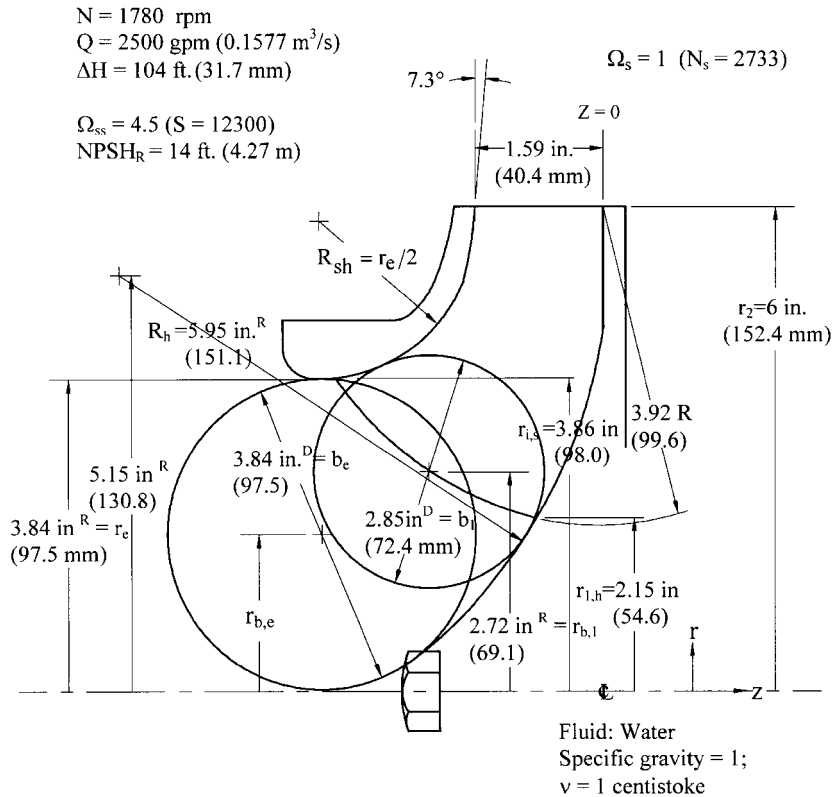

FIGURE 25 Impeller hub and shroud profiles (design example)

$\Omega_s = 1$. This leads to the exit width b_2 after adding in the leakage and the blockage of blades and boundary layers per the computations of Tables 9 and 10.

However, Anderson[6] points out that what matters for centrifugal pump performance is neither the blade angle nor the exit width individually, but the impeller outlet relative area $2\pi r_2 b_2 \sin \beta_{b,2}$. Choosing a higher blade angle is possible if b_2 is correspondingly reduced (and $\phi_{i,2}$ increased) so as to maintain this area and therefore the relative velocity W. Figure 15 shows that $V_{\theta,2}$ is thereby essentially unchanged; this in turn preserves the impeller head.

EFFICIENCIES Anderson's overall pump efficiency correlation (Figure 10 and Eq. 44) and the component efficiency expressions of Table 3 lead to the results of Table 9. These give an indication of the relative magnitudes of the losses and are as follows:

Overall efficiency $\eta_p = 0.8550$

Mechanical efficiency $\eta_m = 0.9814$

Volumetric efficiency $\eta_v = 0.9833$ (leakage across front and back rings)

Hydraulic efficiency $\eta_{HY} = 0.8860$

η_{HY} is at this point simply deduced from the others, beginning with Anderson's correlation. Although it is confirmed by Jekat's correlation in the table, it can be found in a

TABLE 8 Impeller outlet (design example)

From Figure 12

$$\beta_{b,2} = 22\tfrac{1}{2}^\circ \rightarrow \phi_2 = \frac{V_{m,2}}{U_2} = 0.1715 \quad (= \phi_i)$$

$$\rightarrow \psi = \frac{g_0 \Delta H}{U_2^2} = 0.385$$

$$(U_2 = \Omega r_2) = \frac{\pi}{30} \times 1780 \times \frac{6}{12} = 93.2 \ \frac{\text{ft.}}{\text{sec.}} \ (28.4 \text{ m/s})$$

$$r_2 = \sqrt{\frac{g \Delta H}{\Omega^2 \psi}} = 12 \sqrt{\frac{32.174 \times 104}{\frac{\pi^2}{30^2} \times (1780)^2 \times 0.385}}$$

= 6 in. (152.4 mm) [12 in. (304.8 mm) dia.]

Width: $b_2 : A_2' = \pi D_2 b_2'$

$b_2 = b_2' + 2\delta_o^* +$ Leakage Effect

Solve after obtaining volumetric efficiency and getting approximate passage length (to compute δ_o^*)

detailed computation of the hydraulic losses via one-dimensional methods. This will be carried out further on to obtain the performance characteristic curves. Meanwhile, this initial computation enables the determination of $V_{\theta,2}$ at the end of Table 9, which, along with $V_{m,2}$ from Table 8, is a major element of the outlet velocity diagram of Figure 26.

BLOCKAGE AND WIDTH AT IMPELLER EXIT With the leakage and exit blade angle information, Table 10 contains the computations of the blockage and the exit width b_2. This entails the choice of the number of blades, the blade thickness t (2% of the impeller diameter and typically assumed to exist at the exit and elsewhere on the blades except near the leading edges where typically half that value is chosen), and the approximate blade length ℓ (assuming the mean-streamline blade angle to be constant at $22\frac{1}{2}$ deg). The boundary layer blockage is computed from the following approximations:

- Adverse pressure gradients on the blades lead to a boundary layer displacement thickness δ^* of twice the zero-pressure gradient value δ_0^* on each blade surface.
- Secondary flows scrub the boundary layers from the hub and shroud surfaces; so, δ^* is assumed to be equal to δ_0^* on those surfaces.
- $\delta_0^* = 0.0462\ \ell^{0.8}\nu^{0.2}/W^{0.2}$ for flat-plate, turbulent flow[56], and is approximated in this example for low viscosity by a linear growth with length along the blade.

The resulting thickness of the boundary blockage is 0.0732 in (1.86 mm) on the blades, which themselves have a thickness of 0.24 in (6.1 mm). Because these thicknesses are inclined at the $22\frac{1}{2}$-deg outlet angle, the actual circumferential blockage is $(1 - \varepsilon_{2,b})$ = (1 − 0.870) or 13 percent of $2\pi r_2$. In particular, (0.24 + 0.0732)/sin ($22\frac{1}{2}$ deg) = 0.82 in or (6.1

TABLE 9 Component efficiencies (design example)

Efficiency: $\eta_p = 0.94 - 0.08955\left(\frac{2500}{1780}\right)^{-0.21333} - 0.29\left[\log_{10}\left(\frac{2286}{2733}\right)\right]^2 = 0.8550$
(Eq. 44)

Mech. Eff'y: $\eta_m = 1 - \frac{0.002 \times 0.8550}{1^2 \times (0.385)^{5/2}} = 0.9814 \quad [P_D = 1.43 \text{ hp.}(1.07 \text{ kW})]$
(from Table 3)

Volumetric Efficiency: $\eta_v = \frac{1}{1 + 5\,\frac{0.0016 \times (3.84/6)^2}{1^2 \times 0.385} \times 2} = 0.9833$
(from Table 3)

Hydraulic Efficiency: $\eta_{HY} = \frac{\eta_p}{\eta_v \eta_m} = \frac{0.8550}{0.9650} = 0.886$ vs.
(Eq. 8)

(Jekat's formula in Table 3):

$$\eta_{HY} \approx 1 - \frac{0.8}{(2500)^{0.25}} = 0.887$$

$$\Rightarrow \quad V_{\theta,2} = \frac{32.174 \times 104}{93.2 \times 0.886} = 40.5 \text{ ft/sec.}$$

$$\Rightarrow \quad \psi_i = \frac{40.5}{93.2} = 0.435$$

+ 1.86)/sin($22\frac{1}{2}$ deg) = 20.8 mm per blade, which for all six blades is 0.130 times the circumference of 37.7 in (958 mm). The width b_2 is computed to maintain $V_{m,2}$ at the chosen value of $0.1715 \times U_2$, while accommodating this blockage and that of the sidewall boundary layers. Altogether, it can be computed from these data that 85 percent of the meridional exit area $2\pi r_2 b_2$ is estimated to remain open for the one-dimensional flow of $(Q + Q_L)$ at velocity $V_{m,2}$, the boundary layers causing $\frac{1}{3}$ of the blockage. This is quite typical. An openness of 90 percent is possible for larger impellers.

HUB-SHROUD PROFILES It is now possible, through the guidelines outlined in the discussion of Figure 13, to finish plotting the hub and shroud profiles in Figure 25, which are also seen in Figure 26c. At this point, the envelope of the leading edges of the blades is approximated by a circular arc—later modified somewhat in the construction of the blades. The arithmetic average radius of the meridional passage at the leading edges is found with the circle of diameter 2.85 in (72.4 mm) to be 2.72 in (69.1 mm). The resulting line passing through the center of the circle is normal to both hub and shroud and is approximated by the dashed straight-line leading-edge quasi-normal shown in the Figure 26c.

INLET VELOCITY DIAGRAMS The rms radial point on this quasi-normal line of Figure 26c crosses the leading edges of the blades at $r_{1,\text{mean}} \equiv r_{1,\text{rms}} = 2.91$ in (73.9 mm) and is slightly larger than the arithmetic average radius of 2.72 in (69.1 mm). It is this latter radius that

TABLE 10 Impeller blade blockage and width at exit (design example)

Blade no. n_b: Assume = 6

Check Solidity :

Blade thickness $t = 0.04\ r_2 = 0.24$ in. (6.1 mm)

$$\ell = \Delta m \Big/ \sqrt{\sin\beta} \approx \frac{3.5 \text{ in.}}{\sin 22\tfrac{1}{2}^\circ} = 9.15 \text{ in.}(232.4 \text{ mm}) \quad \text{(Eq. 56)}$$

$$\sigma = \frac{6 \times 9.15}{\pi \times 12} = 1.46 \rightarrow \text{OK} \quad \text{(Eq. 53)}$$

$$\varepsilon_{2,b} \text{ (blades only)} = 1 - \frac{6\,(0.0732 + 0.240)}{\pi \times 12 \times \sin 22\tfrac{1}{2}^\circ} = 0.870$$

$$\delta_o^* \approx 0.002 \times \ell \approx 0.002 \times 9.15 \text{ in.}(232.4 \text{ mm})$$

$2\delta \approx 4\,\delta_o^* \approx 0.0732$ in.(1.86 mm) on blades

$2\delta \approx 2\,\delta_o^* \approx 0.0366$ in.(0.93 mm) on hub and shroud

gpm & ft/sec to inches

η_v

$$b_2 = 0.0366 + \frac{2500 \times 0.3208 / 0.9840}{\underbrace{0.1715 \times 93.2}_{V_{m,2}} \times \underbrace{0.870}_{\varepsilon_{2,b}} \times \pi \times 2 \times 6} = 1.59 \text{ in.}(40.4 \text{ mm})$$

$$\left(\text{Since } b_2 = 2\delta_o^* + \frac{Q + Q_L}{V_{m,2} \times \varepsilon_{2,b} \times \pi \times 2 \times r_2}\right)$$

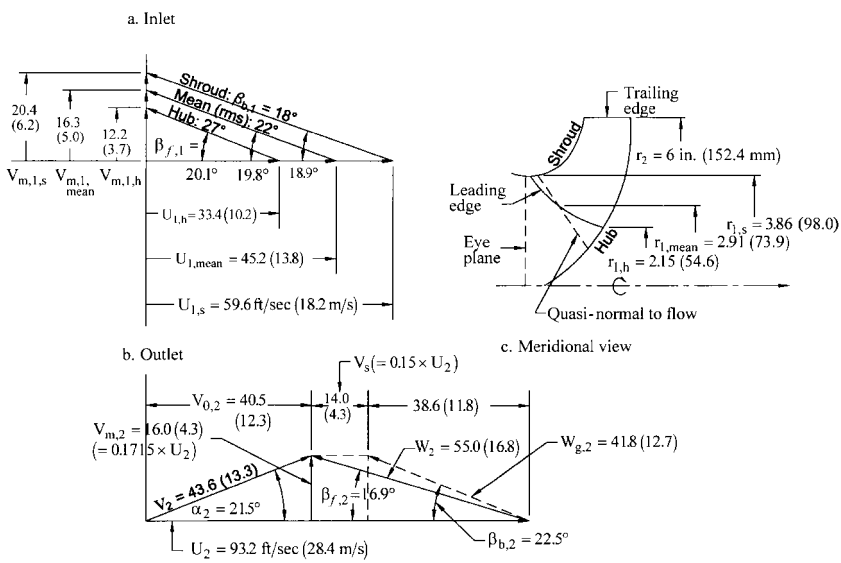

FIGURE 26A through C Impeller velocity diagrams for design example: a) inlet; b) outlet; c) meridional view

must be used in computing the one-dimensional meridional velocity. After obtained, it is applicable to the rms location (the location of the "mean" or "rms" inlet velocity diagram). This diagram is one of three triangles shown for the inlet in Figure 26a, the other two being located at the hub and shroud locations of the blade leading edges. Notice that $V_{m,1}$ for the rms triangle is 16.3 ft/sec (5.0 m/s), which is slightly less than the eye velocity V_e of 17.3 (5.3). Allowing for blade blockage, this would bring the blocked meridional velocity V_m within the blading closer to V_e, the objective being to keep V_m constant in the inlet region and turn into the radial direction. The other triangles correspond to the radial locations of the blade at hub and shroud, as illustrated in Figures 26c and 27, and assume that $V_{m,1,sh}$ = 1.25 times $V_{m,1}$, and $V_{m,1,h}$ = 0.75 $V_{m,1}$. A full Q3D solution would determine these velocities more accurately; however, the design usually proceeds in this way—largely because the hub blade angle is usually a good deal larger than hub flow angle. Efforts to match the hub flow angle more closely entail special blading that is beneficial for high-energy pumps but has little effect otherwise. The blade angle at the shroud is slightly lower than the flow angle (by about 1 deg). This slightly negative incidence is actually ideal for efficient flow and minimum cavitation. The largest values of U and W exist at the shroud, as can be seen for the shroud inlet triangle, making it important to have the best match at that point. Two deg positive incidence is quite common at the mean or rms radial location and allows for blockage by the blades that does not increase the relative velocity W as the fluid enters the impeller.

OUTLET VELOCITY DIAGRAM The outlet velocity components having been found in Tables 8 and 9, the slip velocity V_s must still be found in order to obtain the complete outlet velocity diagram shown in Figure 26b. This slip is computed by Pfleiderer's method (Table 2), which utilizes the $r(m)$ shape of the mean meridional streamline illustrated in Figure 27, V_s emerging as 15% of U_2. The "a" factor for influence of the collector geometry was taken in the middle of the range for volutes at 0.75; (see Table 2). Wiesner's Eq. 52 yields 17.65%. This would mean 6% less $V_{\theta,2}$ and head. However, this discrepancy is not unexpected, and in view of the earlier discussions on slip, the Pfleiderer result is chosen as more realistic.

Nevertheless, uncertainty in the slip is the Achilles heel of the one-dimensional analysis method. For this reason, most analysts "calibrate" their codes by deducing the slip from test results and applying it to impellers of similar geometry. For Pfleiderer's method, this would be done by calibrating the "a" factor. CFD solutions now appear to be the best approach to overcoming this difficulty.

As has been emphasized heretofore, this outlet velocity diagram contains the basic information about the performance and design of the pump. It supplies the boundary conditions for the volute design, but first the impeller blading that must produce it will be established and evaluated.

IMPELLER BLADING As indicated in Figure 26, the blade angles at both inlet and outlet have been chosen at hub, mean, and shroud (with the same $22\frac{1}{2}$ deg all across the trailing edge being assumed, although some would specify a little variation). Fitting a reasonable blade shape between these end conditions can be done in the conformal plane (illustrated in Figure 19). These shapes, when transformed as described earlier, yield the hub, mean, and shroud blade shapes identified in the polar view of Figure 28. In actuality, the inverse "point-by-point" method was used, specifying W_g as indicated in Figure 29 and, at each of the 21 stations along the mean line of Figure 27, developing the velocity diagrams in the manner employed to arrive at Figure 26b; obtaining β_b at each station; and developing the *mean-streamline blade shape* of the polar view with Eq. 60. Involved in this procedure—which was computerized—was the calculation at each station of the blockage and of the local slip velocity, the latter being estimated as a fraction of the discharge slip velocity V_s that increases rapidly to unity as the exit is approached.

Note that the meridional area is needed at each station in order to compute V_m. As indicated in Figure 27, this is approximated here as the area of the frustum of a cone defined by the dashed lines or "quasi-normals," which are as nearly perpendicular to both hub and shroud as possible. Except for some machines with meridionally curved passages and a large passage width-to-length ratio causing the true normals to be strongly curved, the quasi-normal approach works well.

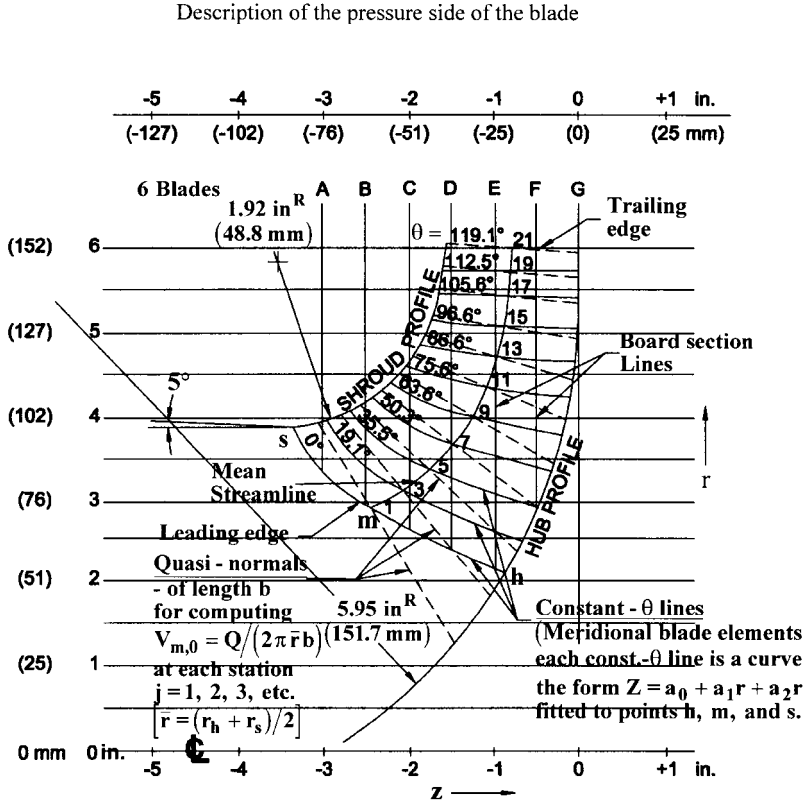

FIGURE 27 Impeller blading–meridional view (design example)

To establish the *blade shapes along the hub and shroud*, the corresponding "grid lines" of Figure 19 were found from polynomials satisfying the end conditions of blade angle and location, the y-position of the inlet end of the grid line being iterated until the desired blade wrap was obtained. In this way, different wrap angles $\Delta\theta$ ($= \theta_2 - \theta_1$) can be imposed, but a tolerable resulting blade shape requires that these $\Delta\theta$s be not much different from the $\Delta\theta$ ($= 119.1$ deg) obtained on the mean line from the method just described. In this example, it was possible to maintain $\Delta\theta$ the same on all three construction lines. Alternatively and perhaps more consistently, the inverse approach could be applied at hub and shroud as well as on the mean line.

Regardless of which procedure is used to generate the hub, mean and shroud blade shapes—the conformal transformation method, the point-by-point method, or some combination—the *shape of the blade everywhere else* still needs to be established. To do this, the shapes of the constant-θ lines in Figure 27—called "blade elements"—must be specified. This can be done mathematically as indicated on the figure or by eye (the latter approach is widely used). Note that each constant-θ line actually lies in a different meridional plane. Thus, Figure 27 depicts a superposition of all 21 meridional planes, each containing an intersection of the blade surface and appropriately identified as having the θ-value noted on the figure.

DIFFUSION ASSESSMENT Figure 29 is a presentation of the free-stream relative velocity distributions at the blade surfaces and halfway between. The rapid approximate method of

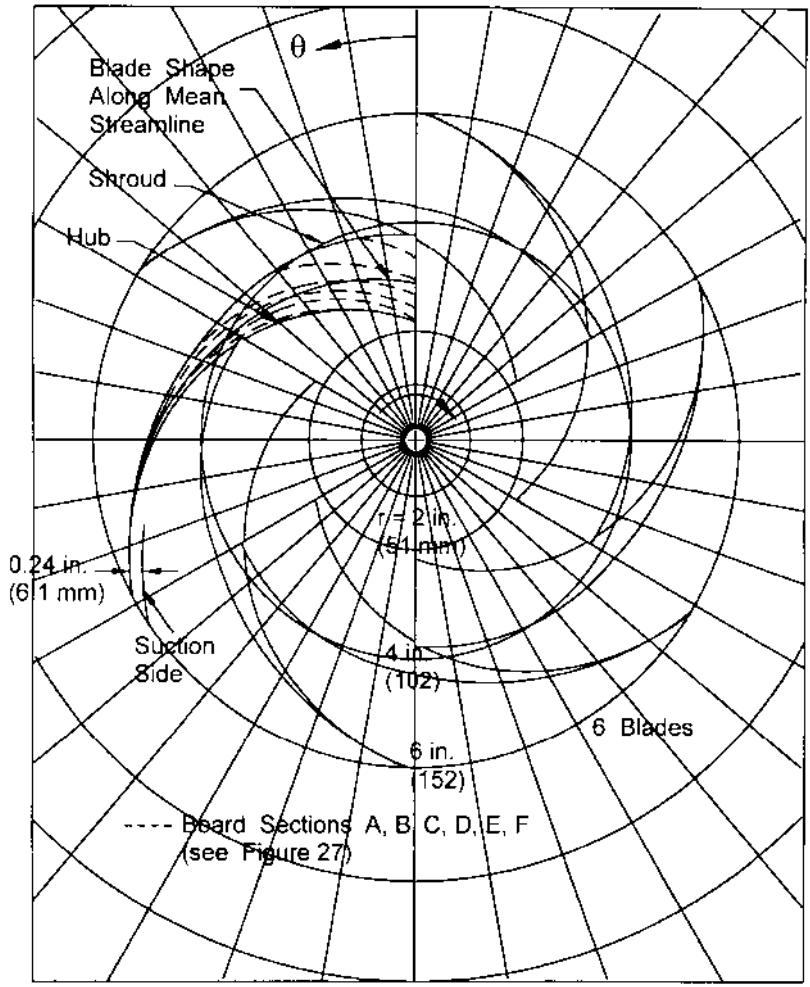

FIGURE 28 Impeller blading—polar view, showing pressure sides of the blades (design example)

Stanitz (Eq. 54) is utilized to obtain the surface W's, the mean values of W on the mean (rms) streamline coming from the local velocity diagrams developed at each station[22]. The mean W's at hub and shroud are found at the ends of the respective constant-θ lines under the assumption that the ideal head or UV_θ-product is constant along each of these lines from hub to shroud. This is usually a fair approximation; however, a Q3D analysis (Figure 14) would yield a closer estimate of these mean W-distributions[16,41]. Nevertheless, the diffusion factors computed from the plotted surface velocities by means of Eqs. 59 are shown on the figure—these values are well below the 0.6 limit. This would indicate that the resulting solidity of 1.48 (originally estimated at 1.46 in Table 10) is adequate, and that the correct number of blades was chosen.

Notice also on Figure 29 that the exit value of W is significantly larger than W_g, which is consistent with the outlet velocity diagram of Figure 26b. Further, a slight jump in the mean W at the inlet is indicated; however, as the higher value of W is not sustained, it is

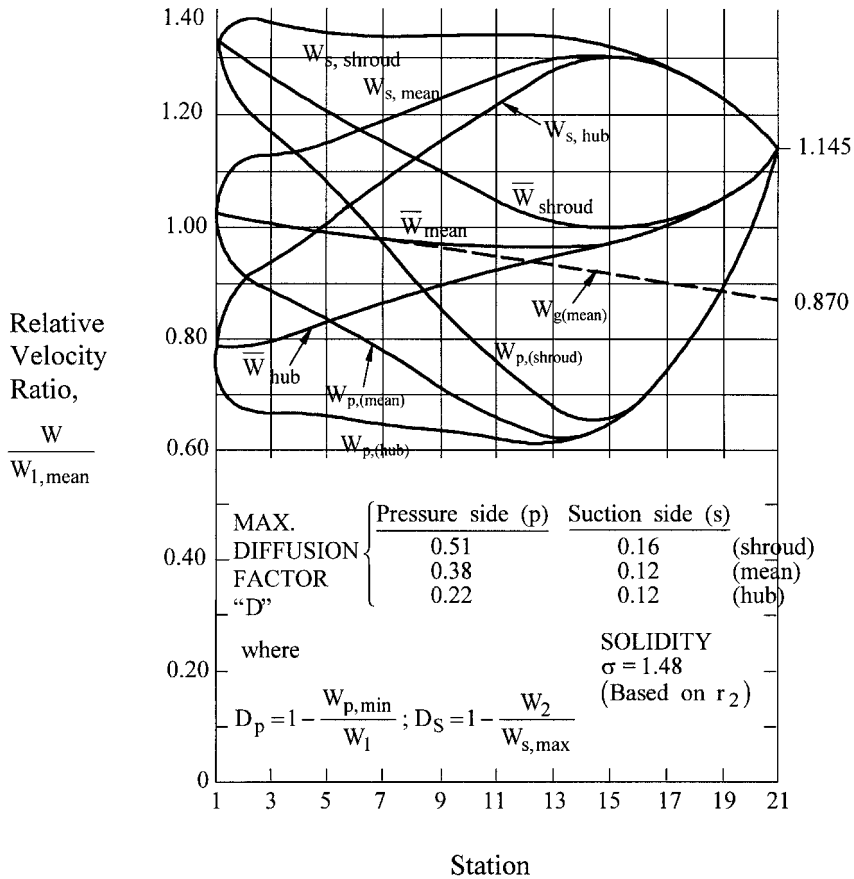

FIGURE 29 Blade surface relative velocity distributions (design example)

unlikely that it actually occurs in the 3D velocity field. Moreover, details near leading and trailing edges are not well handled by Eq. 54—a 2D blade-to-blade solution is more desirable for this type of diffusion assessment[42].

Volute Design With the exit velocity V_2 of 43.6 ft/sec (13.3 m/s) and the tangential velocity component $V_{\theta,2}$ of 40.5 ft/sec (12.3 m/s) from Figure 26b, the volute design process is started in Table 11 using Eq. 61. This entails a choice of the radial "Gap B" of 6% of the impeller radius r_2 and a tongue leading edge thickness t_t equal to 70 percent of the impeller blade thickness. These choices are not critical for a pump of low energy level such as this is, as the stresses imposed by the flow on structural elements are small. The *throat area* A_T is then found to be 32.60 in^2 (21,032 mm^2) and the throat velocity V_T computes to 24.60 ft/sec (7.50 m/s), which is 56% of V_2 and so represents considerable diffusion from impeller exit to throat. (The throat area A_T is the fundamental feature of a volute and acts in concert with the impeller exit area, as emphasized by Anderson[6] and Worster[25] and described in the earlier part of this section on *Designing the Collector* in terms of the intersection of the casing and impeller lines[26].)

The circumferential *distribution of the volute cross-sectional area* A_v versus polar angle θ_v from the tongue (Figure 20a) is developed in the latter part of Table 11, a final listing being presented for a) linear A_v versus θ_v and b) constant one-dimensional angular momentum $r_v V_v$. This listing illustrates an earlier statement that the latter approach pro-

TABLE 11 Volute casing (design example)

Refer to Fig. 20

A) Throat area A_T
Simultaneously solve for A_T from

a) $r_T \dfrac{Q}{A_T} = 0.95\, r_2 V_{\theta,2}$ (Eq. 61, using 0.95) since $A_T = \dfrac{Q}{V_T}$

and

b) $r_T = r_3 + \dfrac{1}{2}\sqrt{A_T} + t_t$ (Fig. 20, assuming a square throat)

Eliminating r_T in combining (a) and (b) yields a quadratic equation in $\sqrt{A_T}$:

c) $A_T \times \left(\dfrac{0.95\, r_2 V_{\theta,2}}{Q}\right) - \dfrac{1}{2}\sqrt{A_T} - (r_3 + t_t) = 0$

Taking $r_3 = 1.06\, r_2$ (i.e., "Gap B" = $0.06\, r_2$), $r_3 = 6.36$ in (161.5 m);
assuming $t_t = 0.7\, t_b = 0.7 \times 0.24 = 0.168$ in. (4.3 mm); and
using consistent units in (c); leads through the quadratic formula to

$A_T = 32.60$ in^2 (21,032 mm^2)

Thus $V_T = 24.60$ ft/sec (7.50 m/s)

B) Cross-sectional area

If volute cross-sectional area A_v is distributed linearly vs. θ_v, A_v and the radius r_v to the center of the cross section are as follows:

d) $A_v = A_T \dfrac{\theta_v(\text{deg})}{360} = \dfrac{32.60}{360} \times \theta_v \text{ in}^2 = \dfrac{21{,}032}{360} \times \theta_v \text{ mm}^2$

e) $r_v = r_3 + \dfrac{1}{2}\sqrt{A_v} = 6.36 + \dfrac{1}{2}\sqrt{A_T(\text{in}^2)}$ in

$= 161.5 + \dfrac{1}{2}\sqrt{A_T(\text{mm}^2)}$ mm

If A_v is found subject to constant angular momentum with $r_v V_v = 0.95\, r_2 V_{\theta,2}$,

f) $A_v = \dfrac{Q}{V_v} \times \dfrac{\theta_v(\text{deg})}{360} = \dfrac{Q\left(r_3 + \dfrac{1}{2}\sqrt{A_v}\right)}{0.95\, r_2 V_{\theta,2}} \times \dfrac{\theta_v(\text{deg})}{360}$

TABLE 11 Continued.

This is a quadratic equation in $\sqrt{A_v}$, which, when solved, gives the results for "constant $r_v V_v$" in the llisting below, r_v being found from Eq. (e) for both this and the linear case.

Volute cross sections (design example)

	Linear A_v vs. θ_v				Constant (r_v x V_v)			
θ_v	A_v		r_v		A_v		r_v	
deg	in^2	mm^2	in	mm	in^2	mm^2	in	mm
0	0.00	0	6.36*	161.5*	0.00	0	6.36*	161.5*
45	4.08	2,629	7.37	187.2	3.15	2,031	7.25	184.1
90	8.15	5,258	7.79	197.8	6.64	4,286	7.65	194.3
135	12.23	7,887	8.11	205.9	10.39	6,701	7.97	202.5
180	16.30	10,516	8.38	212.8	14.34	9,250	8.25	209.6
225	20.38	13,145	8.62	218.9	18.48	11,922	8.51	216.1
270	24.45	15,774	8.83	224.3	22.79	14,706	8.75	222.2
315	28.53	18,403	9.03	229.4	27.27	17,596	8.97	227.9
360	32.60	21,032	9.21**	234.1**	31.91	20,588**	9.18**	233.3**

* $r_v = r_3$ at $\theta_v = 0$
** transition to $r_T = 9.38$ in (238.3 mm) and $A_T = 32.6$ in^2 (21032 mm^2) due to tongue thickness

duces smaller areas upstream of the throat than does the former. Frictional effects in the smaller-A_v portion of the volute are less prominent using the linear approach. A CFD assessment at all flow rates can be made to guide the design choice here. Finally, the one-dimensional constant $r_v V_v$ method can be improved upon by integrating a constant rV_θ distribution over each cross section, and the proper design must satisfy also continuity[26].

Estimated Performance Characteristics Detailed computation of hydraulic losses, together with leakage, disk friction, and other mechanical drags was done as described previously, and the results are presented in Figure 30. The method predicts the pump efficiency to be 85.5% at the design point of 2500 gpm (0.1577 m^3/s), peaking at 86 percent at a 5% lower flow rate. The power consumption peaks at the design point at 77 hp (57 kW), indicating that this is a "non-overloading" design; that is, shaft power does not increase beyond this flow rate. The empirical methods reviewed earlier for shut-off head and power were applied here and blended into the one-dimensionally computed curves at half of the BEP flow rate.

The shut-off head coefficient value of 0.596 is close to the 0.585 value of Stepanoff[4] and is admittedly open to alteration. The rise of head from design point to shut-off is from 104 up to 161 ft (31.7 up to 49.1 m) or 55%. This percentage could be smaller and still ensure stable operation in any typical system; however, the non-overloading feature could change, the power peaking at a higher flow rate. In retrospect, the design-point head coefficient ψ of 0.385 could be larger without the diffusion-factor results of Figure 29 becoming excessive. One would conclude from this exercise that the ψ-curve of Figure 12 is conservative and could be higher. Of more significance, however, is the demonstration in this design example of the utilization of easily applied fundamental fluid dynamical analyses such as the diffusion assessment illustrated in Figure 29 as the basic arbiters of design choices such as the head coefficient, number of blades, and so on. Furthermore, the shapes of the performance characteristics are revealed.

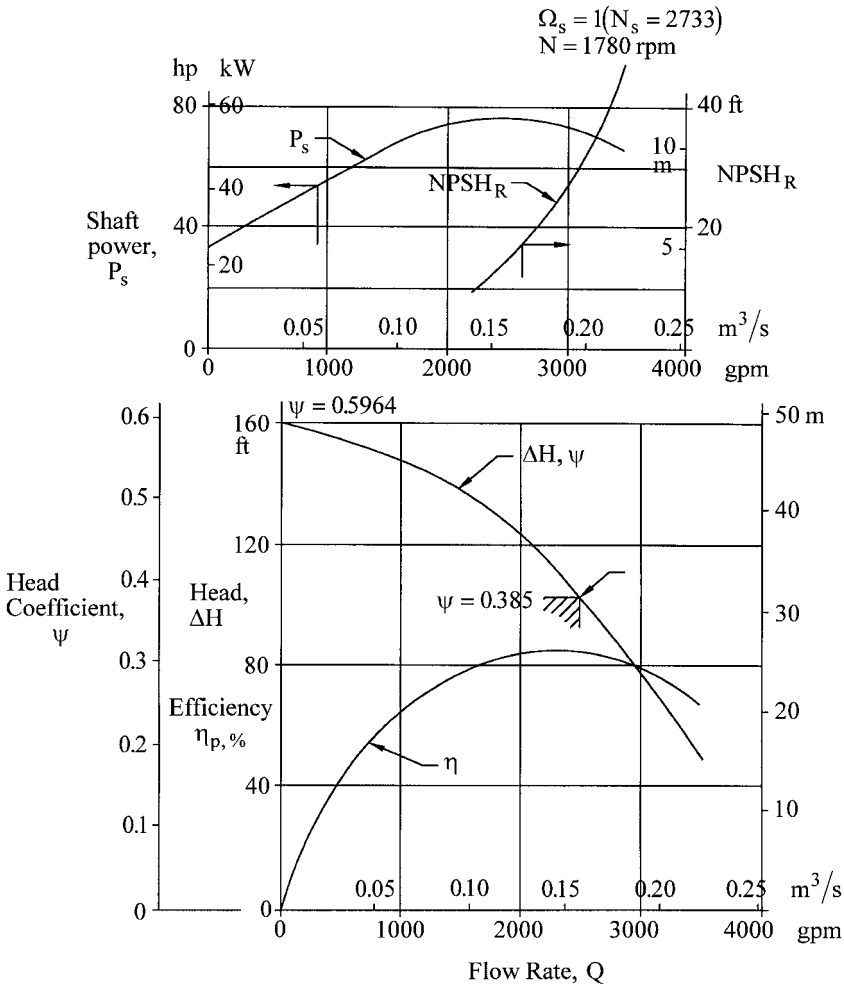

FIGURE 30 Estimated performance characteristics (design example)

The shut-off power is 34 hp (25 kW), arising from a power coefficient of 0.047 from Mockridge's correlation[36] for a b_2/D_2 of 1.59/12 (= 40.4/304.8) = 0.1325—as found from Figure 23. This is 44% of the design-point power, a typical result. As seen in Section 2.3.1, this percentage increases with specific speed, where, of course, b_2/D_2 is also larger[36].

The *NPSHR* (= $NPSH_{3\%}$ for this example) at off-design conditions is estimated empirically. At the higher, non-recirculating flow rates, *NPSHR* is related to the head required to accelerate the relative velocity within the blades to values higher than at the design point[14]. As stated in Section 2.3.1, operation at $NPSH_{3\%}$ involves performance in the presence of extensive internal two-phase behavior. This is complicated by recirculation at the lower flow rates. Therefore, the full *NPSHR* curve in such a case usually has to be established experimentally.

HIGH-ENERGY PUMPS

Over the past few decades, there has been a trend toward pumping machinery that concentrates more power within a given volume. This trend is driven by cost and technology improvements. The basic energy transfer relationships show that smaller size demands higher rotative speed. Thus, over the same time period, speeds of high-power pumps have been increasing. Moreover, the number of stages in multistage pumps has been decreasing. There have been spikes in these trends; the resulting pumps suffering from excessive vibration, rotor and hydraulic instabilities, component failure, and cavitation damage[57]. The term "high energy" has been applied to these machines, and this label can be quantified in terms of the stresses arising in critical pump components and the likelihood of an adverse mechanical response that such stress levels imply. Research has led to technical solutions for effectively controlling rotordynamic behavior and reducing unsteady hydraulic thrust and surge as well as cavitation erosion[53,58,59]. The resulting pump reliability improvements and life extension should enable the previous trends to continue. Being aware of the energy level enables the pump user to assess whether operation and maintenance difficulties are likely to occur after the pump is installed and running, and it enables the designer to take the appropriate measures to ensure the technical integrity of the product.

Pressure Pulsations Measured at the inlet or outlet port, the amplitude of the pressure pulsations can be a significant fraction of the pressure rise of the pump—especially at flow rates well below that of the BEP for the speed involved. Sources are a) the interaction of the pressure fields of the impeller and diffuser or volute, b) unsteady separated and reversed flows at impeller inlet and discharge and in the diffuser, c) cavitating flows, and d) combinations of these phenomena. Pressure pulsations presumed to exist at the impeller OD from the interaction of impeller blade-to-blade and diffuser vane-to-vane variations of pressure have been calculated by inviscid flow analysis to have a peak-to-peak amplitude that is of the same order as the static pressure rise of the impeller[60]. Moreover, the viscous, thicker wakes existing at lower-than-BEP flow rates (here called "low flows") and separated recirculating fluid from both impeller and diffuser that participate in these interactions can be expected to increase the pressure pulsation amplitude at such conditions.

Figure 31 confirms these ideas, showing a bronze impeller that operated extensively at low flow. Cavitation pitting can be observed near the OD of the impeller, which means that the rarefactions of the pressure waves were below the vapor pressure of the liquid—these pressure minima therefore being below the inlet pressure to the impeller. Moreover, the bulged-out shrouds can be assumed to be the result of the repeated occurrence of the associated pressure spikes (that is, the maxima of the pressure waves) within the radial gap ("Gap B") between the impeller blades and the diffuser vanes, the sidewall pressures on the outsides of the shrouds remaining comparatively constant. At greater values of design pressure rise than was the case for this impeller, this phenomenon creates correspondingly greater forces that have led to actual breakage of the impeller shrouds and diffuser vanes[61]. The cavitation seen in Figure 31, can also be observed on the leading edges of diffuser vanes, as in Figure 21 of Section 9.5, and this raises the possibility of diffuser vane breakage.

Energy Level: Stage Pressure Rise Even in the absence of the weakening effect of cavitation erosion, the leading edge of a diffuser vane or volute tongue is a representative, highly stressed zone within a pump that is subject to failure if the magnitude of the pressure pulsations arising from the impeller-diffuser interactions just described is sufficiently large. Thus, the hydraulically induced stresses in these vanes can be the basis for quantifying the energy level of a pump stage. In Table 12, this concept is developed into an expression for the stress in terms of the fluctuating pressure magnitude δp that is assumed to act across the vane leading edge as illustrated in the table. The width b of the vane is close enough to b_2 of the impeller exit to utilize the relationships for ψ and ϕ_i of Figure 12 to relate b/D to specific speed in Eq. (c) of the table. For similar velocity fields, the pressure pulsation magnitude δp is a constant multiplied by the stage pressure rise ΔP_{stg}. Thus, for a limiting value of stress, the concept of a limiting stage pressure rise

FIGURE 31 Damage to impeller from low-flow operation (Source: E. Makay in *Power*)

emerges in Eq. (e). The constant K is chosen from experience, which leads to the resulting Eq. (f). This relationship is plotted in Figure 32. [It will be observed that this choice for K corresponds to a limiting stress s from Eq. (d) of 6,600 psi (45.5 MPa) that would exist if δp were equal to ΔP_{stg}—with $t/D = 0.01$ and $\varepsilon = 0.85$ as in the example.] The inverse variation with specific speed is a consequence of the greater b/D of higher-Ω_s pumps (as developed in Table 12), the wider vane introducing more stress at the juncture with the sidewalls for the same pressure loading and so imposing a lower stage pressure-rise limit. Conversely, lower-Ω_s pumps should have higher limits for ΔP_{stg}.

Figure 32, therefore, illustrates this concept of a *limiting stage pressure rise* as a measure of the energy level of centrifugal pumps, the basis being a limiting stress level in a critical component of the pump. Starting with stress at other locations in the pump leads to similar results. To provide perspective, specific examples of pumps that by this definition are in the *high-energy domain* are plotted on the figure. These data points are taken from Table 13, which contains information for several well-known liquid rocket engine turbo pumps[62,63,64] and for some representative high-energy electric utility boiler feed pumps[53,57].

The last column in Table 13 is another, more general way of comparing the energy level of these machines; namely, the *torque per unit volume*, which also has the dimensions of stress. For fixed ratios of stage width, casing OD, and other dimensions to impeller radius r ($= r_2$), torque per unit volume differs from the listed values of torque/r^3 by a factor. The actual torque per unit volume therefore ranges from one-half to one-sixth of the tabulated

TABLE 12 Hydraulically induced stress levels

- Stress at juncture of diffuser vane leading edge with sidewall:

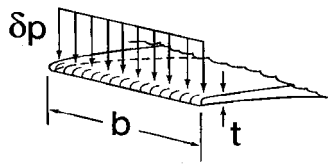

$$s = \frac{\delta p\, b^2}{2t^2} = \frac{(\delta p/2)(b/D)^2}{(t/D)^2} \qquad (a)$$

- From Fig. 12 and Eq. 36:

$$\frac{b}{D} = \frac{Q}{V_{m,2}\, 2\pi r_2 \varepsilon D} = \frac{Q}{\Omega r_2 \dfrac{V_{m,2}}{\Omega r_2} 4\pi r_2^2 \varepsilon} = \frac{Q_s}{\phi_i 4\pi \varepsilon} \qquad (b)$$

- From Eq. 50:

$$\frac{b}{D} = \Omega_s^2 \psi^{3/2} / (4\pi \phi_i \varepsilon) \qquad (c)$$

- With $\psi \approx 0.383/\Omega_s^{1/3}$ and $\phi_i \approx 0.1715\sqrt{\Omega_s}$

the stress Eq. (a) becomes, with Eq. (c)

$$s = \frac{\delta p \times \Omega_s^2}{165 \times (t/D)^2 \varepsilon^2} \qquad (d)$$

- Example for t/D=0.01, ε=0.85, Ω_s=0.6 and δp=1000 psi (6.895 MPa):

$$s = \frac{1000 \times (0.6)^2}{165 \times (0.01)^2 \times (0.85)^2} = 30{,}198 \text{ psi } (208.2 \text{ MPa})$$

- For δp being proportional to ΔP_{stg}, and for a fixed geometry and a given limiting value of stress, Eq. (d) becomes

$$\Delta P_{stg} = K/\Omega_s^2 \qquad (e)$$

- Experience leads to a choice of K such that

$$\Delta P_{stg} = \frac{78.72}{\Omega_s^2} \text{psi} = \frac{0.5427}{\Omega_s^2} \text{MPa} \qquad (f)$$

torque/r^3, depending on the casing or barrel thickness, and so on. However, as has been demonstrated, the critical stresses are more closely associated with the impeller OD, which makes comparison of the tabulated values more relevant. Thus, a pump with high torque/r^3 can be expected to have correspondingly high local internal stresses. The maximum values listed, namely for the high-pressure propellant pumps on the RD-170 (Russian) and SSME (U.S. Space Shuttle) engines, tend to explain the high level of research and development that was necessary to successfully deploy these machines. Illustrations of some of these rocket engine pumps can be found in Section 9.19.2. Similarly, Section 9.5

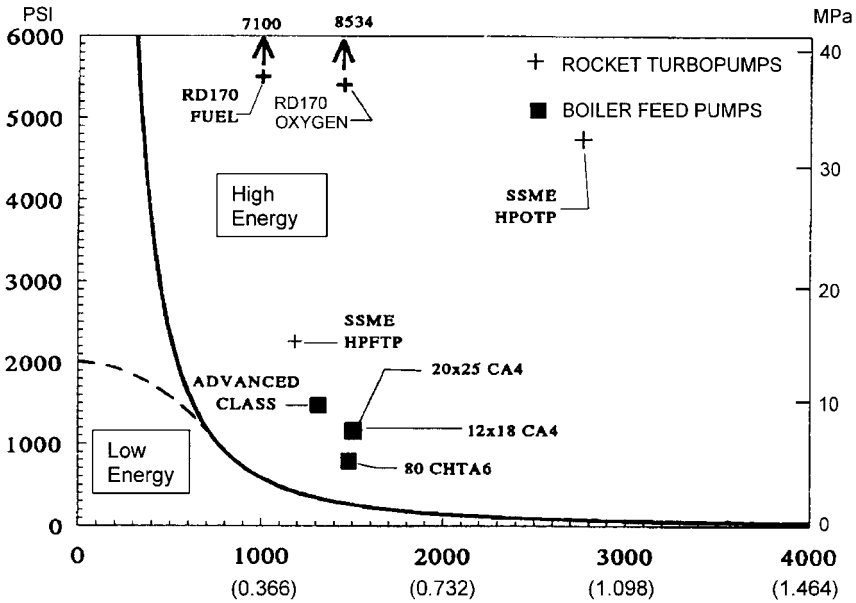

FIGURE 32 Pump energy level defined in terms of stage pressure rise

provides examples of high-energy boiler feed pumps: the massive, barrel-type construction of these machines is illustrated in Figure 18. Specifically, the first boiler feed pump listed in Table 13 is the sole feed pump supplying the steam generator of a super-critical 1300 MW electric generating unit and consumes nearly 50 MW of shaft power. It can be seen in Figures 7 and 20 of Section 9.5.

For pumps in the *low-energy domain* of Figure 32, normal design and manufacturing practices result in a more benign mechanical response to the abnormal fluid phenomena discussed here. However, for locations other than the diffuser entrance, which was the basis for the development of the figure, limiting stresses could be reached at considerably lower values of stage pressure rise. For this reason, the dashed line is offered as the upper limit of the low-energy domain; however, a thorough analysis of the stresses in any given application is the ultimate determinant of all the limits suggested in Figure 32 and of the acceptability of the design. It can now be seen that the design example treated earlier in this section is of the low-energy variety; therefore, the special design problems treated here and further on are of relatively little concern in such pumps. On the other hand, if the curve in Figure 32 were extended to much *higher specific speeds*, it would be found that many existing, large, high-Ω_s, low-head pumps are high-energy machines by this stress-related definition. It is therefore not surprising that such pumps generally require full stress and modal analyses to identify possible destructive resonances and stresses.

Fluid/Structure Interactions With the dimensions of pump energy level identified, the next step is to continue the examination of the problems mentioned previously and the methods that have become available for solving them. Attention is focused on hydraulic phenomena because, as the previous discussion of pressure pulsations implies, most of the adverse mechanical behavior exhibited by pumps originates from the behavior of the internal flow field. Excessive measured vibrations, material erosion, and component failures are often the external symptoms of fluid/structure interaction phenomena that are fundamentally explained from a hydraulics perspective. In addition to the hydraulically

TABLE 13 Data on high-energy pumps*

Pump	No. of stages	Speed rpm	Flow rate gpm (m^3/s)	Head/stg ft (m)	ΔP/stg psi (MPa)	Specific Spd N_s (Ω_s)	Torque/r^3 psi (MPa)
Liquid Rocket Propellant Turbopumps							
Saturn V Booster – F1 Engine: Oxygen	1	5,490	25,080 (1.582)	3,100 (945)	1,530 (10.5)	2,095 (0.767)	371 (2.6)
Saturn V Booster – F1 Eng: Fuel (RP1)	1	5,490	15,640 (0.986)	5,100 (1,555)	1,810 (12.5)	1,130 (0.413)	172 (1.2)
Space Shuttle Main Engine: Oxygen (= SSME HPOTP)	1	31,100	7,240 (0.457)	9,700 (2,957)	4,800 (33.1)	2,700 (0.988)	1,431 (9.9)
Space Shuttle Main Engine: Fuel (H_2) (= SSME HPFTP)	3	37,400	16,300 (1.028)	66,700 (20,330)	2,280 (15.7)	1,150 (0.421)	200 (1.4)
RD-170 – Oxygen	1	13,850	25,008 (1.578)	17,300 (5,273)	8,534 (58.8)	1,448 (0.530)	1,521 (10.5)
RD-170 – Fuel (= RP1)	1	13,850	14,485 (0.914)	20,000 (6,096)	7,100 (49.0)	992 (0.363)	698 (4.8)
Boiler Feed Pumps							
20x25 CA-4 (IDP)	4	4,160	21,620 (1.364)	3,000 (914)	1,169 (8.1)	1,509 (0.552)	128 (0.9)
12x18 CA-4 (IDP)	4	5,800	11,000 (0.694)	3,000 (914)	1,169 (8.1)	1,500 (0.549)	130 (0.9)
80CHTA-6 (IDP)	6	5,800	6,250 (0.394)	2,100 (640)	820 (5.7)	1,479 (0.541)	87 (0.6)
Advanced Class (Sulzer)	2	6,500	9,510 (0.600)	3,800 (1158)	1,480 (10.2)	1,312 (0.480)	136 (0.9)

**Notes to this table:* Flow rates apply to the pump inlet. RD-170 pump data derived from Sutton[62] and Advanced Class boiler feed pump data from Ref. 57. Remaining data derived from Table 1 of Section 9.19.2, NASA reports[63,64] and from information supplied by Flowserve Corporation.[53]

induced stresses in the pump structure that culminated in the domain definition of Figure 32, these phenomena encompass a) blade-vane interactions, b) recirculation, c) anomalous axial thrust behavior, and d) cavitation.

In order to illustrate the methods for dealing with the problems created by these fluid/structure interactions, a sample suction stage of a high-energy multistage pump is utilized as the quantifying focus in each case. Table 14 contains the conditions and essential features of this machine, a meridional view of which is shown in Figure 33. As with the earlier design example, this stage has been designed in accordance with the procedures outlined for that example. This includes the velocity diagrams shown in the figure, as well

TABLE 14 Data for high-energy pump suction stage

A. Design Inputs

Fluid: Boiler feed water at 350°F (177°C) ⇒ sp. gr. = 0.89, ν = 0.17 cs.	
Flow rate, Q, gpm (m^3/s)	20,000 (1.262)
Head rise, ΔH, ft (m)	3,000 (914.4)
Rotative speed, N, rpm	4,700
Outlet flow coefficient, ϕ_2 (Figure 12)	0.1328
Head coefficient, ψ (Figure 12)	0.455
Specific speed, Ω_s (N_s / n_q)	0.6 (1640/32)
Inlet flow coefficient, ϕ_e	0.3 (=tan 16.7 deg.)
Number of Impeller blades, n_b	7
Number of Diffuser vanes, n_v	9

B. Calculated Perfomance Data

1. Efficiency
   a) BEP of 20,000 USgpm (1.2618 m^3/s)
   $\eta = \eta_p = 0.877$ (vs. η=0.8682 - from Fig 10, for X=1)
   $\eta_{hy} = 0.900$
   $\eta_m = 0.985$
   $\eta_v = 0.989$ [216 gpm (0.0136 m^3/s) front ring leakage; rear ring leakage included in η_{hy}]

   b) At 50% Flow : $\eta_p = 0.693$ (= 0.79 of η_{BEP} ; 0.8 is typical)

2. Head Rise
   $\Delta H_{BEP} = 3000$ ft. (914 m) ⇒ $\psi = 0.455$
   $\Delta H_{shutoff} = 3697$ ft. (1127 m) ⇒ $\psi_{s/o} = 0.560$
   ΔH-vs-Q curve stability indicator, $\Delta H_{s/o}/\Delta H_{BEP} = 1.23$ (doubtful if less than 1.2)

3. Power

$$P_{s,BEP} = 15{,}376 \text{ hp } (11{,}466 \text{ kW}) \sim \hat{P} = 0.0571$$

$$P_{s,SHUTOFF} = 6{,}144 \text{ hp } (4{,}583 \text{ kW}) \sim \hat{P}_{s/o} = 0.0228 \; (= 0.01966 \times 1.16 \text{ from Fig. 23})$$

$$\uparrow$$

$$= K \text{ for } \frac{b_2}{D_2} = 0.0779$$

as the design of the eye, the hub and shroud profiles, and the blading. A preliminary design was also made of the vaned diffuser and return vanes, following the guidelines presented in the foregoing *Design Procedures* subsection. The result is a representative machine to which the following paragraphs continually refer.

Blade-Vane Combinations Certain numerical combinations of impeller blades and diffuser vanes (or inlet guide vanes, where they are employed) have been shown to have acoustic consequences that can exacerbate the pressure pulsations arising from the interaction of impeller and diffuser flow fields. Bolleter reviewed the types of interactions that can occur and the consequences with regard to pressure pulsations and resonance[33]. These

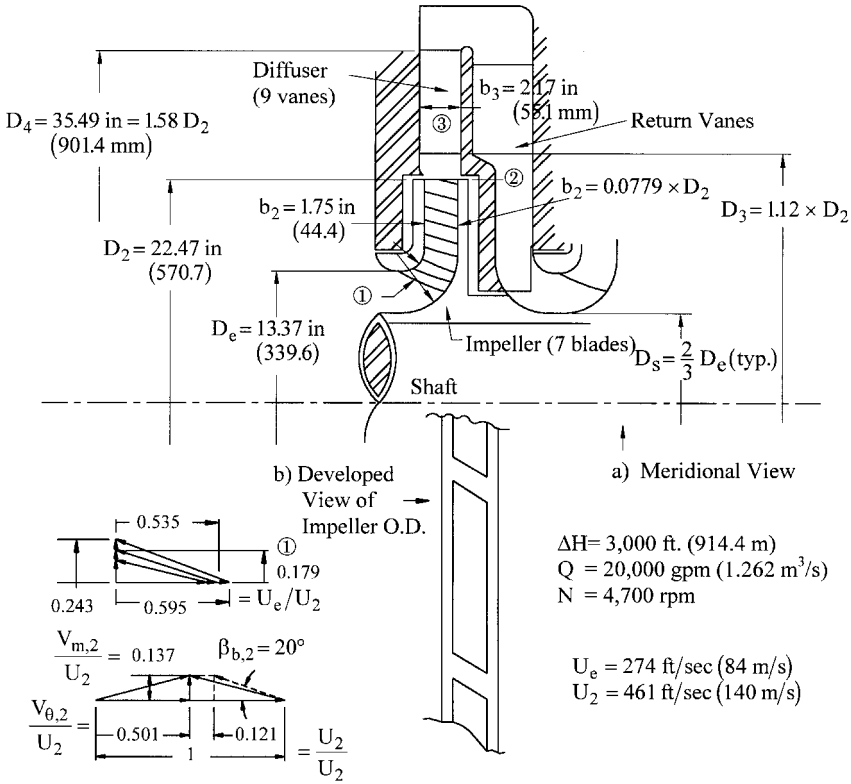

FIGURE 33 Sample suction stage of high-energy multistage pump

types are associated with the integer difference m between the multiples of the number of impeller blades and the number of diffuser vanes, as explained in Table 15. To check the blade-vane combination, one simply forms a matrix of the multiples as shown and lists the difference in each cell.

To illustrate the method, rather than use the pump of Table 14, a different example is chosen in order to dispel the notion that one can always use two different prime numbers for blade-vane combinations. This is an existing case of a 60,000 *hp* (45 MW) single-stage pump of $\Omega_s = 0.6$ ($N_s = 1640$) and $\Delta p = 357$ psi (2.46 MPa), which has 7 impeller blades and 13 diffuser vanes[65]. Notice that $m = 1$ in the second order of impeller blade number, which means there should be pressure pulsations at $2 \times 7 \times$ rpm/60 Hz. In fact, this pump has exactly this vibration and pressure pulsation frequency in the field, not least because the pump is operating at just the right speed for the acoustic waves emanating from successive interaction points to reinforce each other in producing unacceptable pressure pulsations.

Even with this simple method, the final choice of the blade-vane combination is usually a compromise. For example, the method shows that all double-volute pumps have $m = 0$ or 1 in the first order of impeller blade number, depending on whether this number is even or odd. $m = 0$ means that the all the blades or vanes are interacting at the same instant, a consequence of which is torque ripple. High-energy volute pumps exist for both even and odd cases—quite large gaps between blades and vanes (= "Gap B") are employed to mitigate these effects.

The reader who checks the pump of Table 14 by this method will find that $m = 2$ in the first order of both blades (7) and vanes (9) but that $m \neq 0$ everywhere else in the matrix.

TABLE 15 Choosing vane combinations to minimize pressure pulsations[33]

1. Z_i is the number of impeller blades.
2. Z_d is the number of diffuser vanes.
3. Each vane combination produces interacting pressure fields between the blade rows.
4. These fields form "m" rotating "nodal diameters", producing unsteady loads
5. The value of "m" determines the nature and severity of these loads.
6. "m" is the difference between (p x Z_i) and (q x Z_d), where p and q are integers.
7. To find "m", one sets up a matrix of diffuser vanes and their multiples vs. impeller blades and their multiples or "orders". A minimum of the first three orders should be used. This is illustrated as follows for an impeller with 7 blades (Z_i=7) and a diffuser with 13 vanes (Z_d=13):

		Impeller blades and their multiples:			
		p=1 7(=Z_i)	p=2 14	p=3 21	p=4 28
Diffuser vanes and their multiples:		Differences "m" between (p x Z_i) and (q x Z_d) are give below:			
q=1	13(=Z_d)	6	1	8	15
q=2	26	19	12	5	2
q=3	39	32	25	18	11

The significant values of "m" are 0, 1 and 2. The lower the order of either the impeller blades or the diffuser vanes, the stronger is the interaction. The responses that occur for these "m" values are as follows:

- m = 0 - strong pressure pulsations and fluctuating axial loads and torsional forces.
- m = 1 - pressure pulsations and fluctuating radial loads.
- m = 2 - small pressure pulsations and a chance of resonance of the impeller about the two nodal diameters - at a frequency equal to the value of q x Z_d times the rotational frequency (rpm or rps)

In this example, m = 1 in the second order of the impeller blades (i.e., p=2); thus, the frequency of the resulting disturbances will be twice that of blade passing frequency p x Z_i x rpm or 2 x 7 x rpm cycles per minute or 2 x 7 x rpm/60 Hertz. This is therefore a poor vane combination and should be avoided - especially for such low orders of vane number; i.e., for such small values of p and q, (Here, p=2 and q=1.) In general, m = 0 and 1 should be avoided altogether, and m = 2 should be avoided in the lower orders.

$m = 1$ occurs only in the highest orders of both and should therefore be of little consequence. Checking whether 10 or 11 vanes would be better yields $m = 1$ in the third order of impeller blades and second order of diffuser vanes, which is probably less desirable than $m = 2$ in the first orders. Therefore, Figure 33 shows a value of "Gap B" that is 12 percent of the impeller radius, which should provide adequate protection from pressure pulsations and excitations of resonance. (The gaps at the impeller OD will be discussed further on.)

Recirculation Separation and stall of the fluid flowing in the passages of impellers and diffusers occurs at low flow because of the incidence and large reduction in the one-dimensional velocity relative to the passage that happens at low flow. This and the con-

sequent recirculation patterns in the impeller were discussed and illustrated in Figure 6. Fischer and Thoma[66] visually observed and recorded the flow patterns, finding that as flow rate is reduced, wakes on the suction side of all blades thicken until they occupy half the passage width at half the BEP flow rate. At lesser flow rates, the wakes continue to thicken but become irregular, stalling in one passage and not the others—the stall pattern moving into and out of adjacent passages and so rotating relative to the impeller. As shut-off is approached, this rotating pattern is accompanied by reversed flow emerging from the inlet of the stalled passage. Fraser, working with typical impeller geometries, formulated rules for computing the flow Q_{SR} at which this reversal occurs as Q is reduced at constant speed[67]. His expressions, found further on, include the effect of impeller eye size on Q_{SR}. As one might expect, a pump with an eye diameter approaching that of the impeller OD will have Q_{SR} approaching Q_{BEP}. At $Q < Q_{SR}$, the impeller flow patterns are highly unsteady—as is usually the case with massively separated flows—creating nonsynchronous, low-frequency or random pressure pulsations, the resulting shear layers between the reverse-flowing and in-flowing fluid having vortices with locally low pressures so cavitation can also exist. Fraser also quantified the flow rate Q_{DR} below which impeller discharge recirculation exists. Forces from such motion can cause fatigue failure of the impeller blades, diffuser vanes or volute tongue, cavitation erosion also playing a part as in Figure 31. In Section 2.3.2, Fraser describes the identification and consequences of recirculation in detail, the more general designation Q_R referring to either Q_{SR} or Q_{DR}, depending on whether Q is between or below both.

The ability for pumps to operate with any form of separation; stall; or, worse, flow reversal (recirculation) depends on the energy level. This can be approximately quantified, as outlined under the subject of *Minimum Flow Limits* further on, which include consideration of accompanying cavitation activity.

Axial Thrust Response to Recirculation Discharge recirculation usually involves backflow from the diffuser, itself containing oscillating flow patterns and rotating stall. Fluid emerging from the diffuser will be spinning opposite to the direction of rotation, such fluid having a major effect on the sidewall gap flows as it joins the leakage flows described under *Predicting Axial Thrust*. As this fluid invades the sidewall gaps, it can slow or virtually cancel the usual positive swirling of the gap fluid. Iino, Sato, and Miyashiro experimentally observed and recorded this behavior, which was exaggerated by shifting the impeller axially and by changing the ring clearances[68].

An added, not unexpected effect is that as Q is reduced below Q_{DR}, the invading flow from the diffuser can favor the front or back side of the impeller and then *switch sides* upon further reduction of Q. This effect is clearly seen in the experimental thrust-versus-Q plots of Figure 34, the impellers having been shifted as just described. Depicted there is the resulting net load on the axial thrust bearing of an eight-stage, 3600-rpm diffuser pump that had a cylindrical balancing drum (not a self-compensating balancing disk). The drum was sized so as not to completely eliminate the thrust—in order to avoid thrust reversals. The solid lines are the predicted net thrust according to the methods outlined in Table 4 for three axial positions of the impeller. The large excursions in net thrust were eliminated by restricting the entry of the invading diffuser backflow into the sidewall gaps —through a tightening of the gap between the shrouds of impeller and diffuser (Gap "A") in Figure 35. Gap "A" is not effective unless the "overlap" of the two mating shrouds is from four to six times the gap dimension[61]. Moreover, if Gap "A" is minimized, this can exaggerate the blade-vane interactions, making it necessary to open up Gap "B" more than would be necessary were Gap "A" not minimized[69].

A further possibility that has been observed in a single-stage double-suction pump is the *unsteadiness* of impeller discharge recirculation and, most likely, of the diffuser or volute backflow. The side-to-side switching just mentioned appears in Figure 36 to be happening as a function of time as well as of flow rate Q, as evidenced by the axial motion, which is accompanied by discharge pressure pulsations. The "fix" mentioned in the figure was, again, mainly minimizing Gap "A."

Closing Gap "A" and opening Gap "B" are procedures that have been widely and successfully applied in high-energy pumps, which usually work well at BEP but run into difficulties at low flow[69]. The procedures have proven to cure the thrust and pressure

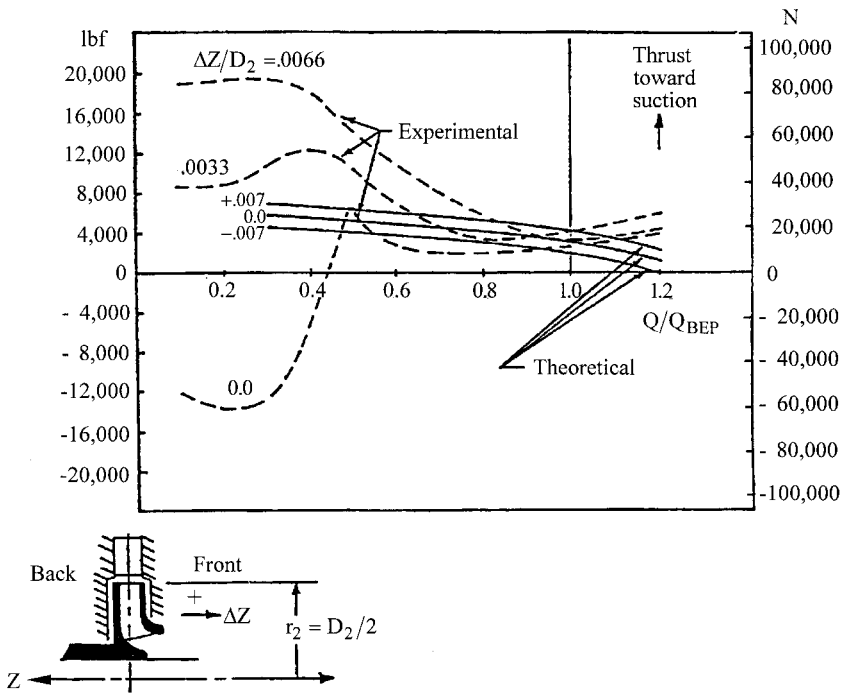

FIGURE 34 Axial thrust response to recirculation. (Source: Flowserve Corporation)

pulsation behavior just described and also improve the low-flow performance curve shape[65]. The results are high-energy pumps that can operate smoothly over a wider range of flow rate than—in many cases—was originally expected or specified. Nevertheless, the higher the energy level, the more intolerable is any unsteadiness and pressure pulsation activity.

Minimum Flow Limits Because the intensity of pressure pulsations and the accompanying vibrations can increase beyond acceptable limits as flow rate is reduced at constant speed below the BEP flow, or more specifically, below Q_R, expressions for how low Q/Q_{BEP} can be without exceeding these limits have been developed. Manufacturer and user groups such as the Hydraulic Institute (HI), the International Standards Organization (ISO), and the American Petroleum Institute (API) have specified vibration limits that must be met at what is usually called at the minimum continuous stable flow (*MCSF*) or simply Q_{min}. In an attempt to answer the question of how far into the recirculation zone (where $Q < Q_R$) an operator can take a pump before reaching the *MCSF*, Gopalakrishnan proposed a general rationale for computing Q_{min} that takes the energy level into account—through the flow rate and rotative speed of the machine[70]. These two quantities imply the blade tip speed at the inlet of the impeller. (Through typical ratios of impeller OD to eye diameter, this also implies the OD tip speed and therefore the head, the energy level having been defined in Figure 32 in terms of stage pressure rise Δp_{stg}.) The theory for this method is defined in Part A of Table 16, in which Q_{min} is computed as the product of a series of K-factors multiplying the value of Q_R, which is computed according to Fraser's earlier development[67]. Conceptually, the product of these factors approaches unity in the maximum-energy case, where the instabilities accompanying any recirculation at all are

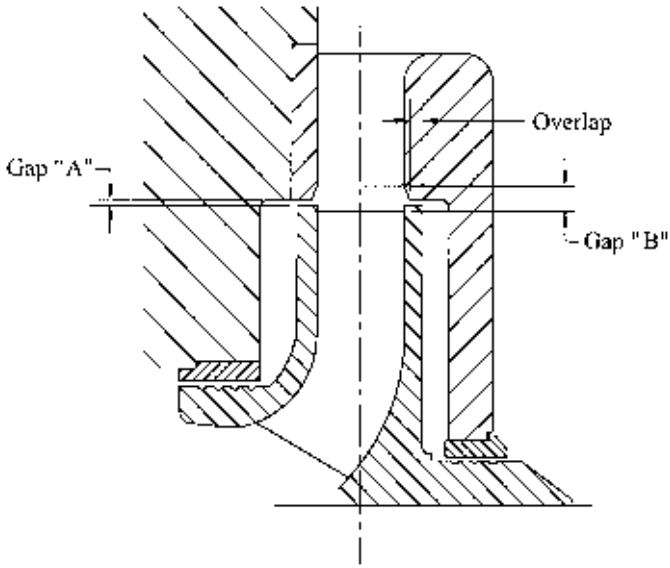

FIGURE 35 Gaps at impeller periphery[61]

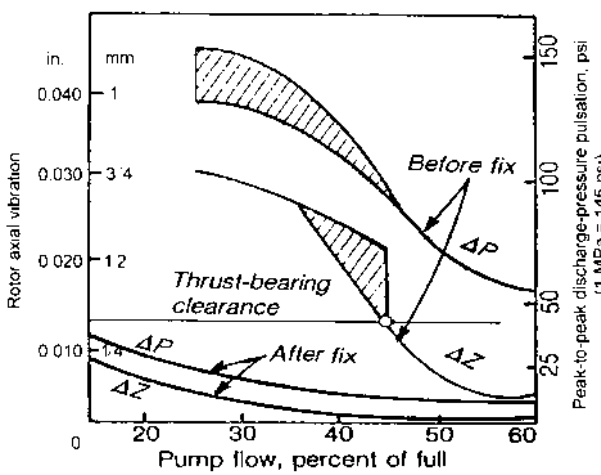

FIGURE 36 Eliminating unsteady thrust and pressure pulsations (Source: E. Makay in *Power.*)

significant. Conceivably, this product could exceed unity at the highest energy levels, as separation and stall and the attendant unsteadiness must occur—as Q is reduced—before the backflows that characterize Q_R, which was observed by Fraser as the value of flow rate for the onset of recirculation (see Section 2.3.2).

K_1 and K_3 are given in Table 16 as equations that have been curve-fitted to speed/flow rate- and *NPSH*-effect charts that appeared in Gopalakrishnan's presentation[70]. This includes the ability to enter any speed (rpm) into the computation for K_1, only 3500 and

1800 rpm having explicitly appeared in the charts. *NPSH* plays a role in the determination of Q_{min}—through the factor K_3—because of the exacerbation of the unsteadiness and pressure pulsations due to dilation of the cavities in the two-phase internal flows that exist for any value of *NPSH* that is less than the inception $NPSH_i$. (See the ensuing cavitation discussion and the description in Section 2.3.1 that accompanies the definition of *NPSH*-limits.)

As an example, the minimum flow of the high-energy pump suction stage of Table 14 and Figure 33 is computed in Part B of Table 16. (The value of R for the calculation of K_3 is taken from Table 18.) This machine has the relatively high energy level of some of the boiler feed pumps shown in Figure 32 and listed in Table 13. Thus it is not surprising that the resulting value of Q_{min} is 90% of Q_R (which equals Q_{SR}, as is typical) and 48.5% of the BEP flow rate. This is indicated on Figure 37, in which the computed performance curves

TABLE 16 General method for computing minimum flow: quantifying the energy-level effect on Q_{min} relative to Q_R[70]

A) Theory

$$Q_{min} = Q_R \quad K_1 \quad K_2 \quad K_3 \quad K_4 \quad K_5, \text{ or } Q_R, \text{whichever is smaller (i.e., product of K's} \le 1)$$

$$Q_R = \begin{cases} Q_{SR} & \text{if } D_e \ge 0.5\, D_2 \\ Q_{DR} & \text{if } D_e \le 0.5\, D_2 \end{cases}$$

$$Q_{DR} = \pi D_2^{\,2}\, b_2\, \frac{\Omega}{2}\, \overline{C_{DR}}$$

$$\overline{C_{DR}} = -0.01 + \beta_{b,2}\,^{\circ} / 218.75$$

$$Q_{SR} = \pi \Omega r_e^3 \left(1 - \frac{D_s^2}{D_e^2}\right) \cdot \overline{C_{SR}}$$

$$\overline{C_{SR}} = \tan\beta_1 \cdot \left\{1 - 0.2091 \cdot (\beta_1\,^{\circ} - 9.5)^{0.4}\right\}$$

$$K_1 = \left[0.06862 \times \left(\frac{N - 1800}{1700}\right)\right] + Y + 0.3843 \log_{10} Q$$

$$Y = \begin{cases} -0.4529 \text{ for Q in gpm} \\ +1.1612 \text{ for Q in } m^3/s \end{cases}$$

K_2 = Specific gravity

$$K_3 = \begin{cases} 0.6 + 0.4 \times \left[\frac{1}{3}\left(\frac{4}{R} - 1\right)\right]^{1.1} & \text{Pump with shaft through eye} \\ 0.7 + 0.3 \times \left[\frac{1}{3}\left(\frac{4}{R} - 1\right)\right]^{1.1} & \text{End - suction pump} \end{cases} \qquad R = \frac{NPSH_A}{NPSH_{3\%}}$$

$$K_4 = \begin{cases} 1 & \text{Continuous operation at minimum flow} \\ 0.7 & \text{Operation at minimum flow less than 25\% of total operating time} \end{cases}$$

$K_5 = 1$ No specific mechanical design margins

TABLE 16 Continued.

B) Results for Sample High-Energy Pump Suction Stage (See Fig. 33)

$Q_R = Q_{SR}$, since $D_e \geq 0.5\, D_2$

$$Q_{SR} = \pi\, \Omega\, r_e^3 \left(1 - \frac{D_s^2}{D_e^2}\right) \cdot \overline{C_{SR}} = \pi \times 4700\, \frac{\pi}{30} \times \left(\frac{6.6855}{12}\right)^3 \cdot \left(1 - \frac{2^2}{3^2}\right) \times \overline{C_{SR}}\ \frac{ft^3}{sec.}$$

and $\overline{C_{SR}} = 0.3 \cdot \left\{1 - 0.2091 \cdot (16.7 - 9.5)^{0.4}\right\} = 0.1618$

$Q_{SR} = 24.03\ ft^3/sec = 10{,}785\ gpm\ (0.6804\ m^3/s) = 0.540 \times Q_{BEP}$

$K_1 = 1.317$; $K_2 = 0.89$; $K_3 = 0.768$; $K_4 = 1$; $K_5 = 1$

$Q_{min} = 10{,}785 \times 0.9002 = \underline{9{,}709\ gpm\ (0.613\ m^3/s) = 0.485\ Q_{BEP}}$

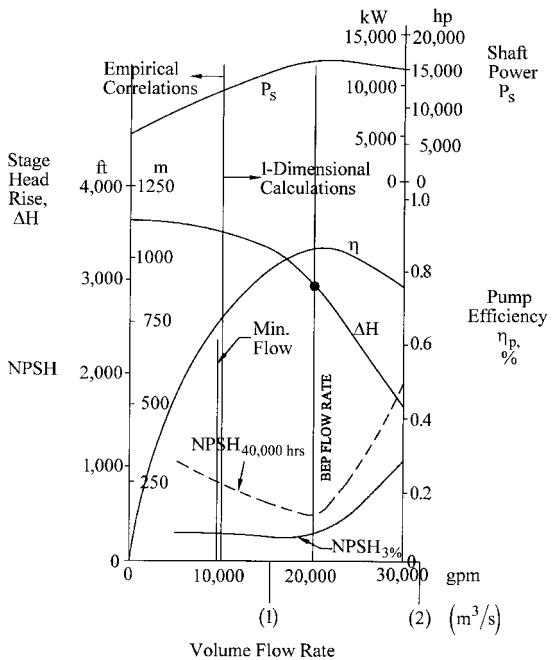

FIGURE 37 Estimated performance of high-energy pump suction stage

of this pump are displayed. (See Part B of Table 14 for the main elements of these performance predictions.) However, some of the remedies that have been discussed in this section to counter the adverse effects of high-energy pump phenomena can reduce Q_{min} to lower values than this. In fact, the method contains the flexibility to take into account such improvements through the factor K_5.

In computing Q_{SR}, the angle β_1 is called for. This is approximated by the inlet flow coefficient $\phi_e = 0.3$ from Table 14, which corresponds to a nominal inlet tip flow angle of 16.7 deg. The actual flow angle (and blade angle) at that location is slightly larger due to the hub-to-shroud variation of the incoming meridional velocity as assumed in the development of the inlet velocity diagrams of Figure 33. This will have a small effect on the results, depending on how one interprets "β_1". In this regard, as can also be appreciated from the choices that must be made for the *K*s, the method of Table 16 is not precise; however, it is a useful indicator of what the user and designer can expect in determining the operating range of a pump.

The above general theory for computing minimum flow is inclusive of all types of centrifugal pumps and has found application especially for high-energy pumps, which can be difficult to evaluate precisely in the varying circumstances of installation and operation in which they are usually applied. The judgments that must be made in order to apply the method of Table 16 can be largely avoided if actual data for $Q_{\min}$ are available. It would in fact be a monumental task to establish precise limits for all pump types and operational envelopes. Nevertheless, the effect of energy level on *MCSF* has been found experimentally for several classes of API process pumps through extensive testing. From this, Heald and Palgrave have developed a method for computing the minimum flow of these pumps as follows[71]:

$$Q_{\min} = \text{MSCF} = \frac{K_7}{100} K_M \times Q_{\text{BEP}} \tag{68}$$

where

$$K_7 = K_7(\text{rpm, configuration, } N_{SS}) \tag{69}$$

and

$$K_M = K_M[(NPSH_A/NPSH_R)_{\text{BEP}}, \text{ fluid}] \tag{70}$$

Obtained from Figure 38, the factor K_7 accounts for the effects of speed and configuration. As used in that chart—and in Eq. 69, the term *suction-specific speed* N_{ss} (or Ω_{ss})

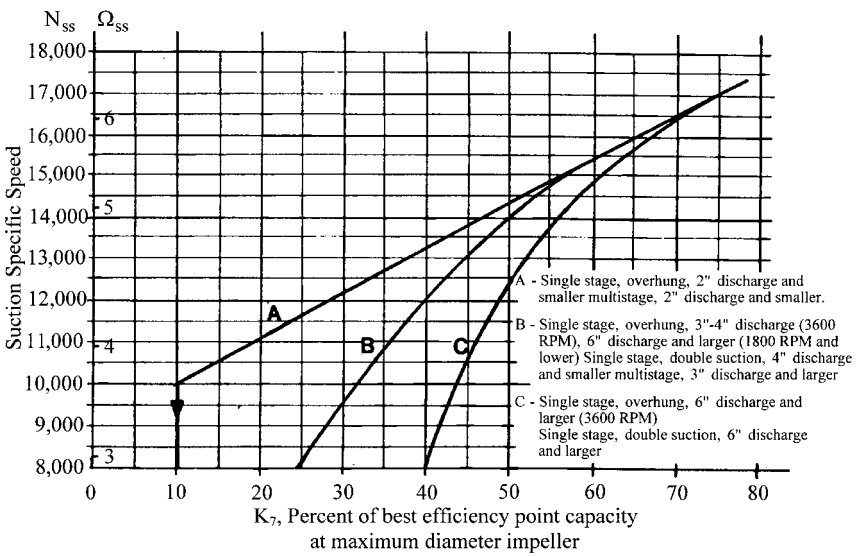

FIGURE 38 Minimum continuous stable flow (MCSF) for process pumps[71]

does not mean that *NPSH*-effects are also included; rather, this expresses the fact that the impeller design is affected by the designer's choice of N_{ss} as can be seen in the case of the earlier *Design Example*, beginning in Table 6. This leads immediately in Table 7 to the inlet flow coefficient ϕ_e (through the *NPSH*-correlations of Table 1) and the impeller eye diameter D_e or radius r_e. Following on from the discussion of *Recirculation*, the ratio Q_{SR}/Q_{BEP} can be expected to increase with eye size or D_e/D_2. Being strictly based on experiments, the Heald and Palgrave method does not deal explicitly with Q_{SR} or Q_{DR}, but one can see from Eq. 38 that this principle is operative: Higher-N_{ss} pumps require greater *MCSF*. Before this fact was clearly understood, the trend was to design for greater N_{ss}—in order to increase suction capability of these pumps. When operators ran them back to the same low flows as they had done with earlier pumps designed for lower-N_{ss} capability, failures became epidemic. This led to a call for "lower-suction specific speed pumps," or, more accurately, pumps designed for lower-N_{ss} capability; specifically 11,000 ($\Omega_{ss} = 4$) or less[72].

The *NPSH*-effect does come into play—as with K_3 in the previous general method — through the factor K_M in Figure 39a. In this case, the term $NPSH_R$ means $NPSH_{3\%}$. Here again, it is the ratio $R = NPSH_A/NPSH_R$ that is the determining factor because it is a measure of the cavitation activity that is invariably present in the first stage of a pump, and

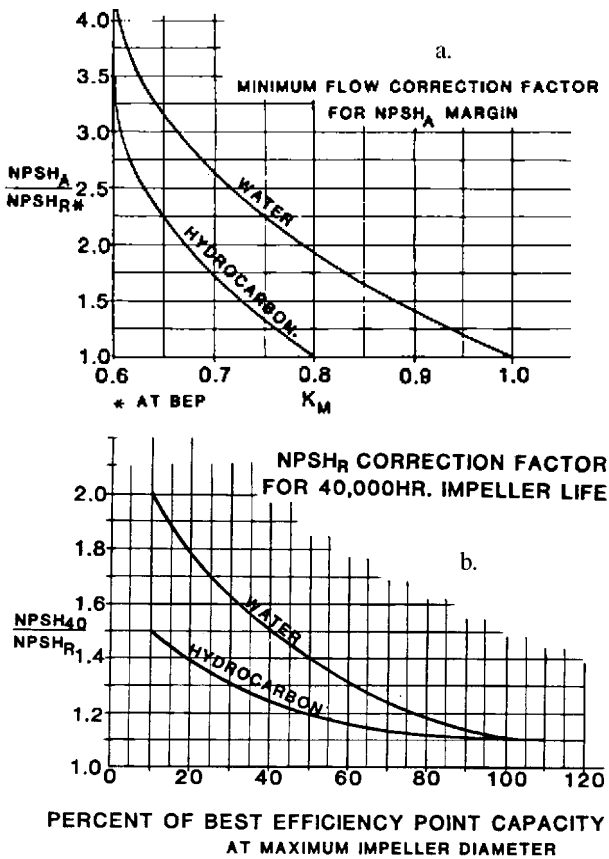

FIGURE 39 *NPSH*-effects on: a) MCSF and b) impeller life[71]

therefore in all single-stage pumps. The lower the value of R, the more violent the pressure pulsations accompanying the recirculating fluid and the consequent vibration. The situation is mitigated considerably at greater R, and K_M operates through Eq. 68 to decrease the *MCSF*. Of course, if R were great enough—often 5 or more—$NPSH_A$ would exceed $NPSH_i$ (as discussed in Section 2.3.1) and there would then finally really be no cavitation in the pump. (That high a value of *NPSHA* is rare; for, if it were supplied, there would hardly be a need for a pump in the first place.)

Figure 39a also brings in the effect of the liquid being pumped. When room temperature water boils (cavitates), the mass boiled off by the local drop below the vapor pressure makes considerably more cavity or bubble volume than some other liquids, namely hydrocarbons and hot water[17]. (See Section 2.3.1.) The table refers to room temperature or cold water.

By way of illustration, computing the minimum flow of the end-suction volute pump of the *Design Example* begins with Curve B in Figure 38 (for pumps with 6-inch discharge and larger and for 1800 rpm and lower as stated on the figure). [This pump has a discharge port of about 9 inches (229 mm) as would be the case if the velocity in this port were half of the throat velocity V_T in Part A of Table 11, as suggested previously in the paragraphs on *Volutes* under *Designing the Collector*.] N_{ss} for this pump was chosen as 12,300 ($\Omega_{ss} = 4.5$), which yields 41.5% for K_7. If it were decided to provide this cold-water pump with 16.4 ft (5 m) of $NPSH_A$, R would be 1.17, and the figure yields 0.97 for K_M. [$NPSH_{3\%} = 14$ ft. (4.27 m) for this pump, as seen in Table 6.] Thus, from Eq. 68, this pump has an *MCSF* of 0.415×0.97 or 40% of Q_{BEP}. Had it been designed for $N_{ss} = 11{,}000$ ($\Omega_{ss} = 4.025$), and if R still were 1.17, the $NPSH_A$ would have been 19 ft (5.8 m) and *MCFS* would have been 0.36×0.97 or 35% of Q_{BEP}. Moreover, if it were pumping hydrocarbons at this same $NPSH_A$, *MCFS* would have been even lower, namely 0.36×0.78 or 28% of Q_{BEP}. It would appear, though, that for many applications, the pump as designed (at $\Omega_{ss} = 4.5$) has a low enough energy level to allow for an adequate range of flow-rate capability, and that therefore, the value $N_{ss} = 12{,}300$ is in this case not excessive.

Cavitation Considerations Having alluded to and treated the subject of cavitation a number of times in this section, we should expand on the role that this ever-present phenomenon plays in the operation and durability of centrifugal pumps, particularly those having a high energy level. The manifestations of cavitation that are encountered and become issues for the operability and life of a pump are a) cavitation accompanying backflow from the impeller eye, b) cavitation-generated instabilities and pressure pulsations, and c) erosion, which involves the prediction of the $NPSH_R$-versus-flow rate characteristic curve to maintain life and, conversely (d) the prediction of life for a given $NPSH_A$. The range of *NPSH* over which cavitation occurs within a pump extends from the point where pump head or pressure rise undergoes an identifiable drop—usually 3% for repeatable results for the *NPSH*-value involved—namely the "performance-*NPSH*" or $NPSH_{3\%}$—upwards. As *NPSH* increases from this point, there is an extensive range over which no observable performance loss is detected, yet erosive damage is progressing at a sometimes excessive rate. Finally, at the upper end of the range, all two-phase activity ceases—all bubbles and cavities are suppressed—namely, at the inception-*NPSH* value or $NPSH_i$. As stated previously, $NPSH_i$ has been observed to be typically about five times $NPSH_{3\%}$. This is clearly described in Section 2.3.1, in which the different *NPSH*-limits are distinguished. The following cavitation considerations pertain to this range.

a) Cavitation and backflow. The minimum flow limits imposed by the *R*-value or *NPSH*-effect arise partly because a lower flow rate at a low *NPSH*—although it may be in excess of $NPSH_{3\%}$—involves a strong interaction between suction recirculation and cavitation that can be intense, especially for inducers and large-eye (large D_e/D_2) impellers. At flow rates $Q \ll Q_{SR}$, there exists upstream of the impeller an annulus of back-flowing fluid that emerges from the impeller. Drawing the velocity diagram at the impeller leading edge at the shroud for the case of reversed flow reveals that the absolute velocity component V i) is mostly circumferential and ii) is greater than the impeller tip speed $U_{t,1}$ or U_e. Thus the fluid leaving the impeller hugs the outer wall of the approach passage. If this passage is an axial pipe supplying an end-suction impeller or inducer, the pressure along the centerline can be below the vapor pressure, thus creating a vapor core that extends many

diameters upstream, as was shown in a photograph that is part of an article by Yedidiah[73]. Obviously the energetic backflow has to be balanced by an equivalent inflow that enters the impeller from the interior of the pipe and therefore along the hub streamline of the impeller. Vapor from the core is drawn in also and tends to fill the impeller and vapor-lock it. At this point, the pressure to drive the highly spinning liquid upstream is non-existent and the backflow ceases. The vapor core disappears and the impeller once more begins ingesting liquid, the process just described repeating itself at a very low frequency (as low as 1 to 6 Hz) and called cavitation surge[74]. It has been found possible to passively divert the backflowing liquid outward from the inlet passage at the impeller or inducer eye into a series of vaned passages surrounding the inlet pipe, the vanes deswirling the backflowing liquid and returning it to a point or annular port upstream. Properly designed, this "backflow recirculator" has completely eliminated all cavitation instabilities in inducers—over the full range of flow rate from shut-off to run-out. It was shown to work for some high-N_{ss} impellers to which it was applied[74]. Cavitation surge, however, is rarely seen in low-N_{ss} impellers and is usually completely avoided by running the pump at flow rates greater than minimum flow Q_{min} as established by one of the previous methods or by test.

b) Cavitation-related instabilities and pressure pulsations. At flow rates greater than Q_{min}, cavitation can cause or intensify pressure pulsations. Such instabilities are connected with the variety of cavity and bubble configurations that can exist over the range of flow rates and *NPSH*- or *R*-values. The nature and extent of cavitating flow within a pump has been studied extensively by visual observation. Figures 40 and 41 are laboratory photographs[61] of a sector of a boiler feed pump impeller eye, in which the suction sides of some of the blades are visible. These were taken with the aid of a bright flash that lasted for 1 μs. They can also be found in Ref. 24 of Section 2.3.1. Figure 40a shows the sheet cavity that exists at BEP flow rate and at an *R*-value of 2. Also observed at BEP—but at $R = 1$ (that is, $NPSH = NPSH_{3\%}$)—is the thick, extensive cavity of Figure 40b. This cavity extends from the blade leading edge to the throat formed by the leading edge of the following blade, and this same pattern exists on every blade. Most observers note that when this suction-side cavity reaches the next throat, the pressure rise or liquid head starts breaking down—which is what is recorded at this "3-percent-*NPSH*" point. Instabilities tend to be at a minimum at both of these relatively steady-flow conditions.

Figure 41, on the other hand, displays highly unsteady cavity flows. Both photographs (A and B) were taken at the same half-flow condition at different instants—for $R = 2$. A similar sequence of three photographs at this condition appears in Section 9.5, and none of the three possesses a cavity pattern that resembles either of the others. The position of the somewhat smaller cloud in Figure 41b that has broken off the main cavity appears to be traveling toward the pressure-side (out of sight) of the next blade. Pressure-side cavitation erosion would be the result, and this accords with the findings in Section 2.3.2.

Pressure pulsations are associated with unsteady cavitation patterns, and plots of the amplitude and frequency of suction pressure pulsations show increasing frequency as *R* is

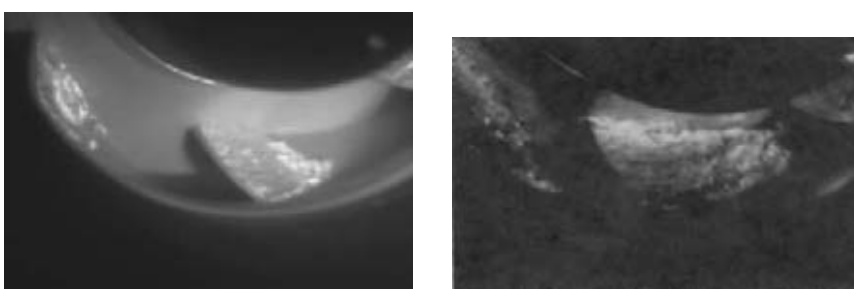

a. b.

FIGURE 40 Cavities on impeller blades at BEP flow rate: a) $NPSH = 2 \times NPSH_{3\%}$; b) $NPSH = NPSH_{3\%}$. (Source: Flowserve Corporation)[61]

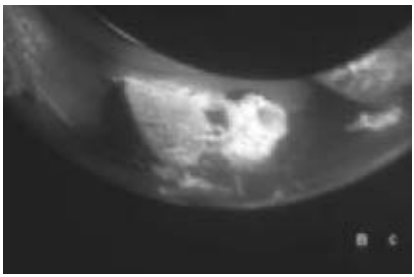

a.

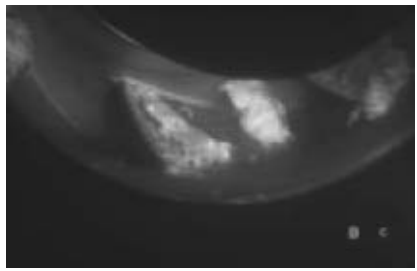

b.

FIGURE 41A and B Cavities on impeller blades at half the BEP flow rate: $NPSH = 2 \times NPSH_{3\%}$. (Source: Flowserve Corporation)[61]

increased—as would be expected as bubble size is reduced. The amplitude peaks at R greater than 1—usually closer to 2. Elimination of these instabilities is best done by avoiding cavitation. This can be done by increasing *NPSHA* and optimizing the blade shape for minimum cavity activity[75]. To avoid the excessive pump and system oscillations that can occur, some users specify that a cavitation-flow visualization test be conducted and require that minimal or no cavities shall be observed.

c) Erosion due to cavitation and the prediction of the Life-NPSH. In the majority of cases cavitation is unavoidable, and the issue becomes the life of component (usually the impeller) in resistance to attack by collapsing bubbles and larger cavities as they are swept out of the low-pressure regions near the blade leading edges. The pressure created at the point and instant of collapse is immense. Photographs of the erosive damage resulting from this activity can be found in Sections 2.3.1 and 9.5. The surface failure mechanism is one of fatigue due to repeated collapse of bubbles adjacent to the blade. This happens at a large number of closely spaced sites, the resulting erosion having a strongly pitted texture. The rate of erosive depth penetration into the surface of a venturi subject to bubble collapse was found by Knapp[76] to increase as the sixth power of velocity V at a constant cavitation number $k = 2(p_1 - p_v)/\rho V^2$. In other words, the erosion rate increased as the third power of $(p_1 - p_v)$ or *NPSH* at the inlet of the venturi, which means that the collapse pressure rises with *NPSH*, as is known from the Rayleigh bubble collapse theory. The velocity V in Knapp's venturi corresponds in a pump to the maximum relative velocity W at inlet—which is conveniently represented by the impeller inlet tip speed $U_{t,1}$ as a criterion for damage rate—and τ corresponds to the cavitation number k. For a given impeller at constant Q/N and a constant value of τ, (or at a constant available suction specific speed,) the higher $U_{t,1}$ is, the greater the *NPSH* and the greater the damage rate. Also, as mentioned earlier, a higher value of $U_{t,1}$ implies a correspondingly greater U_2 and, therefore, greater pump pressure rise or head. Therefore, high-head pumps are more likely to suffer from cavitation erosion, making cavitation a "high-energy" pump phenomenon. High pressure-rise has already been shown to be a feature of high energy pumps through the definition of energy level in terms of classical stress loading (Figure 32).

Facing the reality of high-energy pump destruction due to cavitation erosion, Vlaming redefined the term "*NPSHR*" to mean $NPSH_{40,000\ \text{hrs.}}$; that is, the *NPSH* needed to limit the damage sufficiently so as to ensure an impeller life of 40,000 hours. He developed an empirical method for predicting the curve of this "damage-*NPSH*" versus flow rate for conventionally-designed impellers[77]. This method is defined in Table 17 and includes the inlet tip speed effect on the erosion rate. A value of the vaporization factor C_b that is less than unity applies to hot water and to other liquids such as hydrocarbons, which generate far less vapor volume when they cavitate than does cold water. (See the earlier discussion under *NPSH Effects* in the subsection on *Specific Speed and Optimum Geometry*.) (Rather than depend on theory for the API process pumps men-

TABLE 17 *NPSH* required for 40,000 hours life[77]

$$NPSH_R = NPSH_{SE} + f\left(\frac{Q}{Q_{BEP}}, \frac{Q_{BEP}}{Q_{SE}}, NPSH_{SE}\right)$$

where

$$NPSH_{SE} = C_a \cdot C_b \cdot C_c \cdot \left[(k_1 + k_2)\phi_e^2 + k_2\right] \cdot \frac{U_e^2}{2g}$$

and C_a = Specific Speed Effect (= 1 for $N_s \geq 1000$) ($\Omega_s \geq 0.366$)
C_b = Vaporization Effect [= 1 for cold water; 0.74 for 350°F (177°C) water]
C_c = Material Effect (= 1 for 12 Cr. Stainless Steels)
k_1 = 1.2

$$k_2 = 0.2334 + \left\{\begin{matrix}\left[U_e\,(\text{ft/sec})/400\right]^4 \\ \left[U_e\,(\text{m/s})/128.3\right]^4\end{matrix}\right\} = \left\{\begin{matrix}\text{inlet tip} \\ \text{speed effect}\end{matrix}\right.$$

$$f = \begin{cases}\left[887\left(\frac{Q_{SE}}{Q_{BEP}} - \frac{Q}{Q_{BEP}}\right) + 893\left(\frac{Q_{SE}}{Q_{BEP}} - \frac{Q}{Q_{BEP}}\right)^2\right] \cdot X & \left\{\frac{Q}{Q_{SE}} \leq 1\right. \\ \left[2820\left(\frac{Q}{Q_{BEP}} - \frac{Q_{SE}}{Q_{BEP}}\right) + 6610\left(\frac{Q}{Q_{BEP}} - \frac{Q_{SE}}{Q_{BEP}}\right)^2\right] \cdot X & \left\{\frac{Q}{Q_{SE}} \geq 1\right.\end{cases}$$

and $X = \left(S^{1.105} - S\right)/1000$ where $S = \left\{\begin{matrix}NPSH_{SE}\,(\text{ft}) \\ 3.2808 \times NPSH_{SE}\,(\text{m})\end{matrix}\right.$

tioned earlier in connection with their minimum flow data, Heald and Palgrave quantified $NPSH_{40,000\ hrs.}$ in Figure 39b[71].)

Applied to the high-energy multistage pump suction stage of Figure 33 and Table 14, Vlaming's method yields the $NPSH_R$-values shown in Table 18 under the heading ϕ_e=0.3. These are plotted as the $NPSH_{40,000\ hrs.}$-curve on Figure 37. The blades of the pump are assumed to be set for zero incidence of the incoming flow to their camber lines at the BEP —called "shockless entry" and denoted by "SE." (Many designers make Q_{SE} somewhat larger than Q_{BEP} to achieve lower *NPSHR* at $Q > Q_{BEP}$.) The column to the right in the table contains the results for the same method applied to the more common case for high-energy pump suction stages, namely $\phi_e = 0.25$ (and lower). For the same shaft diameter, flow rate and speed, $\phi_e = 0.25$ yields a larger eye diameter through Eq. 49; namely, 13.92 in. (353.6 mm) versus 13.37 in (339.6 mm) for the $\phi_e = 0.3$ case as shown in Figure 33. Moreover, that figure shows the inlet tip speed $U_{t,1}$ (U_e) to be 274 ft/sec (84 m/s), whereas for the larger-eye case the value is computed to be 286 ft/sec (87 m/s). As Table 18 reveals, this larger-eye impeller has a lower value of $NPSH_{3\%}$ (as computed from the correlations of Table 1), which is the reason for sizing large eyes. But Vlaming's method indicates that the smaller eye requires less "damage-*NPSH*" ($R = 1.69$) than does the larger eye ($R = 2.06$), even though the latter requires less "performance-*NPSH*" or $NPSH_{3\%}$. So, from both a minimum-flow and a cavitation damage standpoint, the advantage of a smaller eye for high energy levels is evident.

d) Prediction of life for a given $NPSH_A$. The inverse of the foregoing problem is how to determine the life under cavitating conditions at a given value of available *NPSH*. Gülich found a connection between an observed length L_{cav} of the cavity trailing off the leading

TABLE 18 *NPSHR* of high-energy pump suctions stages

A) NPSH Required to Maintain Head Rise: $NPSH_{3\%}$

$NPSH_{3\%}$, ft(m) (3% reduction in ΔH)	$\frac{Q}{Q_{BEP}}$	$NPSH_{3\%}$, ft(m) ϕ_e=0.3*	ϕ_e=0.25
$\tau_{3\%}$	[100]	0.2633	0.214
$k_1 = 1.69$, $k_2 = 0.102$ [Table (1)]	100	307(94)	271(83)
[Empirically Calculated]	150	1150(350)	1150(350)

B) NPSH Required to Limit Cavitation Damage: $NPSH_{40,000\ hrs.}$

$NPSH_{40,000\ hrs.\ Life}$	$\frac{Q}{Q_{BEP}}$	$NPSH_R$, ft(m) ϕ_e=0.3*	ϕ_e=0.25
Vlaming's Empirical Method (for $Q_{SE} = Q_{BEP}$)	0.25	1081(329)	1174(358)
	0.50	840(256)	910(277)
	0.75	653(199)	705(215)
	0.90	566(173)	610(186)
$R = \frac{NPSH_{40,000\ hrs.}}{NPSH_{3\%}}$	1.00	519(158)	559(170)
	[1.00]	R=1.69	R=2.06
	1.10	687(209)	743(226)
	1.25	1058(322)	1148(350)
	1.50	1994(608)	2173(662)

*Values predicted for sample high-energy pump suction stage: $\phi_e = 0.3$; $\phi_e \leq 0.25$ widely typical of suction (1st) stages.

edge of the blade at BEP (Figure 40a) and the life of an impeller operating at this condition[78]. The resulting procedure is outlined in Table 19, beginning with the definition that the life is the time it takes for the erosion to penetrate through 75% of the blade (or wall) thickness. In the absence of a cavitation-visualizing test, L_{cav} can be estimated as suggested by the last two formulas in Table 19[75]. Critical to this estimate is the assumed value of the "inception-*NPSH*" or τ_i. For conventionally designed impeller blades, $\tau_i \approx 1$ at the BEP, whereas aerodynamically shaped blades that minimize the local reduction of static pressure have been produced with $\tau_i < 0.5$ at the BEP[75,79]. The life computations of Table 20 follow from application of the method of Table 19 to the sample suction stage of Figure 33 for $\tau_i = 1$ and 0.5. Higher values of τ_i apply for $Q \neq Q_{BEP}$—as might be expected from the shape of Vlaming's $NPSH_{40,000\ hrs.}$-curve in Figure 37 and the fact that the local pressure reduction in the leading-edge region increases with incidence. From this and the results of Table 20, it is evident that improvements to conventional blade-design practice are essential if life is to exceed half a year. Further, this life calculation method is based on the existence of a sheet cavity like that of Figure 40a; and the disordered cavity structures of Figure 41, which happen in the presence of recirculation, are not addressed. Low-flow cavitation damage is generally more severe, and is described in Section 2.3.2.

TABLE 19 Prediction of life under cavitating conditions

Table 19. Prediction of Life Under Cavitating Conditions

Life=the minimum of ($Life_{s.s.}$, $Life_{p.s.}$), where s.s.= suction side of blade;

and p.s. = pressure side of blade.

And where Life = 0.75 x t/MDPR, where t = blade thickness, mm;

MDPR=mean depth of penetration rate, mm/hour.

$$MDPR = \left[C \times (L_{cav}/10)^n \times \left(\tau_A - \phi_e^2\right)^3 \times U_e^6 \times \rho_L^3 \times A \right] \Big/ \left[8 \times F_{mat} \times (TS)^2 \right] \text{ mm/h}$$

Where C = 8.28 E-06 (s.s.), 396 E-06 (p.s.); and n = 2.83 (s.s.), 2.6 (p.s.);

τ = NPSH$/\left(U_e^2/2g\right)$; dimension less

U_e is blade inlet tip speed in m/s

ϕ_e = $V_{m,1}/U_e$, where $V_{m,1}$ = average axial inlet velocity, (typically ϕ_e = 0.25);

ρ_L = 1000 × sp. gravity of the liquid; A = 1 for cold water, 0.705 for 350° F (177° C) water;

F_{mat} = 1 for martensitic: stainless steel, 1.7 for austenitic stainless steel;

TS = tensile strength in Pa [= 860,000,000 (= 125,000 psi) for 13 Cr and
= 552,000,000 (= 80,000 psi) for 18 Cr, 8 Ni.]

$$L_{cav} \approx \left(\pi \times D_e/n_b\right) \times \left\{1 - \left[\left(\tau_A - \tau_{3\%}\right)/\left(\tau_i - \tau_{3\%}\right)\right]^{1/3}\right\} \text{ if } \tau_A < \tau_i \text{ (mm)}$$

L_{cav} = 0 if $\tau_A > \tau_i$

Moreover, corrosion can play a role in cavitation-related erosive activity, an effect that was also addressed in Gülich's work.[78] Nevertheless, the ability to compute erosive behavior—even at the BEP—allows one to evaluate design improvements and provides a good idea of the life that can be expected under normal operating conditions.

Obviously, if the available *NPSH* is greater than the inception-*NPSH* (that is, $\tau_A > \tau_i$), there is no bubble activity of any kind, and at Q_{BEP} the cavity length $L_{cav} = 0$. An illustration of what can be achieved in this regard is presented in Figures 24 and 25 of Section 9.5, which are the "before" and "after" photographs of the model impeller blades for the first stage of a 24,000 hp (18 MW) pipeline pump. *Q*uasi-three dimensional analysis of the blade pressure loading led to changes in shape that eliminated the cavities[53,75]. This complete absence of cavitation is becoming the desired objective for the design and application of new and upgraded multistage high-energy pump suction stages. This approach eliminates both the erratic mechanical behavior that occurs in response to unsteady cavity patterns and the erosion due to bubble collapse; thereby substantially increasing the life and reliability of such machines[80].

TABLE 20 Life of high-energy pump suction stage

A) Pump data for computing life [at the B.E.P. of 20,000 gpm (1,262 m^3/s)]

- $NPSH_{3\%}$ = 307 ft (94 m) ; thus, $\tau_{3\%}$ = 0.263
- NPSHA = 519 ft (158 m) ; thus, τ_A = 0.444
- t_{blade} = 0.42 in (10.7 m) ; thus, F_{mat} = 1 (13 Cr martensitic stainless steel)
- Suction-side cavitation in 350°F (177°C) boiler feedwater, for which A=0.705
- Inlet flow coefficient ϕ_e =0.3; U_e = 274.2 ft/sec (83.57 m/s); $U_e^2/2g$=1168ft (356 m)

B) Results for inception occurring at $NPSH_i$ = blade inlet tip speed head and half that $NPSH_i$.

a) τ_i =1.0 = 3.8 x $\tau_{3\%}$	b) τ_i = 0.5 = 1.9 x $\tau_{3\%}$
$NPSH_i$ = 1168 ft (356 m)	$NPSH_i$ = 584 ft (178 m)
Lcav = 57.0 mm	13.1 mm
MDPR = 0.0014482 mm/hour	0.000022257 mm/hour
Life = 5,541 hours = 7.6 months	360,000 hours = 41 years

C) Sample Life Calculation { High Energy Pump Suction Stage

$$L_{cav} = 25.4 \times \frac{\pi \times 13.37}{7} \times \left[1 - \left(\frac{0.444 - 0.263}{1 - 0.263}\right)^{1/3}\right] = \underline{57.0 \text{ mm}}$$

$$MDPR = \frac{8.28 \times 10^{-6} \times \left(\frac{57}{10}\right)^{2.83} \times \left(0.444 - \overline{0.3}^2\right) \times (83.57)^6 \times (890)^3 \times 0.705}{8 \times 1 \times \left(860 \times 10^6\right)^2}$$

$$= 0.0014482 \text{ mm / hour} \left(\times 8760 \frac{\text{hr}}{\text{year}} = 12.7 \text{ mm/yr} \right)$$

$$\text{Life} = 0.75 \times 10.7/0.0014482 = \underline{5{,}541 \text{ hours}}$$

$$= \underline{7.6 \text{ months}}$$

REFERENCES

1. Jennings, G. P., and Meade, L. P. "Determination of Pump Efficiencies from Fluid Temperature Rise." Presented at the 7th Annual Spring Pipeline Conference, Houston, Texas, May 14, 1956, under the auspices of the American Petroleum Institute's *Division of Transportation.* Published in the Division's Vol. 36 [5] 1956.
2. Cooper, P., and Reshotko, E. "Turbulent Flow Between a Rotating Disk and a Parallel Wall." *AIAA Journal.* Volume 13, No. 5, May 1975, pp. 573–578.

3. Sabersky, R., and Acosta, A. J. *Fluid Flow*, Macmillan, p. 76 (1966).
4. Stepanoff, A. J. *Centrifugal and Axial Flow Pumps.* 2nd ed. Krieger Publishing, Malabar, FL, 1957.
5. Iversen, H. W. "Performance of the Periphery Pump." *Transactions of the ASME.* Vol. 77, Jan. 1955, pp. 15–28.
6. Anderson, H. H. "Prediction of Head, Quantity and Efficiency in Pumps—The Area Ratio Principle." *Performance Prediction of Centrifugal Pumps and Compressors*. ASME, 1980, pp. 201–211.
7. American National Standard for Centrifugal Pumps for Design and Application, ANSI/HI 1.3-2000, Section 1.3.4.1.11-14, Hydraulic Institute, Parsippany, NJ, www.pumps.org.
8. Cooper, P. "Analysis of Single- and Two-Phase Flows in Turbopump Inducers." *Transactions of the ASME, Journal of Engineering for Power*. Vol. 89, Series A, Oct. 1967, pp. 577–588.
9. Turpin, J. L., Lea, J. F., and Bearden J. L. "Gas-Liquid Flow Through Centrifugal Pumps—Correlation of Data." *Proceedings of the Third International Pump Symposium*, Texas A&M University, 1986, pp. 13–20.
10. Runstadler, P. W., Jr., and Dolan, F. X. "Two-Phase Flow, Pump Data for a Scale Model NSSS Pump." *Polyphase Flow in Turbomachinery*, ASME, 1978, pp. 65–77.
11. Cooper, P., and others. "Tutorial on Multiphase Gas-Liquid Pumping." *Proceedings of the Thirteenth International Pump Users Symposium*, Texas A&M University, Mar. 1996, pp. 159–174.
12. Kasztejna, P. J., and Cooper, P. "Hydraulic Development of Centrifugal Pumps for Coal Slurry Service." *Proceedings of the Eighth International Symposium on Coal Slurry Fuels Preparation and Utilization*. U.S. Dept. of Energy, May 1986.
13. Gongwer, C. A. *Transactions of the ASME.* Vol. 63, Jan. 1941, pp. 29–40.
14. Stripling, L. B., and Acosta, A. J. "Cavitation in Turbopumps." Parts 1 and 2, *Transactions of the ASME.* Series D, 1961.
15. Lazarkiewicz, S., and Troskolanski, A. T. *Impeller Pumps*. Pergamon Press.
16. Katsanis, T., and McNally, W. D. "Revised Fortran Program for Calculating Velocities and Streamlines on the Hub-Shroud Midchannel Stream Surface of an Axial-, Radial-, or Mixed-Flow Turbomachine or Annular Duct." I, User's Manual, NASA TN D-8430, and II, Programmer's Manual, NASA TN D-8431, 1977.
17. Cooper, P. "Application of Pressure and Velocity Criteria to the Design of a Centrifugal-Pump Impeller and Inlet." *Transactions of the ASME*. Series A, Apr. 1964, pp. 181–190.
18. Busemann, A. "Das Förderhohenverhaltniss Radialer Kreiselpumpen mit Logarithmischspiraligen Schaufeln." *Zeitschrift für Angewandte Mathematik und Mechanik.* Vol. 8, Oct. 1928, pp. 372–384.
19. Wiesner, F. J. "A Review of Slip Factors for Centrifugal Pumps." *Transactions of the ASME.* Series A, Oct. 1967, pp. 558–572.
20. Pfleiderer, C. *Die Kreiselpumpen für Flüssigkeiten und Gase.* 5te Auflage, Springer-Verlag, 1961.
21. Dicmas, J. L. *Vertical Turbine, Mixed Flow, and Propeller Pumps.* McGraw-Hill, 1987.
22. Stanitz, J. D., and Prian, V. D. "A Rapid Approximate Method for Determining the Velocity Distribution on Impeller Blades of Centrifugal Compressors." TN 2421, NACA, July 1951.
23. Lieblein, S. "Experimental Flow in Two-Dimensional Cascades." Chap. VI in *Aerodynamic Design of Axial-Flow Compressors*. SP-36, NASA, 1965, pp. 202–205.
24. Guinzburg, A., and others. "Emerging Sewage Pump Design Requirements." *1997 ASME Fluids Engineering Division Summer Meeting*. Paper FEDSM97-3325, June 1997.

25. Worster, R. C. "The Flow in Volutes and Its Effect on Centrifugal Pump Performance." *Proceedings of the Institution of Mechanical Engineers.* Vol. 177, No. 31, 1963.

26. Lorett, J. A., and Gopalakrishnan, S. "Interaction Between Impeller and Volute of Pumps at Off-Design Conditions." *Transactions of the ASME, Journal of Fluids Engineering.* Vol. 108, Mar. 1986, pp. 12–18.

27. Miller, D. S. *Internal Flow Systems*, BHRA Fluid Engineering, 1978.

28. Japikse, D. "A Critical Evaluation of Stall Concepts for Centrifugal Compressors and Pumps—Studies in Component Performance, Part 7." In *Stability, Stall and Surge in Compressors and Pumps.* FED—Vol. 19, ASME, Dec. 1984, pp. 1–10.

29. Kovats, A. "Diffusers of Multistage Centrifugal Pumps." In *Return Passages of Multi-Stage Turbomachinery*. FED—Vol. 3, ASME, June 1983, pp. 61–66.

30. Reneau, L. R., and others. "Performance of Straight, Two-Dimensional Diffusers." *Transactions of the ASME.* Series D, Vol. 89, 1967, pp. 141–150.

31. Fox, R. W., and Kline, S. J. "Flow Regimes in Curved, Subsonic Diffusers." *Transactions of the ASME*. Series D, Vol. 84, 1962, pp. 303–316.

32. Sagi, C. J, and Johnston, J. P. "The Design and Performance of Two-Dimensional, Curved Diffusers." *Transactions of the ASME*. Series D, Vol. 89, 1967, pp. 715–731.

33. Bolleter, U. "Blade Passage Tones of Centrifugal Pumps." *Vibrations.* Vol. 4, No. 3, Sep. 1988, pp. 8–13.

34. Nykorowytsch, P., Ed. *Return Passages of Multi-Stage Turbomachinery.* FED—Vol. 3, ASME, June 1983.

35. Hill, P. G., and Peterson, C. R. *Mechanics and Thermodynamics of Propulsion.* Addison-Wesley, 1965, pp. 238–280.

36. Stepanoff, A. J. "Centrifugal Pump Performance as a Function of Specific Speed." *Transactions of the ASME.* Aug. 1943, pp. 629–647.

37. Weissgerber, C., and Carter, A. F. "Comparison of Hydraulic Performance Predictions and Test Data for a Range of Pumps." *Performance Prediction of Centrifugal Pumps and Compressors.* ASME, Mar. 1980, pp. 219–226.

38. Streeter, V. L., ed. *Handbook of Fluid Dynamics.* McGraw-Hill, 1961, p. 3–23.

39. Wood, G. M., Welna H., and Lamers, R. P. "Tip–Clearance Effects in Centrifugal Pumps." Paper No. 64–WA/FE–17, ASME, Nov. 1964.

40. Stepanoff, A. J. "Pumping Solid–Liquid Mixtures." Paper No. 63–WA–102, ASME, Nov. 1963.

41. Katsanis, T. "Quasi-Three-Dimensional Full Analysis in Turbomachines: A Tool for Blade Design." In *Numerical Simulations in Turbomachinery*, FED—Vol. 120, ASME, 1991, pp. 57–64.

42. Katsanis, T. "Fortran Program for Calculating Transonic Velocities on a Blade–to–Blade Stream Surface of a Turbomachine." NASA TN D–5427, 1969.

43. Spring, H. "Affordable Quasi-Three-Dimensional Inverse Design Method for Pump Impellers." *Proceedings of the Ninth International Pump Users Symposium*, Texas A&M University, College Station Texas, Mar. 1992, pp. 97–110.

44. Daily, J. W., and Nece, R. E. "Chamber Dimension Effects on Induced Flow and Frictional Resistance of Enclosed Rotating Disks." *Transactions of the ASME*, Series D, Vol. 82, Mar. 1960, pp. 217–232.

45. Nece, R. E., and Daily, J. W. "Roughness Effects on Frictional Resistance of Enclosed Rotating Disks." *Transactions of the ASME.* Series D, Vol. 82, Sep. 1960, pp. 553–562.

46. Graf, E. "Analysis of Centrifugal Impeller BEP and Recirculating Flows: Comparison of Quasi–3D and Navier–Stokes Solutions." *Pumping Machinery—1993.* FED–Vol. 154, ASME, 1993, pp. 235–245.

47. Gülich, J. F., Favre, J. N., and Denus, K. "An Assessment of Pump Impeller Performance Predictions by 3D–Navier Stokes Calculations." *1997 ASME Fluids Engineering Division Summer Meeting.* Paper FEDSM97–3341, June 1997.

48. Japikse, D., Marscher, W. D., and Furst, R. B. *Centrifugal Pump Design and Performance*. Concepts, ETI, Inc., Wilder, Vermont, 1997.

49. Denus, K., and others. "A Study in Design and CFD Analysis of a Mixed Flow Pump Impeller." *1999 ASME Fluids Engineering Division Summer Meeting*, Paper FEDSM99–6858, July 1999.

50. Jimbo, H. "Investigation of the Interaction of Windage and Leakage Phenomena in a Centrifugal Compressor." Paper No. 56–A–47, ASME, Nov. 1956.

51. Keathly, W. C., Due, H. F., and Comolli, C. R. "A Study of Pressure Prediction Methods for Radial Flow Impellers." Final Report on NASA Contract NAS8–5442, PWA FR–952, Pratt & Whitney Aircraft, W. Palm Beach, Florida, April 1964.

52. Greitzer, E. M. "The Stability of Pumping Systems." *Transactions of the ASME, Journal of Fluids Engineering*, Vol. 103, June, 1981, pp. 193–242.

53. Cooper, P. "Perspective: The New Face of R&D—A Case Study of the Pump Industry." *Transactions of the ASME, Journal of Fluids Engineering*, Vol. 118, Dec. 1996, pp. 654–664.

54. Rothe, P. H., and Runstadler, P. W., Jr. "First–Order Pump Surge Behavior." Paper No. 77–WA/FE–12, ASME, Nov. 1977.

55. Brennen, C., and Acosta, A. J. "The Dynamic Transfer Function for a Cavitating Inducer." *Transactions of the ASME, Journal of Fluids Engineering.* Vol. 98, 1976, pp. 182–191.

56. Schlichting, H. *Boundary Layer Theory.* 4th ed. McGraw-Hill, 1960.

57. "Advanced Class Boiler Feed Pumps." *Proceedings of the Institution of Mechanical Engineers.* Vol. 184, Part 3N, 1970.

58. Gopalakrishnan, S. "Pump Research & Development—Past, Present, and Future: An American Perspective." *1997 ASME Fluids Engineering Division Summer Meeting*. Paper FEDSM97–3387, June 1997.

59. Bolleter, U., Frei, A., and Florjancic, D. "Predicting and Improving the Dynamic Behavior of Multistage High Performance Pumps." *Proceedings of the First International Pump Symposium*. Texas A&M University, College Station Texas, May 1984, pp. 1–8.

60. Iino, T. "Potential Interaction Between a Centrifugal Pump Impeller and a Vaned Diffuser." *Fluid/Structure Interactions in Turbomachinery*. ASME, Nov. 1981, pp. 63–69.

61. Cooper, P. "Hydraulics and Cavitation." *Symposium Proceedings: Power Plant Pumps*. M. L. Adams, ed. EPRI CS–5857, June 1988, pp. 4–109 to 4–149.

62. Sutton, G. P. *Rocket Propulsion Elements*. 6th ed., Wiley, 1992.

63. "Liquid Rocket Engine Centrifugal Flow Turbopumps." Report SP–8109 of the series entitled *NASA Space Vehicle Design Criteria (Chemical Propulsion)*. NASA, 1973.

64. "Turbopump Systems for Liquid Rocket Engines." Report SP–8107 of the series entitled *NASA Space Vehicle Design Criteria (Chemical Propulsion)*. NASA, 1975.

65. Makay, E., Cooper, P., Sloteman, D. P., and Gibson, R. "Investigation of Pressure Pulsations Arising from Impeller/Diffuser Interaction in a Large Centrifugal Pump." Proceedings: Rotating Machinery Conference and Exposition, ASME, Vol. 1, 1993.

66. Fischer, K., and Thoma, D. "Investigation of the Flow Conditions in a Centrifugal Pump." *Transactions of the ASME.* Vol. 54, 1932, pp. 143–155.

67. Fraser, W. H. "Recirculation in Centrifugal Pumps." *Materials of Construction of Fluid Machinery and Their Relationship to Design and Performance.* ASME, Nov. 1981, pp. 65–86.

68. Iino, T., Sato, H., and Miyashiro, H. "Hydraulic Axial Thrust in Multistage Centrifugal Pumps." *Transactions of the ASME, Journal of Fluids Engineering.* Vol. 102, Mar. 1980, pp. 64–69.

69. Makay, E., and Barrett, J. A. "Changes in Hydraulic Component Geometries Greatly Increased Power Plant Availability and Reduced Maintenance Cost: Case Histories." *Proceedings of the First International Pump Symposium.* Texas A&M University, College Station Texas, May 1984, pp. 85–97.

70. Gopalakrishnan, S. "A New Method for Computing Minimum Flow." *Proceedings of the Fifth International Pump Users Symposium.* Texas A&M University, College Station Texas, May 1988, pp. 41–47.

71. Heald, C. C., and Palgrave, R. "Backflow Control Improves Pump Performance." *Oil and Gas Journal.* Feb. 25, 1985, pp. 96–105.

72. Hallam, J. L. "Centrifugal Pumps: Which Suction–Specific Speeds Are Acceptable." *Hydrocarbon Processing*, Apr. 1982.

73. Yedidiah, S. "Performance Curves: Key to Centrifugal Pump Selection." *Machine Design.* Apr. 10, 1980, pp. 117–122.

74. Sloteman, D. P., Cooper, P., and Dussourd, J. L. "Control of Backflow at the Inlets of Centrifugal Pumps and Inducers." *Proceedings of the First International Pump Symposium*. Texas A&M University, College Station Texas, May 1984, pp. 9–22.

75. Cooper, P., Sloteman, D. P., Graf, E., and Vlaming, D. J. "Elimination of Cavitation–Related Instabilities and Damage in High–Energy Pump Impellers." *Proceedings of the Eighth International Pump Users Symposium.* Texas A&M University, 1991, pp. 3–19.

76. Knapp, R. T. "Recent Investigations of the Mechanics of Cavitation and Cavitation Damage." *Transactions of the ASME*, Oct. 1955, pp. 1045–1054.

77. Vlaming, D. J. "Optimum Impeller Inlet Geometry for Minimum *NPSH* Requirements for Centrifugal Pumps." *Pumping Machinery—1989*. ASME, July 1989, pp. 25–29.

78. Gülich, J. F. *Guidelines for Prevention of Cavitation in Centrifugal Feedpumps.* EPRI CS–6398, 1989.

79. Sloteman, D. P., Cooper, P., and Graf, E. "Design of High–Energy Pump Impellers to Avoid Cavitation Instabilities and Damage." EPRI Power Plant Pumps Symposium, Tampa FL, June 1991.

80. Sloteman, D. P., and others. "Experimental Evaluation of High–Energy Pump Improvements Including Effects of Upstream Piping." *Proceedings of the Twelfth International Pump Users Symposium.* Texas A&M University, Mar. 1995, pp. 97–110.